

TKK Dissertations 258
Espoo 2010

**ALKALI-METAL ATOMS IN LASER FIELDS: OPTICAL
PUMPING, COHERENT POPULATION TRAPPING, AND
LASER COOLING**

Doctoral Dissertation

Thomas Lindvall



**Aalto University
School of Science and Technology
Faculty of Electronics, Communications and Automation
Department of Micro and Nanosciences**

TKK Dissertations 258
Espoo 2010

ALKALI-METAL ATOMS IN LASER FIELDS: OPTICAL PUMPING, COHERENT POPULATION TRAPPING, AND LASER COOLING

Doctoral Dissertation

Thomas Lindvall

Doctoral dissertation for the degree of Doctor of Science in Technology to be presented with due permission of the Faculty of Electronics, Communications and Automation for public examination and debate in Auditorium TU2 at the Aalto University School of Science and Technology (Espoo, Finland) on the 10th of December 2010 at 12 noon.

**Aalto University
School of Science and Technology
Faculty of Electronics, Communications and Automation
Department of Micro and Nanosciences**

**Aalto-universitetet
Tekniska högskolan
Fakulteten för elektronik, kommunikation och automation
Institutionen för mikro- och nanoteknik**

Distribution:
Aalto University
School of Science and Technology
Faculty of Electronics, Communications and Automation
Department of Micro and Nanosciences
P.O. Box 13500 (Tietotie 3)
FI - 00076 Aalto
FINLAND
URL: <http://nano.tkk.fi/>
Tel. +358-9-47001
Fax +358-9-47026080
E-mail: thomas.lindvall@iki.fi

© 2010 Thomas Lindvall

ISBN 978-952-60-3501-7
ISBN 978-952-60-3502-4 (PDF)
ISSN 1795-2239
ISSN 1795-4584 (PDF)
URL: <http://lib.tkk.fi/Diss/2010/isbn9789526035024/>

TKK-DISS-2851

Multiprint Oy
Espoo 2010

ABSTRACT OF DOCTORAL DISSERTATION		AALTO UNIVERSITY SCHOOL OF SCIENCE AND TECHNOLOGY P.O. BOX 11000, FI-00076 AALTO http://www.aalto.fi	
Author Thomas Lindvall			
Name of the dissertation Alkali-metal atoms in laser fields: optical pumping, coherent population trapping, and laser cooling			
Manuscript submitted 22.10.2010		Date of the defence 10.12.2010	
Manuscript revised			
<input type="checkbox"/> Monograph		<input checked="" type="checkbox"/> Article dissertation (summary + original articles)	
Faculty	Faculty of Electronics, Communications and Automation		
Department	Department of Micro and Nanosciences		
Field of research	Electrophysics		
Opponent	Prof. Anders Kastberg		
Supervisor	Prof. Ilkka Tittonen		
<p>Abstract</p> <p>Alkali metals have played an important role in optical and atomic physics from the very beginning. This thesis deals with three aspects and applications of alkali-metal atoms, in particular rubidium (Rb).</p> <p>Optical pumping changes both the amplitudes and the center positions of the absorption profiles in the Doppler-broadened D-line spectra of the alkali-metal atoms. This effect has been studied by reducing the multilevel system to an effective three-level system and by treating the finite interaction time and collisions with the vapor-cell walls in two different ways: as ground-state relaxation and by averaging the time-dependent absorption over the distribution of interaction times. The former is a computationally efficient way to compare theoretical spectra to experimental results, and the latter reveals lineshape details that are due to the coupling between the Doppler shift and the interaction times through the longitudinal velocity of the atoms.</p> <p>Using coherent population trapping (CPT) in ^{85}Rb, an all-optical atomic clock has been realized. The good noise properties of the diode laser, an optimized buffer gas, and a very low light intensity allow detection of ultranarrow CPT resonances < 20 Hz, apparently the narrowest optically induced hyperfine CPT resonance ever measured. The Q value of this resonance, 1.5×10^8, is comparable to Q values in cesium clocks and the stability of the CPT clock is sufficient for many high-precision applications.</p> <p>Trapping of Rb atoms in microscopic magneto-optical traps (MOTs) a few hundred micrometers from the surface of an optically transparent ferrite-garnet permanent-magnet atom chip has been demonstrated. The required magnetic fields are created by magnetic patterns magneto-optically written into the ferrite-garnet film and the transparency of the chip allows using a conventional MOT geometry. The magnetic patterns can be erased and re-written <i>in situ</i>, even during the experiments. Magnetic traps with a trap depth up to 1 mK could be realized using this type of atom chip.</p>			
Keywords alkali metal, optical pumping, coherent population trapping, laser cooling			
ISBN (printed)	978-952-60-3501-7	ISSN (printed)	1795-2239
ISBN (pdf)	978-952-60-3502-4	ISSN (pdf)	1795-4584
Language	English	Number of pages	68 p. + app. 60 p.
Publisher Department of Micro and Nanosciences, Aalto University			
Print distribution Department of Micro and Nanosciences, Aalto University			
<input checked="" type="checkbox"/> The dissertation can be read at http://lib.tkk.fi/Diss/2010/isbn9789526035024/			

SAMMANFATTNING (ABSTRAKT) AV DOKTORSAVHANDLING		AALTO-UNIVERSITETET TEKNISKA HÖGSKOLAN PB 11000, FI-00076 AALTO http://www.aalto.fi	
Författare Thomas Lindvall			
Titel Alkalimetallatomer i laserfält: optisk pumpning, fenomenet coherent population trapping och laserkyllning			
Inlämningsdatum för manuskript 22.10.2010		Datum för disputation 10.12.2010	
Datum för det korrigerade manuskriptet			
<input type="checkbox"/> Monografi <input checked="" type="checkbox"/> Sammanläggningsavhandling (sammandrag + separata publikationer)			
Fakultet	Fakulteten för elektronik, kommunikation och automation		
Institution	Institutionen för mikro- och nanoteknik		
Forskningsområde	Elektrofysik		
Opponent	Prof. Anders Kastberg		
Övervakare	Prof. Ilkka Tittonen		
<p>Sammanfattning (Abstrakt)</p> <p>Alkalimetallerna har spelat en viktig roll i den optiska fysiken och atomfysiken ända från början. Denna avhandling behandlar tre aspekter och tillämpningar av alkalimetallatomer, speciellt rubidium (Rb).</p> <p>Optisk pumpning ändrar både amplituderna och centerpositionerna för absorptionsprofilerna i alkali-metallatomernas Doppler-breddade D-linjespektrum. Den här effekten har undersökts genom att reducera mångnivåsystemet till ett effektivt trenivåsystem och genom att behandla den ändliga växelverknings tiden och kollisioner med ångcellens väggar på två sätt: som relaxering mellan grundtillstånden och genom att integrera den tidsberoende absorptionen över växelverknings tidsdistributionen. Det förstnämnda sättet är ett beräkningseffektivt sätt att jämföra teoretiska spektra med experimentella resultat och det andra uppklarar linjeformsdetaljer som beror på kopplingen mellan Doppler-förskjutningen och växelverknings tiden genom atomernas longitudinella hastighet.</p> <p>Genom att utnyttja fenomenet coherent population trapping (CPT) i ^{85}Rb har ett heloptiskt atomur förverkligats. Diodlaserns goda brusegenskaper, en optimerad buffergas och en mycket låg ljusintensitet tillåter uppmätandet av extremt smala CPT-resonanser < 20 Hz, upperbarligen den smalaste optiskt inducerade hyperfina CPT-resonansen som någonsin mätts. Denna resonans Q-värde, 1.5×10^8, är jämförbart med Q-värdena för cesium-ur och CPT-urets stabilitet är tillräcklig för många högpresisionstillämpningar.</p> <p>Infångandet av Rb-atomer i mikroskopiska magneto-optiska atomfällor (MOT) några hundra mikrometer från ytan av ett optiskt transparent atomchip av permanent magnetisk ferrit-granat har demonstrerats. De nödvändiga magnetfälten skapas av magnetiska mönster som skrivs magneto-optiskt i den magnetiska filmen och chipets genomskinlighet tillåter användandet av en konventionell MOT-geometri. De magnetiska mönstren kan raderas och skrivas på nytt på platsen, även under experimentets gång. Magnetiska atomfällor med ett djup upp till 1 mK kunde förverkligas med denna typs atomchip.</p>			
Nyckelord alkalimetall, optisk pumpning, coherent population trapping, laserkyllning			
ISBN (tryckt)	978-952-60-3501-7	ISSN (tryckt)	1795-2239
ISBN (pdf)	978-952-60-3502-4	ISSN (pdf)	1795-4584
Språk	Engelska	Sidantal	68 s. + bilagor 60 s.
Utgivare Institutionen för mikro- och nanoteknik, Aalto-universitetet			
Distribution av tryckt avhandling Institutionen för mikro- och nanoteknik, Aalto-universitetet			
<input checked="" type="checkbox"/> Avhandlingen är tillgänglig på nätet http://lib.tkk.fi/Diss/2010/isbn9789526035024/			

Preface

The research reported in this thesis has been carried out in the Micro and Quantum Systems group at Aalto University School of Science and Technology (formerly Helsinki University of Technology).

I am grateful to my supervisor Prof. Ilkka Tittonen for the possibility to work in an interesting field and for giving me the opportunity to participate in international conferences and summer schools at an early stage. I want to thank all the co-authors for their collaboration, especially Dr. Mikko Merimaa, Miika Heiliö, Dr. Andriy Shevchenko, and Prof. Tilman Pfau for their important contributions. I also want to thank Prof. Jacques Vanier for helpful discussions on optical pumping and Kasimir Blomstedt and Osmo Vänskä for helpful discussions on mathematical and numerical problems.

This research has been funded by the Academy of Finland, the Graduate School in Electronics, Telecommunications and Automation (GETA), and Jenny and Antti Wihuri Foundation. In addition, personal grants from the Finnish Foundation for Technology Promotion (Tekniikan edistämissäätiö), Jenny and Antti Wihuri Foundation, Emil Aaltonen Foundation, and Helsinki University of Technology are gratefully acknowledged.

I thank my parents for their continuous support and encouragement and my friends (old friends, new friends, and everyone I play or have played music with) for all the fun. Finally, I thank my family, Lili, Julius, and Adrian, for their love and support.

Espoo, November 2010

Thomas Lindvall

List of Publications

List of Publications included in the thesis

This thesis consists of an overview and of the following Publications which are referred to in the text by their Roman numerals.

- I T. Lindvall and I. Tittonen, “Effect of optical pumping on alkali-atom Doppler-limited spectra”, *J. Mod. Opt.* **54**, 2779–2793 (2007). Corrigendum, *ibid.* **55**, 2497–2500 (2008).
- II T. Lindvall and I. Tittonen, “Interaction-time-averaged optical pumping in alkali-metal-atom Doppler spectroscopy”, *Phys. Rev. A* **80**, 032505, 10 pages (2009).
- III T. Lindvall, M. Merimaa, I. Tittonen and E. Ikonen, “All-optical atomic clock based on dark states of ^{85}Rb ”. In P. Gill (ed.), *Proceedings of the 6th Symposium on Frequency Standards and Metrology*, pp. 183–190. World Scientific, Singapore, 2002.
- IV M. Merimaa, T. Lindvall, I. Tittonen, and E. Ikonen, “All-optical atomic clock based on coherent population trapping in ^{85}Rb ”, *J. Opt. Soc. Am. B* **20**, 273–279 (2003).
- V A. Shevchenko, M. Heiliö, T. Lindvall, A. Jaakkola, I. Tittonen, M. Kailola, and T. Pfau, “Trapping atoms on a transparent permanent-magnet atom chip”, *Phys. Rev. A* **73**, 051401(R), 4 pages (2006).

Author's contribution

The author has contributed significantly to all parts of this thesis. He is responsible for the initial ideas, the theoretical calculations and the preparation of the manuscripts for Publications [I–II](#). He has carried out the theoretical parts of the work in Publications [III–IV](#) and participated in the construction of the experimental setup, the measurements, and the manuscript preparation. He has designed and constructed the experimental infrastructure, the vacuum system, and parts of the optical detection system used in Publication [V](#). The experiments in Publication [V](#) were carried out by M. Heiliö, Dr. A. Shevchenko, and the author.

Other publication to which the author has contributed:

- A. Shevchenko, T. Lindvall, I. Tittonen, and M. Kaivola, “Microscopic electro-optical atom trap on an evanescent-wave mirror”, *Eur. Phys. J. D* **28**, 273–276 (2004).
- A. Shevchenko, A. Jaakkola, T. Lindvall, I. Tittonen, and M. Kaivola, “Method for obtaining high phase space density in a surface-mounted atom trap”, *Appl. Phys. B* **79**, 367–370 (2004).

Contents

Abstract	iii
Sammanfattning (Abstrakt)	v
Preface	vii
List of Publications	viii
Author's contribution	ix
Contents	xi
1 Introduction	1
2 Atoms in laser fields: semiclassical description	5
2.1 The density matrix	5
2.2 Electric dipole interaction	6
2.3 Relaxation	8
2.4 Steady-state solution of the evolution equations	9
2.5 Time-dependent solution of the evolution equations	9
2.6 Average over velocity distribution: Doppler broadening	11
2.7 Absorption of a vapor	12
3 Alkali-metal atoms	13
3.1 Light polarization versus quantization axis	14
3.2 Rubidium	14
3.3 Collisions in alkali-metal vapor cells	15
4 Optical pumping	17
4.1 Optical pumping in alkali-atom Doppler spectroscopy	17
4.2 Steady-state solution with ground-state relaxation	19
4.3 Interaction-time averaged optical pumping	19
4.3.1 Distribution of interaction times	20
4.3.2 Time-dependent absorption	21
4.3.3 Average over interaction-time and velocity distributions	23
4.4 Rubidium D ₂ spectra	26
4.4.1 Position-dependent absorption	26
4.4.2 Transmission spectra	27
4.4.3 Doppler line shifts	27
4.5 Comparison to related research	27
5 Coherent population trapping	31
5.1 Superposition states	31
5.2 CPT frequency standards	33
5.3 Buffer gas	33
5.4 Electron spin exchange	35
5.5 Density matrix for CPT in a cell with buffer gas	36

5.6	CPT frequency standard using ^{85}Rb	38
5.6.1	Experimental setup	38
5.6.2	Neon-argon buffer gas	39
5.6.3	CPT resonances	40
5.6.4	Frequency shifts	41
5.6.5	Frequency stability	43
6	Laser cooling	45
6.1	Light forces	45
6.2	Magneto-optical trap	46
6.2.1	One-dimensional model	46
6.2.2	Three-dimensional MOT	48
6.2.3	Polarization gradient cooling	48
6.2.4	MOT loading	49
6.3	Magnetic traps	50
6.4	Atom chips	51
6.5	Microscopic magneto-optical traps	53
6.5.1	Ferrite-garnet films	53
6.5.2	Experimental setup	53
6.5.3	Results	56
7	Conclusions	57
	References	59
	Abstracts of Publications I–V	66
	Erratum	68

1

Introduction

As highly reactive, the alkali metals are not found in elemental form in Nature. Although certain alkali-metal compounds have been known since medieval times, an alkali metal was isolated for the first time in 1807, when Sir Humphry Davy extracted potassium through electrolysis of molten caustic potash (KOH) [1]. He observed how the metallic luster of the element rapidly vanished as it reacted with the water in the air and again formed hydroxide. Shortly thereafter he isolated sodium from sodium hydroxide (NaOH) in a similar process [1]. Lithium was discovered by J. A. Arfvedson in 1817 and soon isolated independently by W. T. Brande [2] and Davy [3].

Also in the early 19th century, J. Fraunhofer invented the spectrometer and used it to analyze hundreds of dark absorption lines in the optical spectrum of the Sun [4]. In 1860 G. Kirchhoff and R. Bunsen published a study on chemical analysis using a spectrometer [5], where they studied the flame test spectra of the known alkali metals lithium, sodium, and potassium, and among other things noted the bright yellow sodium D lines. This technique led to the discovery of two new alkali metals, cesium and rubidium [6]. The study of spectral lines laid the foundation for atomic physics and led to the Bohr atom model [7, 8].

The advances in vacuum technology during the late 19th century and early 20th century enabled experimental work in atomic physics. The first experiments with molecular beams were performed by L. Dunoyer in 1911 [9], verifying that sodium atoms travel in straight lines in vacuum. The molecular beam technique was adopted and developed by O. Stern, which led to the classical Stern-Gerlach experiments carried out during 1920–1923 [10–14]. These experiments proved spatial quantization experimentally, demonstrated that silver atoms have an intrinsic angular momentum, and determined a value for the Bohr magneton.

Stern's group continued its pioneering work with molecular beams and in 1933 O. R. Frisch reported the deflection of a sodium beam using resonant light from a sodium lamp [15]. Although the radiation pressure on macroscopic surfaces had been observed about 30 years earlier [16–18], this was the first demonstration of radiation pressure on atoms and thus a ground-breaking step towards the field of laser cooling and trapping.

In 1938 I. I. Rabi, who ten years earlier as a post-doc had worked in Stern's laboratory, invented the molecular beam magnetic resonance method [19, 20]. In this method, a molecular beam passes through a homogeneous magnetic field strong

enough to decouple the nuclear magnetic moments from each other and from the rotational moment of the molecules. A transversal oscillating field induces transitions to other magnetic states if its frequency is close to the Larmor frequency of the nuclear moment in the strong homogeneous field. This new technique was soon used to measure the hyperfine structure of the alkalis Li, K [21], Na, Rb, and Cs [22]. In 1946 F. Bloch introduced the Bloch equations that describe how the magnetization in nuclear magnetic resonance (NMR) evolves in time [23]. Much of the formalism developed by Rabi and Bloch for NMR was later adopted to the semiclassical description of laser-atom interaction as is described in Chapter 2.

The possibility of using the beam resonance method as a time and frequency standard was considered by the Rabi group already in 1939 [24]. Ten years later N. F. Ramsey invented the separated oscillatory field method [25, 26], which allowed much narrower linewidths to be obtained. This method led to the first practical laboratory cesium beam frequency standard in 1955 [27] and to the first commercial model one year later [24]. Since 1967 the cesium atom is used to define the SI unit of time: “The second is the duration of 9 192 631 770 periods of the radiation corresponding to the transition between the two hyperfine levels of the ground state of the cesium atom 133” [24].

The method of optical pumping, i.e., the selective population or depletion of certain atomic levels by absorption followed by spontaneous emission, was suggested by A. Kastler in 1950 [28] and experimentally realized a few years later by J. Brossel, Kastler, and J. Winter [29] and by W. B. Hawkins and R. H. Dicke [30]. These first experiments were carried out with sodium beams. Experiments in vapor cells showed that alkali-wall collisions destroyed the polarization with nearly 100 % probability. Two techniques were developed to circumvent this problem: the use of a buffer gas that increases the diffusion time between wall collisions without destroying the polarization, and coating the inner cell walls with a nonrelaxing material [31]. There was an extensive amount of work on optical pumping in the 1950s and 1960s, e.g., measuring hyperfine structure intervals, Zeeman and Stark splittings, as well as pressure shifts and different relaxation cross sections. Many of these results are summarized in a review by W. Happer [31].

The maser (Microwave Amplification by Stimulated Emission of Radiation) was developed in the 1950s and in the 1960s work with both hydrogen and rubidium masers as frequency standards started [32]. In 1958 A. L. Schawlow and C. H. Townes suggested the extension of maser techniques to the infrared and optical region [33]. Soon the first optical maser, the laser (Light Amplification by Stimulated Emission of Radiation), was realized using ruby as the active medium [34]. The recently developed optical pumping technique enabled the achievement of the population inversion required for lasing.

The development of tunable, narrow-linewidth single-mode lasers in the 1970s was a major breakthrough in optical spectroscopy. In addition, the intense and coherent light of the lasers gave rise to a whole new field, non-linear optics. The possibility to use multiple phase-coherent laser modes also made it possible to observe new coherence phenomena in atomic multi-level systems. One such phe-

nomenon is coherent population trapping (CPT), first discovered in sodium atoms by G. Alzetta *et al.* in 1976 [35]. CPT occurs in atomic three-level Λ systems when the atoms are pumped into a coherent, nonabsorbing superposition of the two ground levels. The CPT resonances can be very narrow and are suitable candidates for frequency references, as will be discussed in Chapter 5.

Laser cooling was proposed in 1975 by T. W. Hänsch and A. L. Schawlow for neutral atoms [36] and by D. J. Wineland and H. Dehmelt for trapped ions [37]. The first successful method to decelerate an atomic beam using a laser was the so-called Zeeman slower, where the spatially varying magnetic field of a solenoid keeps the decelerating atoms resonant with the laser, developed and demonstrated by W. D. Phillips and H. Metcalf in 1982 [38]. Optical molasses, the viscous confinement and cooling (but not trapping) of atoms using radiation pressure was demonstrated by S. Chu *et al.* in 1985 [39]. A major experimental breakthrough occurred in 1987, when the first magneto-optical trap (MOT) was demonstrated using sodium [40]. The MOT soon became a workhorse in the research of cold atoms. Another milestone was the achievement of Bose-Einstein condensation of rubidium-87 in 1995 [41]. During the past decade, one trend in atom trapping has been the development of microscopic traps integrated on a surface, an atom chip, see Chapter 6.4.

We have seen that the alkali metals have had an important role in optical and atomic physics from the very beginning. The difficulty of handling these reactive elements is outweighed by several beneficial properties. Their high vapor pressures allow significant absorption at room temperature as well as simple generation of atomic beams. With a single valence electron they have a relatively simple level structure. The transitions between the ground and the first excited states are strong and lie in the visible or near-infrared regions, which have made it easy to generate resonant light, first using alkali lamps, then using dye lasers and more recently using inexpensive and readily available semiconductor lasers. Their hyperfine structure and Zeeman sublevels make them well suited for radiofrequency manipulation and creates multi-level systems that can be used to observe nonlinear effects even at very low light intensities.

This thesis consists of seven chapters. Chapter 2 introduces the semiclassical treatment of laser-atom interaction. A brief summary of the atomic and optical properties of alkali-metal atoms and rubidium in particular is found in Chapter 3. The topic of Chapter 4 is optical pumping in alkali-metal atoms and Chapter 5 describes coherent population trapping and its application for frequency standards. Chapter 6 discusses laser cooling, with emphasis on micro-MOTs and atoms chips. Chapter 7 summarizes the results and discusses their role within the framework of related research.

2

Atoms in laser fields: semiclassical description

In the semiclassical description of the interaction between laser light and atoms, a classical electromagnetic field interacts with a quantized atom. After introducing the density matrix, the simple case of a two-level atom interacting with a near-resonant laser field will be considered as an example.

2.1 The density matrix

In textbook quantum mechanics all information about a pure state is given by the state vector $|\Psi\rangle$, which can be determined, excluding the arbitrary overall phase, by performing the measurements corresponding to a complete set of commuting observables. However, a pure state is not the most general kind of state. In fact, most systems observed in the laboratory are not in a pure state, but in a non-pure or mixed state, also referred to as a statistical mixture of states. A frequent reason is that only a part of the total system is observed. For example, for an atom that undergoes spontaneous emission, it is usually neither possible nor desirable to observe the state (wave vector and polarization) of the emitted photons. Although the total system, the atom and the electromagnetic field, might be in a pure state, the reduced system consisting of the atom alone will be in a mixed state.

To treat mixed states one needs to define the density operator or state operator [42, 43]. It can be written as

$$\rho = \sum_i p_i |\psi_i\rangle \langle \psi_i|, \quad (2.1)$$

where, assuming that the states $|\psi_i\rangle$ are orthogonal, p_i is the probability to be in state $|\psi_i\rangle$. However, this way of writing the density operator as a statistical mixture of pure-state density operators is not unique, but often there is natural choice of states, e.g., the atomic eigenstates. The expectation value of an operator O can be expressed as

$$\langle O \rangle = \sum_i p_i \langle \psi_i | O | \psi_i \rangle = \text{Tr } \rho O. \quad (2.2)$$

Some general properties of the density operator are:

- The density operator is normalized:¹ $\text{Tr } \rho = 1$.
- The density operator is Hermitian (self-adjoint): $\rho = \rho^\dagger$.
- The density operator is positive: $\langle \phi | \rho | \phi \rangle \geq 0$ for all $|\phi\rangle$.

The evolution equation for the density operator can be derived from the Schrödinger equation and is given by the *Liouville-von Neumann equation*

$$i\hbar \frac{d\rho}{dt} = [H, \rho], \quad (2.3)$$

where H is the Hamiltonian.

In practice it is often necessary to perform measurements on a large number of identical systems in order to obtain an observable signal. All the systems are generally not in the same state, but their statistical properties can be described by the ensemble averaged density operator or statistical operator [44].² The use of the evolution equation (2.3) requires that all the systems have the same Hamiltonian, so any summation over systems with different Hamiltonians must be performed after the equation has been integrated [46].

The matrix representation of the density operator is called the density matrix. It obviously depends on the basis $\{|\phi_n\rangle\}$ and its elements are given by $\rho_{ij} = \langle \phi_i | \rho | \phi_j \rangle$. Often the terms density matrix and operator are used interchangeably.

The density matrix for a two-level atom in the basis $\{|e\rangle, |g\rangle\}$ is given by

$$\rho = \begin{pmatrix} \rho_{ee} & \rho_{eg} \\ \rho_{ge} & \rho_{gg} \end{pmatrix}. \quad (2.4)$$

The diagonal elements ρ_{ee} and ρ_{gg} give the occupation probabilities of states $|e\rangle$ and $|g\rangle$, respectively, and are hence called *populations*. For a pure state $|\Psi\rangle = c_e|\psi_e\rangle + c_g|\psi_g\rangle$, the populations are simply $\rho_{ii} = |c_{ii}|^2$. Still considering this pure state, we see that in order for the nondiagonal matrix element $\rho_{ij} = c_i c_j^*$ ($i \neq j$) to be nonzero, the system must be in a coherent superposition of the two states $|e\rangle$ and $|g\rangle$. Hence these elements are called *coherences*. If the system under consideration is an ensemble, it is not enough that some of its members is in a superposition. The phases of the individual members must be correlated, otherwise the matrix element will average to zero in the ensemble average $\rho_{ij} = \overline{c_i c_j^*} = \overline{|c_i c_j| e^{i(\theta_i - \theta_j)}}$ [44].

2.2 Electric dipole interaction

As an example, we will study the interaction between a two-level atom and a near-resonant laser field. The atomic Hamiltonian is

$$H_A = \hbar(\omega_e |e\rangle\langle e| + \omega_g |g\rangle\langle g|), \quad (2.5)$$

¹This does not hold for an open (sub)system with decay to levels not included in ρ .

²Strictly speaking, an ensemble is the abstract infinite set of all systems that can result from a particular state preparation procedure [45], but in practice it can be compared to measurements performed on an ensemble of identical and noninteracting coexisting systems.

where $\hbar\omega_i$ is the energy of state $|i\rangle$. As the optical wavelength typically is several hundred nm, while the effective size of atoms typically is less than 1 nm, one can use the electrical dipole approximation to describe the atom-laser interaction,

$$V = -\boldsymbol{\mu} \cdot \mathbf{E}(\mathbf{R}, t), \quad (2.6)$$

where the field is evaluated at the center-of-mass position of the atom, \mathbf{R} . The laser field is described by a plane wave of frequency ω and wave number k propagating in the z -direction

$$\mathbf{E}(\mathbf{R}, t) = \frac{1}{2} \mathbf{u} \mathcal{E} e^{i(\omega t - kz)} + \text{c.c.}, \quad (2.7)$$

where \mathbf{u} is the polarization vector, \mathcal{E} is the electric field amplitude, and c.c. stands for complex conjugate. The electric dipole operator for the two-level atoms is given by

$$\boldsymbol{\mu} = \begin{pmatrix} 0 & \boldsymbol{\mu}_{eg} \\ \boldsymbol{\mu}_{ge} & 0 \end{pmatrix}. \quad (2.8)$$

The phase of the dipole element depends of the relative phase of the ground and excited state wavefunctions, $\boldsymbol{\mu}_{eg} = \int \phi_e^*(\mathbf{r}) \mathbf{e} r \phi_g(\mathbf{r}) d\mathbf{r}$, and since the overall phases are arbitrary, one can choose them so that $\boldsymbol{\mu}$ is real. For a two-level atom the dipole moment is parallel to the polarization, and one can set $\boldsymbol{\mu}_{eg} \cdot \mathbf{u} = \boldsymbol{\mu}_{ge} \cdot \mathbf{u} = \mu$.

Defining the two-level *Rabi frequency*

$$\Omega = \frac{\mu \mathcal{E}}{\hbar}, \quad (2.9)$$

the interaction Hamiltonian can be written as

$$V = -\frac{\hbar\Omega}{2} (|e\rangle\langle g| + |g\rangle\langle e|) \left(e^{i(\omega t - kz)} + \text{c.c.} \right). \quad (2.10)$$

Using the total Hamiltonian $H = H_A + V$, the Liouville-von Neumann equation (2.3) gives the following evolution equations for the density matrix elements

$$\frac{d\rho_{ee}}{dt} = i\Omega(\rho_{ge} - \rho_{eg}) \cos(\omega t - kz), \quad (2.11a)$$

$$\frac{d\rho_{gg}}{dt} = -i\Omega(\rho_{ge} - \rho_{eg}) \cos(\omega t - kz), \quad (2.11b)$$

$$\frac{d\rho_{ge}}{dt} = i\Omega(\rho_{ee} - \rho_{gg}) \cos(\omega t - kz) + i\rho_{ge}\omega_{eg}, \quad (2.11c)$$

where we have defined $\omega_{eg} = \omega_e - \omega_g$. One can get rid of the oscillation of the optical coherence at the frequency of the laser field through a *transformation to a rotating frame* $\tilde{\rho}_{ge} = \rho_{ge} e^{-i(\omega t - kz)}$. In addition, one usually employs the *rotating wave approximation*³ (RWA) by neglecting terms oscillating at twice the optical fre-

³The term RWA originates from the equivalence between a two-level atom and a spin $\frac{1}{2}$ in a longitudinal static magnetic field interacting with a transversal oscillating field. The transversal field can be decomposed into two components, rotating around the longitudinal axis in opposite directions. If the frequency of the transversal field is close to the Larmor precession frequency of the spin in the longitudinal field, the co-rotating component will follow the spin and be able to act on it, whereas the counter-rotating component will rotate too rapidly relative to the spin to have an appreciable effect and can be neglected.

quency, i.e., by setting $e^{\pm i(\omega t - kz)} \cos(\omega t - kz) \approx \frac{1}{2}$. Note that if one wants to allow for a complex Rabi frequency, $\Omega = |\Omega|e^{i\phi_\Omega}$, it merely gives rise to an additional phase shift in the transformation to the rotating frame.

If the atoms have a non-negligible velocity component along the direction of the laser beam, this can be accounted for by using the *convective derivative* in Eq. (2.3),

$$\frac{d\rho}{dt} = \left(\frac{\partial}{\partial t} + v_z \frac{\partial}{\partial z} \right) \rho. \quad (2.12)$$

For moving atoms, using the RWA in the rotating frame, Eqs. (2.11) become

$$\frac{d\rho_{ee}}{dt} = i\frac{\Omega}{2}(\tilde{\rho}_{ge} - \tilde{\rho}_{eg}) = -\Omega\tilde{\rho}_{ge}^i, \quad (2.13a)$$

$$\frac{d\rho_{gg}}{dt} = -i\frac{\Omega}{2}(\tilde{\rho}_{ge} - \tilde{\rho}_{eg}) = \Omega\tilde{\rho}_{ge}^i, \quad (2.13b)$$

$$\frac{d\tilde{\rho}_{ge}}{dt} = i\frac{\Omega}{2}(\rho_{ee} - \rho_{gg}) - i(\omega - \omega_{eg} - kv_z)\tilde{\rho}_{ge}, \quad (2.13c)$$

where $\tilde{\rho}_{ge}^i$ denotes the imaginary part $\text{Im} \tilde{\rho}_{ge}$. We see that the atomic resonance frequency now has been replaced by the detuning $\delta_0 = \omega - \omega_{eg}$ and that the convective derivative included the *Doppler shift* $-kv_z$. These can be combined to the velocity dependent detuning $\delta(v_z) = \delta_0 - kv_z$. The laser is said to be red-detuned when $\delta_0 < 0$ and blue-detuned when $\delta_0 > 0$.

2.3 Relaxation

Relaxation terms can be added phenomenologically to the evolution equations. Spontaneous emission causes the excited state to decay at the rate $\Gamma_e = \Gamma$, whereas the ground state is stable, $\Gamma_g = 0$. The relaxation rate for the optical coherence consists of a non-adiabatic and an adiabatic part, $\Gamma_{ge} = \Gamma_{ge}^{\text{non-adiab.}} + \Gamma_{ge}^{\text{adiab.}}$ [32]. The term non-adiabatic refers to the fact that there is a net exchange of energy with the environment, and this rate is obtained from the relaxation rates of the populations, $\Gamma_{ge}^{\text{non-adiab.}} = \frac{1}{2}(\Gamma_e + \Gamma_g) = \Gamma/2$. The adiabatic part of the relaxation is due to mechanisms that cause dephasing but no population transfer, such as weak collisions, and will be considered in Section 5.3. With the relaxation terms, Eqs. (2.13) become

$$\frac{d\rho_{ee}}{dt} = -\Omega\tilde{\rho}_{ge}^i - \Gamma\rho_{ee}, \quad (2.14a)$$

$$\frac{d\rho_{gg}}{dt} = \Omega\tilde{\rho}_{ge}^i + \Gamma\rho_{ee}, \quad (2.14b)$$

$$\frac{d\tilde{\rho}_{ge}}{dt} = -\left[\frac{\Gamma}{2} + i\delta(v_z) \right] \tilde{\rho}_{ge} + i\frac{\Omega}{2}(\rho_{ee} - \rho_{gg}). \quad (2.14c)$$

2.4 Steady-state solution of the evolution equations

The steady-state solutions for Eqs. (2.14) can easily be obtained by setting the time derivatives to zero and using $\text{Tr } \rho = \rho_{ee} + \rho_{gg} = 1$,

$$\rho_{ee} = \frac{(\Omega/2)^2}{\delta^2(v_z) + (\Gamma/2)^2 + 2(\Omega/2)^2}, \quad (2.15a)$$

$$\rho_{gg} = \frac{\delta^2(v_z) + (\Gamma/2)^2 + (\Omega/2)^2}{\delta^2(v_z) + (\Gamma/2)^2 + 2(\Omega/2)^2}, \quad (2.15b)$$

$$\tilde{\rho}_{ge} = -\frac{[\delta(v_z) + i\Gamma/2]\Omega/2}{\delta^2(v_z) + (\Gamma/2)^2 + 2(\Omega/2)^2}. \quad (2.15c)$$

A lot can be interpreted from these solutions. We see how both populations approach 1/2 if the laser intensity approaches infinity (strong saturation). The denominators show that the *power broadened* linewidth is given by

$$\Gamma_{\text{power}} = \Gamma \sqrt{1 + 2 \left(\frac{\Omega}{\Gamma} \right)^2} = \Gamma \sqrt{1 + \frac{I}{I_s}}, \quad (2.16)$$

where we have defined the two-level *saturation intensity* $I_s = \pi \hbar c \Gamma / 3 \lambda^3$ [47], where c is the speed of light. The on-resonance saturation parameter is defined as $s_0 = I / I_s$. As derived in Appendix A of Publication I, the imaginary part of the optical coherence describes the absorption of an atomic vapor, whereas the real part describes the refraction.

2.5 Time-dependent solution of the evolution equations

The time-dependent solution of Eqs. (2.14) can easily be obtained by numerical integration. Fig. 2.1 shows how the absorption (actually $-\tilde{\rho}_{ge}^i$) approaches the steady-state value given by Eq. (2.15c) for the initial conditions $\rho_{gg} = 1$, $\rho_{ee} = \rho_{ge} = 0$ at two detunings. At $\Omega = \Gamma$, the Rabi oscillations are heavily damped at resonance; off resonance a few oscillations can be seen.

The analytical time-dependent solution can be obtained using the Laplace transform $R(s) = \int_0^\infty \rho(t) e^{-st} dt$. Using the initial conditions $\rho_{gg} = 1$ and $\rho_{ee} = \tilde{\rho}_{ge} = 0$, Eqs. (2.14) become

$$sR_{ee} = -\Omega R_{ge}^i - \Gamma R_{ee}, \quad (2.17a)$$

$$sR_{gg} - 1 = \Omega R_{ge}^i + \Gamma R_{ee}, \quad (2.17b)$$

$$sR_{ge} = -\left[\frac{\Gamma}{2} + i\delta(v_z) \right] R_{ge} + i\frac{\Omega}{2}(R_{ee} - R_{gg}). \quad (2.17c)$$

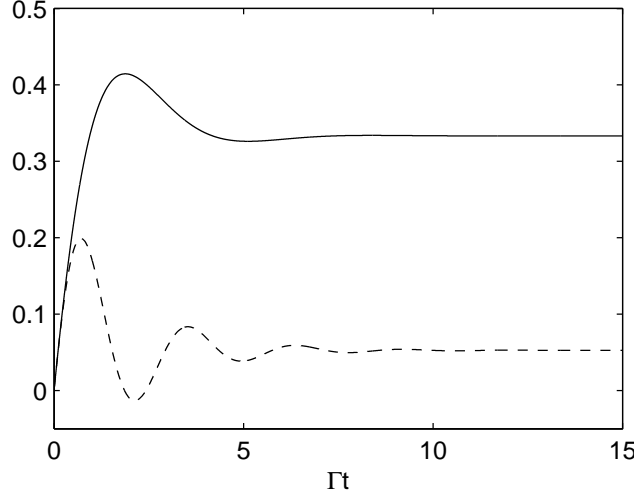


Figure 2.1. Absorption ($-\tilde{\rho}_{ge}^i$) as a function of time for a two-level system with the initial conditions $\rho_{gg} = 1$, $\rho_{ee} = \rho_{ge} = 0$ at resonance (solid line) and for $\delta = \Gamma$ (dashed line). $\Omega = \Gamma$.

The solution of this algebraic equation system is

$$R_{ee} = 2 \left(s + \frac{\Gamma}{2} \right) \left(\frac{\Omega}{2} \right)^2 D^{-1}, \quad (2.18a)$$

$$R_{gg} = \left\{ (s + \Gamma) \left[\left(s + \frac{\Gamma}{2} \right)^2 + \delta^2(v_z) \right] + 2 \left(s + \frac{\Gamma}{2} \right) \left(\frac{\Omega}{2} \right)^2 \right\} D^{-1}, \quad (2.18b)$$

$$R_{ge} = -(s + \Gamma) \left[\delta(v_z) + i \left(s + \frac{\Gamma}{2} \right) \right] \frac{\Omega}{2} D^{-1}, \quad (2.18c)$$

where the common denominator is $D = s^4 + 2\Gamma s^3 + [\delta^2(v_z) + 5\Gamma^2/4 + \Omega^2] s^2 + [\delta^2(v_z) + \Gamma^2/4 + \Omega^2/2] \Gamma s$. If we can solve the roots s_i of the equation $D = 0$, we can write the solutions (2.18) as partial fractions $R_{ij} = \sum_{k=1}^4 R_{ij,k} / (s - s_k)$, where the coefficients $R_{ij,k}$ can be solved from $R_{ij,k} = \lim_{s \rightarrow s_k} (s - s_k) R_{ij}$. The time dependence is then given by

$$\rho_{ij}(t) = \sum_{k=1}^4 R_{ij,k} e^{s_k t}. \quad (2.19)$$

The exact analytic expressions for the roots s_i are not very transparent. Simple expressions can, however, be obtained in the following special cases:

- **No spontaneous decay, $\Gamma = 0$:**

$$\rho_{ee} = \frac{\Omega^2}{2\Omega'^2} (1 - \cos \Omega' t), \quad (2.20a)$$

$$\tilde{\rho}_{ge}^i = -\frac{\Omega}{2\Omega'} \sin \Omega' t. \quad (2.20b)$$

The system undergoes undamped Rabi oscillations at the generalized Rabi frequency $\Omega' = \sqrt{\Omega^2 + \delta^2}$, see Fig. 2.2(a). The amplitude of the oscillations decrease off resonance.

- **Weak intensity limit, $\Omega \ll \Gamma$:**

$$\rho_{ee} = \frac{(\Omega/2)^2}{\delta^2 + (\Gamma/2)^2} \left(1 + e^{-\Gamma t} - 2e^{-\Gamma t/2} \cos \delta t \right), \quad (2.21a)$$

$$\tilde{\rho}_{ge}^i = -\frac{\Omega/2}{\delta^2 + (\Gamma/2)^2} \left[\frac{\Gamma}{2} - e^{-\Gamma t/2} \left(\frac{\Gamma}{2} \cos \delta t - \delta \sin \delta t \right) \right]. \quad (2.21b)$$

Because the field is weak, the Rabi oscillations are heavily damped and occur only off resonance, at the frequency δ , see Fig. 2.2(b). The figure also shows that this approximation is good already for $\Omega = 0.1\Gamma$, except exactly at resonance.

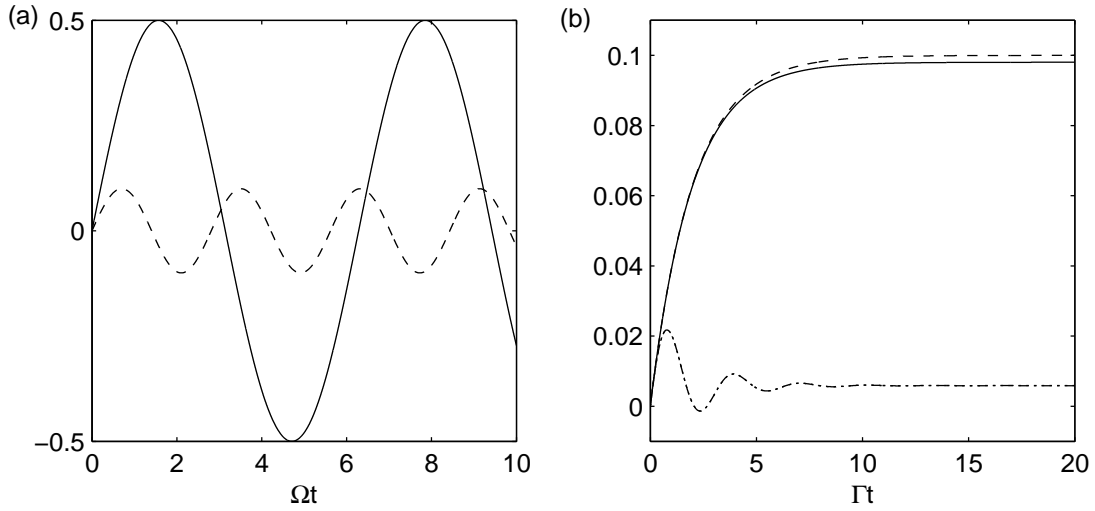


Figure 2.2. Absorption ($-\tilde{\rho}_{ge}^i$) as a function of time for an atomic system with the initial conditions $\rho_{gg} = 1, \rho_{ee} = \rho_{ge} = 0$. (a) No spontaneous decay: $\delta = 0$ (solid) and $\delta = 2\Omega$ (dashed). (b) Weak intensity limit, $\Omega = 0.1\Gamma$: At resonance, the approximation (dashed) rises slightly higher than the numerical solution (solid), but for $\delta = 2\Gamma$ the approximation (dotted) and numerical solution (dash-dotted) cannot be distinguished.

2.6 Average over velocity distribution: Doppler broadening

For a thermal vapor, the density matrix elements, steady-state or time-dependent, must be averaged over the longitudinal velocity distribution

$$\langle \rho_{ij} \rangle_{v_z} = \frac{1}{\sqrt{\pi} v_{\text{mp}}} \int_{-\infty}^{+\infty} \rho_{ij}(v_z) e^{-v_z^2/v_{\text{mp}}^2} dv_z, \quad (2.22)$$

where $v_{\text{mp}} = (2k_{\text{B}}T/m)^{1/2}$ is the most probable velocity. As an example, we consider the velocity average of the steady-state solution for the imaginary part of the coherence given in Eq. (2.15c). Defining the integration variable $x = kv_z$, it becomes

$$\langle \tilde{\rho}_{ge}^i \rangle_{v_z} = -\frac{\Gamma\Omega/4}{\sqrt{\pi}kv_{\text{mp}}} \int_{-\infty}^{+\infty} \frac{e^{-x^2/(kv_{\text{mp}})^2}}{(\delta_0 - x)^2 + (\Gamma/2)^2 + 2(\Omega/2)^2} dx. \quad (2.23)$$

The resulting line shape is the convolution of the Lorentzian homogeneous line and the Gaussian velocity distribution and is called a Voigt profile. The convolution integral cannot be evaluated analytically, but if the Doppler width $\Delta\omega_{\text{D}} = 2(\ln 2)^{1/2}kv_{\text{mp}}$ is much larger than the natural linewidth Γ , the exponential function will be approximately constant, $e^{-x^2/(kv_{\text{mp}})^2} \approx e^{-\delta_0^2/(kv_{\text{mp}})^2}$, over the frequency range where the Lorentzian is non-negligible. It can thus be taken out of the integral, which then can be integrated to give the Gaussian approximation

$$\langle \tilde{\rho}_{ge}^i \rangle_{v_z} \approx -\frac{\sqrt{\pi}\Omega/2}{kv_{\text{mp}}\sqrt{1 + I/I_s}} e^{-\delta_0^2/(kv_{\text{mp}})^2}. \quad (2.24)$$

2.7 Absorption of a vapor

The absorption coefficient depends on the imaginary part of the optical coherence, as derived in Appendix A of Publication I,

$$\alpha = -\frac{2kN\mu}{\varepsilon_0\mathcal{E}} \langle \tilde{\rho}_{ge}^i \rangle_{v_z} = -\frac{2kN\mu^2}{\varepsilon_0\hbar\Omega} \langle \tilde{\rho}_{ge}^i \rangle_{v_z}, \quad (2.25)$$

where N is the number density of the atoms and ε_0 is the permittivity of vacuum. The absorption coefficient generally depends on the light intensity due to saturation and optical pumping.

The absorption of light traveling in the z -direction in a medium is described by the equation

$$\frac{dI(\nu, z)}{dz} = -\alpha(\nu, I)I(\nu, z), \quad (2.26)$$

where $I(\nu, z)$ is the light intensity at frequency ν and $\alpha(\nu, I)$ is the absorption coefficient at this frequency and intensity. If the absorption in the medium is small, the intensity dependence and thus also the z dependence of the absorption coefficient can be neglected and Eq. (2.26) can be integrated to give the relative transmission

$$T(\nu) = \frac{I(\nu, l)}{I_0} = e^{-\alpha(\nu)l}, \quad (2.27)$$

where I_0 is the incident intensity and l is the length of the absorbing medium.

3

Alkali-metal atoms

The alkali metals have closed (filled) electronic shells with one valence electron. The closed shells do not contribute to the electronic angular momenta, so the atoms have the orbital angular momentum $\mathbf{L} = \mathbf{l}$, spin angular momentum $\mathbf{S} = \mathbf{s}$, and total electronic angular momentum $\mathbf{J} = \mathbf{j}$. Here the capital symbols refer to the angular momenta of the atom, whereas the lower-case symbols refer to those of the valence electron. The total (electronic) angular momentum is $\mathbf{J} = \mathbf{L} + \mathbf{S}$ and so the corresponding quantum number J takes the values $|L - S|, |L - S| + 1, \dots, L + S$. The states are labeled using the Russell-Saunders [47] or spectroscopic notation $n^{2S+1}L_J$, where n is the principal quantum number of the valence electron.

Because of the spin-orbit interaction, proportional to $\mathbf{L} \cdot \mathbf{S}$, states with different values of J have different energies. This so-called *fine-structure splitting* splits the first excited state into the states $n^2P_{1/2}$ and $n^2P_{3/2}$. The transitions from the ground state $n^2S_{1/2}$ to these two states are known as the D₁ and D₂ lines, respectively. From the point of view of laser spectroscopy, the fine-structure splitting is very large, ranging from 0.5 THz for sodium to 16.6 THz for cesium, and thus the two states are usually considered separately.

The level structure becomes a bit more complicated when one takes the interaction between the total angular momentum of the electron \mathbf{J} and the nuclear spin \mathbf{I} into account. These form the total angular momentum $\mathbf{F} = \mathbf{I} + \mathbf{J}$. Again, states with different F , ranging from $|I - J|$ to $I + J$, have different energies. This is the *hyperfine structure*. The ground state is split into two hyperfine levels with a separation of ~ 200 – 9200 MHz, depending on the particular element. The excited state $2P_{1/2}$ is split into two hyperfine levels with a typical separation of the order of 100 – 1000 MHz, whereas the $2P_{3/2}$ state is split into four levels with typical separations of the order of 10 – 100 MHz.

Each hyperfine state is further split into $2F + 1$ *Zeeman sublevels*, labeled by the magnetic quantum number $m_F = -F, -F + 1, \dots, F$. In the absence of a magnetic field these are degenerate, but a field lifts this degeneracy. For low fields the Zeeman shift is approximately linear, $\Delta E = g_F \mu_B m_F B$, where g_F is the hyperfine Landé factor and $\mu_B = e\hbar/2m_e$ is the Bohr magneton (e is the elementary charge and m_e is the electron mass). The magnetic quantum number m_F is the projection of \mathbf{F} on the magnetic field B ; the field defines the *quantization axis*.

3.1 Light polarization versus quantization axis

In multi-level atoms, the orientation of the atomic dipole moment with respect to the polarization of light has to be considered. The polarization experienced by the atoms can be obtained by expanding the polarization vector of the light using the spherical unit vectors [48]

$$\mathbf{u}_{\pm 1} = \mp \frac{1}{\sqrt{2}}(\mathbf{u}_x \pm i\mathbf{u}_y), \quad \mathbf{u}_0 = \mathbf{u}_z, \quad (3.1)$$

where \mathbf{u}_z is the direction of the quantization axis. The vectors $\mathbf{u}_{\pm 1}$ correspond to circularly polarized light (σ^\pm), whereas \mathbf{u}_0 correspond to linearly polarized light (π). As an example, a linearly polarized laser beam traveling in the \mathbf{u}_z direction must be decomposed into its σ^+ and σ^- components and is referred to as σ light.

Because of the conservation of angular momentum, σ^\pm light drive transitions with $\Delta m_F = \pm 1$, whereas π light drive transitions with $\Delta m_F = 0$.

3.2 Rubidium

Rubidium has the atomic number $Z = 37$ and thus its electron configuration is $1s^2 2s^2 2p^6 3s^2 3p^6 4s^2 3d^{10} 4p^6 5s$. Natural rubidium is an isotopic mixture of ^{85}Rb (relative abundance 72.17 %) with an atomic mass of 84.91178974 u and ^{87}Rb (relative abundance 27.83 %) with an atomic mass of 86.90918053 u [49]. In principle only ^{85}Rb is stable, but ^{87}Rb has a half-life of 4.9×10^{10} years [49] and can for all practical purposes be considered stable, as it would take approximately 3×10^9 years for its abundance to decrease by 1 %.

Since the two isotopes have different nuclear spins ($I = 5/2$ for ^{85}Rb and $I = 3/2$ for ^{87}Rb), they also have different hyperfine splittings. The ground-state hyperfine splitting of ^{85}Rb is 3.036 GHz, whereas that of ^{87}Rb is 6.835 GHz. Also the excited-state hyperfine splittings are approximately twice as large for ^{87}Rb . The ground and the first excited states of ^{87}Rb and ^{85}Rb are shown in Fig. 3.1. The hyperfine splittings are calculated using the hyperfine constant values recommended in Ref. [50].

The natural linewidth is approximately 6 MHz for all the D line transitions and the dipole moment of the closed transition $|F = I + 1/2, m_F = F\rangle \rightarrow |F' = F + 1, m'_F = F'\rangle$ at 780 nm is $\sim 2.5 \times 10^{-29}$ Cm.

There are considerable differences between the different published vapor pressure data and formulae for rubidium. A frequently cited source is Nesmeyanov's formula [51]

$$\log(p/\text{Pa}) = \log_{10} 133.322 + A + B(T/\text{K})^{-1} + CT/\text{K} + D \log_{10} T/\text{K}, \quad (3.2)$$

where $A = -94.04826$, $B = -1961.258$, $C = -0.03771687$, and $D = 42.57526$ in the solid phase, and $A = 15.88253$, $B = -4529.635$, $C = 0.00058663$, and $D = -2.99138$ in the liquid phase. The term $\log_{10} 133.322$ is added to convert from

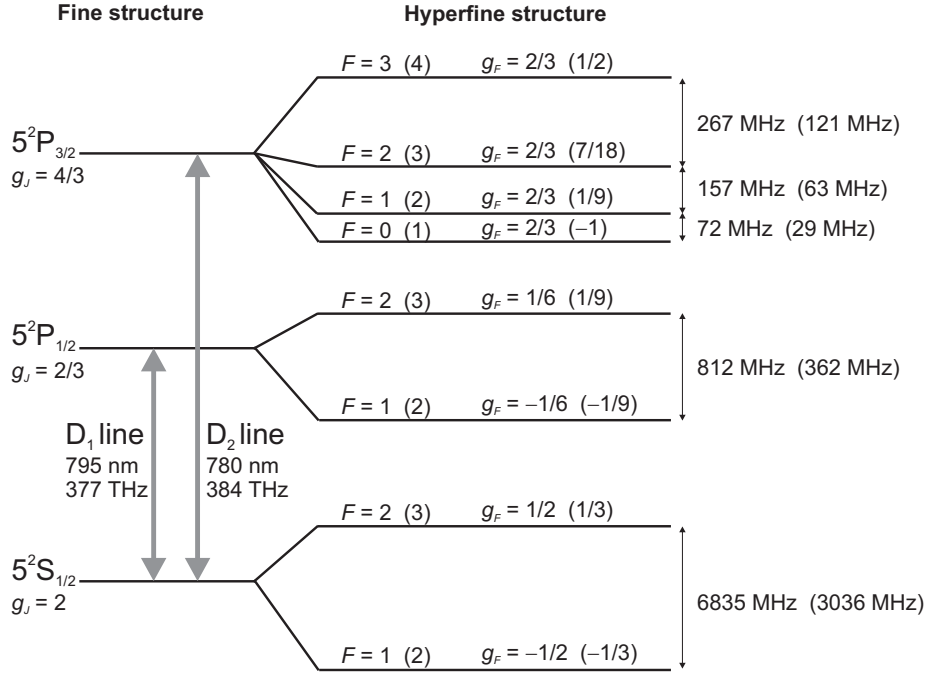


Figure 3.1. Level scheme for the ground and first excited states of ^{87}Rb (^{85}Rb).

torr to Pa. However, it has been suggested that Nesmeyanov's vapor pressures may be in error by as much as a factor of 1.5 [52] and the 2008 *CRC Handbook of Chemistry and Physics* [49] refers to Alcock *et al.* [53] and gives the formula

$$\log(p/\text{Pa}) = 5.006 + A' + B'(T/\text{K})^{-1}, \quad (3.3)$$

where $A' = 4.857$ and $B' = -4215$ for solid Rb (298–312.45 K) and $A' = 4.312$ and $B' = -4040$ for liquid Rb (312.45–550 K). These equations reproduce the experimental input data to $\pm 5\%$ or better in the temperature ranges mentioned, but the experimental uncertainties may be larger [53].

At 298 K, the Rb vapor pressure is 5.2×10^{-7} mbar [53] (the value obtained from [51] is about 25 % lower). It depends strongly on the temperature: a 1-K increase (decrease) in temperature corresponds to about a 10 % increase (decrease) in the pressure.

3.3 Collisions in alkali-metal vapor cells

At room temperature the rubidium number density N is of the order of 10^{16} m^{-3} [53]. The cross section for Rb-Rb collisions is $\sigma_{\text{Rb-Rb}} \approx 1.4 \times 10^{-17} \text{ m}^2$ [32], which gives the mean free path $\ell_{\text{Rb}} = 2^{-1/2}(N\sigma_{\text{Rb-Rb}})^{-1} \approx 5 \text{ m}$. As the typical dimensions of atomic vapor cells are two orders of magnitude smaller, Rb-Rb collisions are negligible compared to collisions with the cell walls.

For a typical vapor cell (diameter 25 mm, length 50 mm) the average time between wall collisions is about 70 μs , whereas the excited state lifetime is 27 ns, so

the probability of an excited atom colliding with a cell wall is small. The mean kinetic energy for an atom at room temperature is $\langle E_k \rangle / h \approx 10^{13}$ Hz. This is small compared to the optical frequencies ($10^{14} \dots 10^{15}$ Hz) but large compared to the ground-state hyperfine splitting ($10^8 \dots 10^{10}$ Hz). When an atom collides with the cell wall it either sticks to it for some time, the average of which depends on the temperature, or bounces elastically from the surface. For a bare glass surface elastic collisions can be neglected and we can assume that complete relaxation takes place, meaning that the atom loses coherence and that it will populate all ground-state Zeeman sublevels (from both hyperfine states) with the same probability after the collision [32]. The rate of wall collisions is $\gamma = Av_{\text{ave}}/4V$, where A is the surface area of the cell, V is the volume of the cell and $v_{\text{ave}} = (8k_B T / \pi m)^{1/2}$ is the average velocity [32]. For a cylindrical cell this becomes

$$\gamma = \frac{1}{\sqrt{\pi}} \frac{R+L}{RL} v_{\text{mp}}, \quad (3.4)$$

where R is the cell radius and L is the cell length [32]. If the beam radius is smaller than the cell radius, one should replace the cell radius by the beam radius, as an atom exiting the beam inevitably collides with a wall before returning to the interaction region.

4

Optical pumping

Optical pumping refers to the redistribution of atomic level populations through absorption of light followed by spontaneous emission. It can be divided into depopulation pumping and repopulation pumping [31]. Depopulation pumping is due to selective excitation, e.g., the frequency of the light can be tuned to excite a certain hyperfine ground level or the polarization can be chosen to address particular Zeeman sublevels. Repopulation pumping arises from spontaneous decay of a polarized excited state. Different transition probabilities for decay to different ground levels lead to a partially polarized ground state. In multilevel atoms, many optical pumping processes are combinations of these two mechanisms. For alkali-metal atoms, optical pumping is usually divided into hyperfine and Zeeman optical pumping.

Note that some sources use the term polarization for any deviation from equally populated sublevels [31], whereas others use it only for states with a nonzero magnetic moment and use the term alignment for the case of unequally but symmetrically populated sublevels [32]. In the latter case, polarization is typically created by σ^+ (or σ^-) polarized light, i.e., circularly polarized light traveling in the direction of the quantization axis, whereas alignment is created by π or σ polarized light, i.e., linearly polarized light with the polarization vector parallel or orthogonal to the quantization axis, respectively.

Optical pumping is the topic of Publications I–II. Coherent population trapping (Publications III–IV) is a special form of optical pumping, where the atomic population is pumped into a nonabsorbing superposition state of the ground levels. Optical pumping is also responsible for the need of a repumping laser in the magneto-optical trap (Publication V).

4.1 Optical pumping in alkali-atom Doppler spectroscopy

When one measures the Doppler-broadened D_2 spectrum of an alkali-metal vapor, one notices that the amplitudes of the lines do not simply reflect the transition strengths and equilibrium ground-state populations even for intensities much lower than the two-level saturation intensity, $I \ll I_s$. In particular, the amplitude of the so-called A line (transitions from the lower hyperfine ground

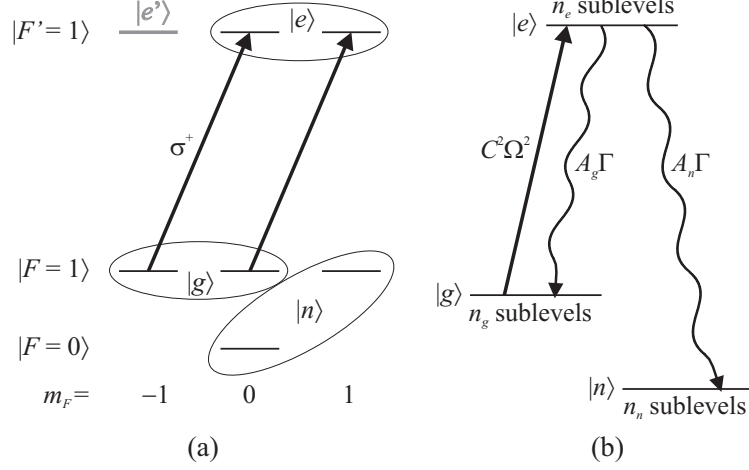


Figure 4.1. (a) σ^+ excitation of the $|F = 1\rangle \rightarrow |F' = 1\rangle$ transition in an atom with nuclear spin $I = 1/2$. The magnetic sublevels belonging to each effective energy level are circled. (b) The resulting three-level model.

level) compared to the amplitude of the B line (transitions from the upper level) is noticeably smaller than predicted. This is due to hyperfine optical pumping, which makes the relative contributions of the different hyperfine transitions vary with light intensity and polarization, beam size and vapor cell length. In addition to altering the amplitudes, optical pumping causes the center frequencies of the Doppler lines to shift, as the contributions from the different hyperfine transitions change.

Due to the hyperfine splitting and the magnetic sublevel structure of the alkali-metal atoms, the number of involved levels is impractically high for an analytical treatment. The number of levels can be reduced using the following assumptions: (i) The excited-state hyperfine splitting is much larger than the natural linewidth so that the laser field at moderate intensities ($I \lesssim I_s$) interacts with only one hyperfine excited state at a time. (ii) For a given excited state and polarization, we average over the allowed Zeeman transitions to reduce the number of levels to three. Fig. 4.1(a) illustrates this for σ^+ excitation of the $|F = 1\rangle \rightarrow |F' = 1\rangle$ transition in a (fictitious) atom with nuclear spin $I = 1/2$. The ground-state sublevels that are coupled by the light field form the ground state $|g\rangle$ and the corresponding excited-state sublevels form the excited state $|e\rangle$. The remaining ground-state sublevels, from both hyperfine levels, form the noncoupled state $|n\rangle$, to which atoms can be optically pumped. The uncoupled excited state $|e'\rangle$ can be neglected. C^2 is the Zeeman-averaged transition strength and Ω is the two-level Rabi frequency, both assumed to be real for simplicity. The excited state $|e\rangle$ decays to the ground states $|g\rangle$ and $|n\rangle$ at the rate Γ with the branching ratios A_g and A_n , respectively ($A_g + A_n = 1$). These branching ratios are averaged over the sublevels of $|e\rangle$.

The parameters C^2 , A_g and A_n , as well as the number of sublevels n_g , n_n and n_e , must be evaluated separately for different polarizations (π , σ , σ^+) and for each hyperfine excited state. With the assumptions described above, the values will

be the same for π and σ^+ light, even though the involved magnetic sublevels and transitions are different. The numerical values are tabulated in Appendix C of Publication II. At room temperature all magnetic ground-state sublevels are equally populated and the thermal equilibrium populations (in the absence of light) of the ground states are

$$P_i = \frac{n_i}{n_g + n_n}, \quad i = g, n. \quad (4.1)$$

4.2 Steady-state solution with ground-state relaxation

If we account for wall collisions using the relaxation rate γ given in Eq. (3.4), we can use the steady-state solution for the density matrix (Publication I). For the three-level system in Fig. 4.1(b), the evolution equations in the rotating frame and in the RWA are

$$\frac{d\rho_{ee}}{dt} = -C\Omega\tilde{\rho}_{ge}^i - \Gamma\rho_{ee}, \quad (4.2a)$$

$$\frac{d\rho_{gg}}{dt} = C\Omega\tilde{\rho}_{ge}^i + A_g\Gamma\rho_{ee} + \gamma(P_g\rho_{nn} - P_n\rho_{gg}), \quad (4.2b)$$

$$\frac{d\rho_{nn}}{dt} = A_n\Gamma\rho_{ee} + \gamma(P_n\rho_{gg} - P_g\rho_{nn}), \quad (4.2c)$$

$$\frac{d\tilde{\rho}_{ge}}{dt} = -\left[\frac{\Gamma}{2} + i\delta(v_z)\right]\tilde{\rho}_{ge} + i\frac{C\Omega}{2}(\rho_{ee} - \rho_{gg}). \quad (4.2d)$$

The steady-state solution is obtained by setting the time derivatives equal to zero and using the trace, $\text{Tr } \rho = 1$. The absorption is then governed by

$$\tilde{\rho}_{ge}^i(v_z) = -\frac{(\Gamma/2)(C\Omega/2)P_g}{\delta^2(v_z) + (\Gamma'/2)^2}, \quad (4.3)$$

where Γ' is the linewidth, broadened by saturation and optical pumping,

$$\Gamma' = \Gamma\sqrt{1 + \left(\frac{C\Omega}{\Gamma}\right)^2 \left(2P_g + P_n + \frac{\Gamma}{\gamma}A_n\right)}. \quad (4.4)$$

If $A_n \neq 0$, optical pumping is significant at intensities a factor of Γ/γ lower than saturation. For rubidium at room temperature and a beam radius of 10 mm this factor is as large as 3000.

The velocity average in Eq. (2.22) can be integrated numerically, calculated using fast Fourier transforms, or expressed using the complex error function [54] as is done in Publication I.

4.3 Interaction-time averaged optical pumping

The steady-state solution in Section 4.2 is convenient, but optical pumping is actually a transient effect and the density matrix should be averaged over the distri-

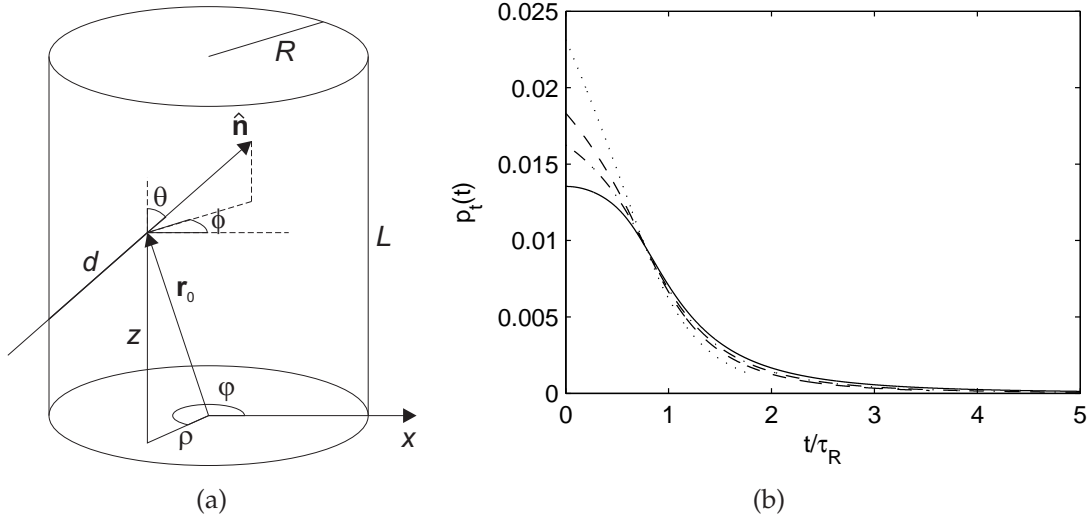


Figure 4.2. (a) Geometry of the interaction region. (b) Interaction time distributions $p_t(t|v_z)$ for the velocity groups $v_z = 0$ (solid), $v_z = v_{\text{mp}}$ (dashed) and $v_z = 2v_{\text{mp}}$ (dotted). The average over v_z is also shown (dash-dotted). $R = 10$ mm, $L = 50$ mm.

bution of interaction times between the atoms and the laser field (Publication II),

$$\langle \rho_{ij} \rangle_t(v_z) = \int_0^\infty \rho_{ij}(v_z, t) p_t(t|v_z) dt. \quad (4.5)$$

Only after this can the velocity average, Eq. (2.22), be evaluated.

4.3.1 Distribution of interaction times

When the atoms enter the interaction region determined by the laser beam and the vapor cell, the ground-state populations obey Eq. (4.1). If we neglect the decrease of the laser intensity over the length of the cell, we can assume that the internal state of the atoms inside the interaction region at any time depends only on how long they have interacted with the laser field. The distribution of interaction times can be derived from the geometry of the interaction region and the atomic velocity distribution.

We consider an atom at a position $\mathbf{r}_0 = (\rho \cos \varphi, \rho \sin \varphi, z)$ inside the interaction region, defined by the radius R of the laser beam and the length L of the glass cell, see Fig. 4.2(a). It is traveling in the direction $\hat{\mathbf{n}} = (\cos \phi \sin \theta, \sin \phi \sin \theta, \cos \theta)$ and has traveled the distance d inside the beam. Using the geometry, the distribution of atoms inside the interaction region, and the conditional velocity distribution, we can derive the distribution of interaction times for a fixed v_z (Publication II),

$$p_t(t|v_z) = \left[\frac{1}{\tau_{v_z}} \left\{ 1 - e^{-\frac{\tau_R^2}{t^2}} \left[I_0 \left(\frac{\tau_R^2}{t^2} \right) + 3I_1 \left(\frac{\tau_R^2}{t^2} \right) \right] \right\} + \frac{2}{t} e^{-\frac{\tau_R^2}{t^2}} I_1 \left(\frac{\tau_R^2}{t^2} \right) \right] \times \Theta(t < \tau_{v_z}). \quad (4.6)$$

Here I_n is the n th order modified Bessel function of the first kind and we have defined the characteristic transversal interaction time $\tau_R = \sqrt{2}R/v_{\text{mp}}$ and the velocity-dependent longitudinal interaction time $\tau_{v_z} = L/|v_z|$. $\Theta(T)$ is a truth function, equal to one when T is true and zero otherwise. Fig. 4.2(b) shows this distribution for different velocity groups. If L approaches infinity, only the last term in Eq. (4.6) remains: the time distribution is independent of longitudinal velocity and identical to the $v_z = 0$ distribution in Fig. 4.2(b). This is also the distribution obtained from a two-dimensional treatment. On the other hand, the smaller the ratio L/R , the more the distributions for the different velocity groups will differ.

A simpler distribution has been derived in Ref. [55] and used also in Refs. [56, 57]. However, it only considers the two transversal dimensions and holds for the total time-of-flight through the beam, not for the interaction time of all atoms inside the beam at a certain time.

4.3.2 Time-dependent absorption

In the time-dependent case, there will be no ground-state relaxation and the system can be treated as an open two-level system neglecting the non-coupled state $|n\rangle$. The density matrix equations are thus

$$\frac{d\rho_{ee}}{dt} = -C\Omega\tilde{\rho}_{ge}^i - \Gamma\rho_{ee}, \quad (4.7a)$$

$$\frac{d\rho_{gg}}{dt} = C\Omega\tilde{\rho}_{ge}^i + A_g\Gamma\rho_{ee}, \quad (4.7b)$$

$$\frac{d\tilde{\rho}_{ge}}{dt} = -\left[\frac{\Gamma}{2} + i\delta(v_z)\right]\tilde{\rho}_{ge} + i\frac{C\Omega}{2}(\rho_{ee} - \rho_{gg}). \quad (4.7c)$$

This equation system can be solved by numerical integration using the initial conditions $\rho_{gg} = P_g$, $\rho_{ee} = \tilde{\rho}_{ge} = 0$. Fig. 4.3 shows $-\tilde{\rho}_{ge}^i$ as a function of time for two values of the detuning. For low intensities, $\Omega \lesssim \Gamma$, the time dependence can be divided into three regions: a rapid growth at small t , none or a few heavily damped Rabi oscillations depending on the parameters, and then a slow decay at the optical pumping rate. The slow optical pumping, compared to the atomic lifetime, of several microseconds is in agreement with [58], where saturated absorption spectra were studied.

Obtaining the density matrix elements through numerical integration of Eqs. (4.7) and then evaluating the integrals (4.5) and (2.22) numerically makes the calculation of complete absorption spectra extremely time consuming and is not very convenient for comparison with experimental data. Another motivation for finding an approximate analytical solution for Eqs. (4.7) is that the numerical solution tends to become unstable as the detuning $|\delta|$ increases, unless the integration time step is decreased.

A first estimate for the optical pumping rate can be obtained by assuming that the optical coherence and the excited-state population follow the changes in the ground-state population due to optical pumping. This approximation neglects the

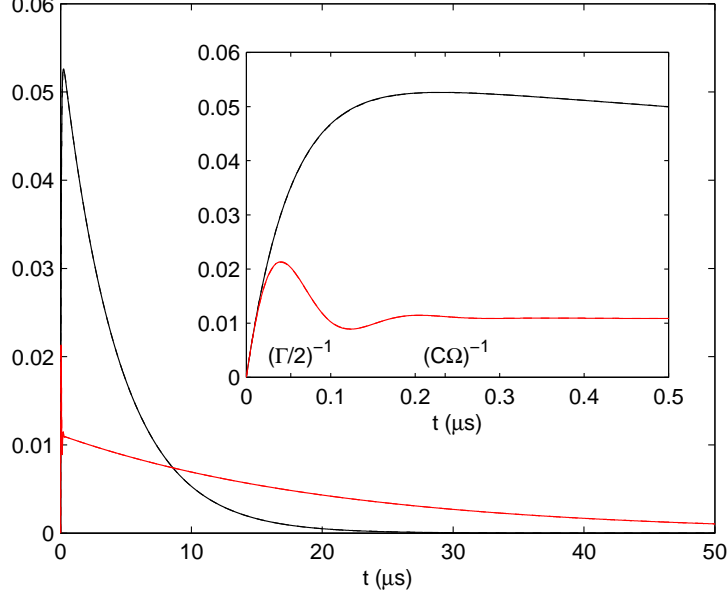


Figure 4.3. Numerically integrated absorption coefficient (actually $-\tilde{\rho}_{ge}^i$) as a function of time for $\delta = 0$ (black solid line) and $\delta = \Gamma$ (red solid line). The analytical approximations (black and red dashed lines, respectively) cannot be distinguished from the numerical curves. The inset shows the initial rise and Rabi oscillations for small t . The time scales $(\Gamma/2)^{-1}$ and $(C\Omega)^{-1}$ are shown. $I/I_s = 10^{-1}$. Figs. 4.3–4.6: $C = P_g = A_g = 0.5$, other parameters as for ^{85}Rb at $T = 300$ K.

initial rise and possible Rabi oscillations and is valid for $t \gg \Omega^{-1} \gtrsim \Gamma^{-1}$. It gives (Publication II)

$$\tilde{\rho}_{ge}^i(t) = -\frac{(\Gamma/2)(C\Omega/2)P_g}{\delta^2(v_z) + (\Gamma/2)^2 + (C\Omega/2)^2} e^{-\Gamma_{\text{op,est}} t}, \quad (4.8)$$

where the optical pumping rate is

$$\Gamma_{\text{op,est}} = \frac{(C\Omega/2)^2 A_n \Gamma}{\delta^2(v_z) + (\Gamma/2)^2 + (C\Omega/2)^2}. \quad (4.9)$$

We see that the expressions (4.8) and (4.9) lack the familiar factor of 2 in front of the saturation term in the denominator.

The full time-dependence can be solved using Laplace transforms as in Section 2.5. This leads to solving the roots of a fourth-order equation. The exact solutions are not very transparent, but Publication II shows how to use series expansions to obtain the approximative time dependence

$$\tilde{\rho}_{ge}^i(t) = \sum_{j=1}^3 B_j e^{s_j t} = B_1 e^{s_1 t} + 2 \text{Re}(B_2 e^{s_2 t}), \quad (4.10)$$

where

$$s_1 = -\frac{A_n \Gamma \left(\frac{C\Omega}{2}\right)^2}{\delta^2(v_z) + \left(\frac{\Gamma}{2}\right)^2 + \left[2 + \frac{\delta^2(v_z) - 3(\Gamma/2)^2}{\delta^2(v_z) + (\Gamma/2)^2} A_n\right] \left(\frac{C\Omega}{2}\right)^2}, \quad (4.11a)$$

$$s_{2,3} = -\frac{\Gamma}{2} \mp i\delta(v_z) - \frac{A_n \Gamma \pm 2i\delta(v_z)}{\delta^2(v_z) + \left(\frac{\Gamma}{2}\right)^2} \left(\frac{C\Omega}{2}\right)^2, \quad (4.11b)$$

and

$$B_1 = -\frac{\frac{\Gamma}{2} \frac{C\Omega}{2} P_g}{\delta^2(v_z) + \left(\frac{\Gamma}{2}\right)^2 + \left[2 + \frac{3\delta^2(v_z) - 5(\Gamma/2)^2}{\delta^2(v_z) + (\Gamma/2)^2} A_n\right] \left(\frac{C\Omega}{2}\right)^2}, \quad (4.12a)$$

$$B_{2,3} = \frac{\frac{1}{2} \left[\frac{\Gamma}{2} \mp i\delta(v_z)\right] \frac{C\Omega}{2} P_g}{\delta^2(v_z) + \left(\frac{\Gamma}{2}\right)^2 + \left[2 + \frac{3\delta^2(v_z) - 5(\Gamma/2)^2}{\delta^2(v_z) + (\Gamma/2)^2} A_n\right] \left(\frac{C\Omega}{2}\right)^2}. \quad (4.12b)$$

The optical pumping rate is $\Gamma_{\text{op}} = -s_1$. Writing the root s_1 and the amplitudes in this form, we can associate the terms $2(C\Omega/2)^2$ in the denominators with saturation, whereas the terms that are proportional A_n describes the effect of optical pumping. Fig. 4.3 shows that this solution hardly can be distinguished from the numerical solution.

4.3.3 Average over interaction-time and velocity distributions

With the time-dependence of Eqs. (4.10–4.12), the average over interaction times (4.5) cannot be evaluated in closed form. Hence we have to evaluate this integral as well as the integral over the velocity distribution numerically.

Homogeneous lineshapes for different atomic velocity groups are shown in Fig. 4.4. For a moderate intensity and large beam ($I/I_s = 10^{-1}$ and $R = 10$ mm), the lineshape, and in particular the amplitude, depend strongly on the longitudinal velocity, see Fig. 4.4(a). The interaction time of atoms with small $|v_z|$ is limited mainly by transversal motion, and they experience more optical pumping than atoms with larger $|v_z|$. Even after the lineshapes are scaled by the velocity distribution, there is a slight dip at zero velocity (right-hand figure). On the other hand, for a lower intensity and smaller beam size ($I/I_s = 10^{-3}$ and $R = 1$ mm), the lineshape is practically independent of v_z and no dip occurs, Fig. 4.4(b).

Fig. 4.5(a) compares the absorption coefficient, Eq. (2.25), obtained by numerically integrating the time-dependent absorption, Eq. (4.10), over t and v_z to the one calculated using the steady-state approach (Section 4.2) for different intensities. The dependence on the beam radius is similar, see Fig. 4.5(b). The behavior of the absorption coefficient can be described using the on-resonance optical pumping rate $\Gamma_{\text{op}}(\delta = 0) \approx A_n(C\Omega)^2/\Gamma$, the inverse of the transversal interaction time $\tau_R^{-1} = v_{\text{mp}}/\sqrt{2}R$, and the ratio of cell length to beam radius L/R . For

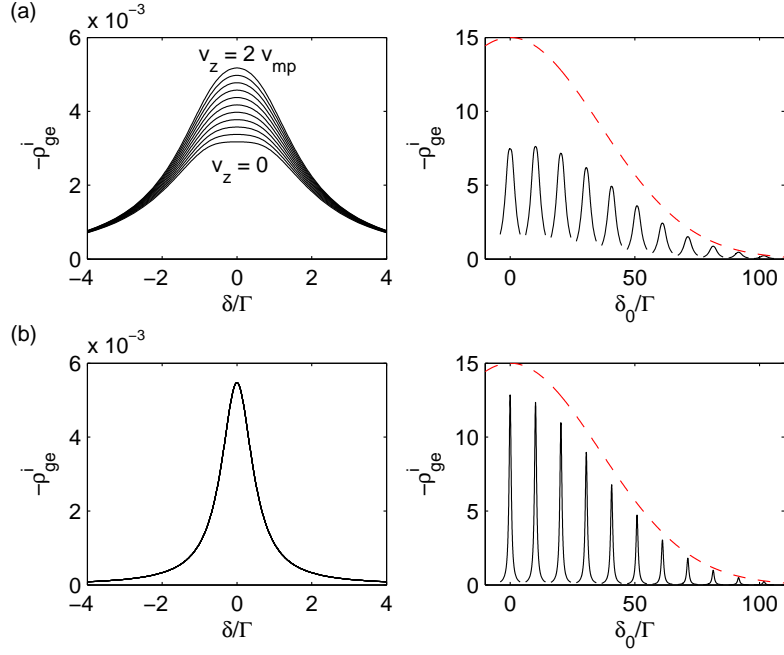


Figure 4.4. Homogeneous lineshapes ($-\tilde{\rho}_{ge}^i$) for the velocity groups $v_z/v_{mp} = 0, 0.2, \dots, 2$. The left figures show the lineshapes on top of each other, the figures on the right-hand side show the lineshapes at their Doppler-shifted positions and scaled by the velocity distribution, which is also shown (dashed curve, in arbitrary units). (a) $I/I_s = 10^{-1}$, $R = 10$ mm and (b) $I/I_s = 10^{-3}$, $R = 1$ mm. $L = 50$ mm.

$L/R \gg 1$ and $\Gamma_{op}(\delta = 0) \ll \tau_R^{-1}$, the absorption coefficient is practically identical to the result using the steady-state approach (see the highest curves in Figs. 4.5(a) and 4.5(b)). When $\Gamma_{op}(\delta = 0) \sim \tau_R^{-1}$, the difference between the amplitudes is maximum (middle curves in Fig. 4.5(a) and second lowest curves in Fig. 4.5(b)). Keeping the ratio of the two rates constant, the difference increases with intensity. Finally, when $\Gamma_{op}(\delta = 0) > \tau_R^{-1}$, the amplitudes are again close, but the curve obtained using the time-dependent approach is clearly not a Voigt profile, but has a flatter top or even a dip at the center (lowest curves in Figs. 4.5(a) and 4.5(b)).

Fig. 4.6 shows the absorption coefficients for different cell lengths. The curve obtained using the steady-state approach is always a Voigt profile and its amplitude increases when the length decreases (γ increases, which counter-acts optical pumping). In the time-dependent approach, on the other hand, atoms with a longitudinal velocity close to zero exit the interaction region mainly in the transversal direction. They are therefore almost unaffected by the cell length, whereas atoms with nonzero longitudinal velocity experience less optical pumping for shorter cell lengths. Again, this causes a dip in the Doppler profile as the cell length approaches the beam diameter.

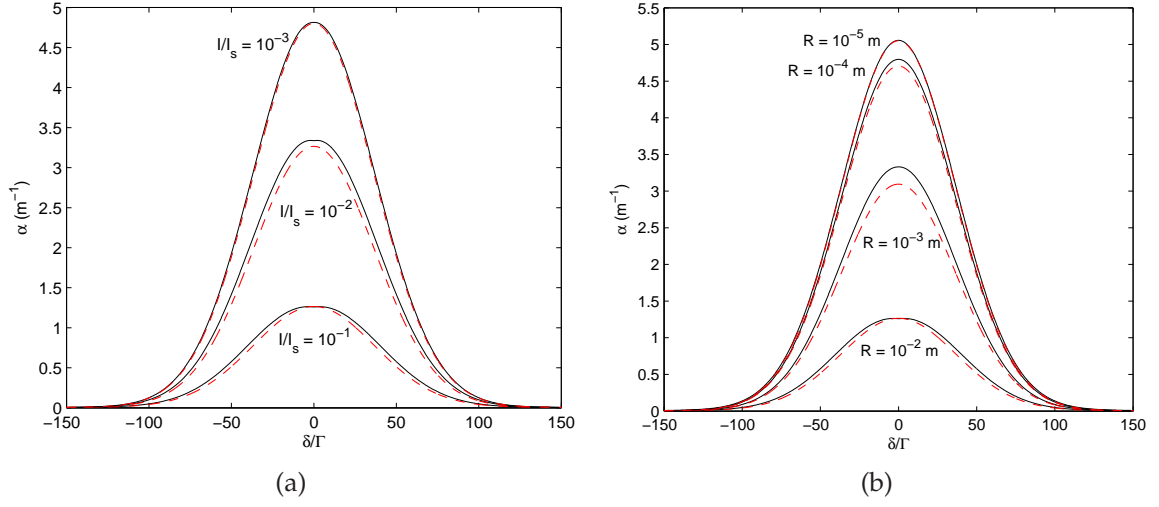


Figure 4.5. Absorption coefficients obtained from Eq. (4.10) (black solid curves) and using the steady-state approach (red dashed curves). (a) For different intensities ($R = 10$ mm). (b) For different beam radii ($I/I_s = 0.1$). $L = 50$ mm.

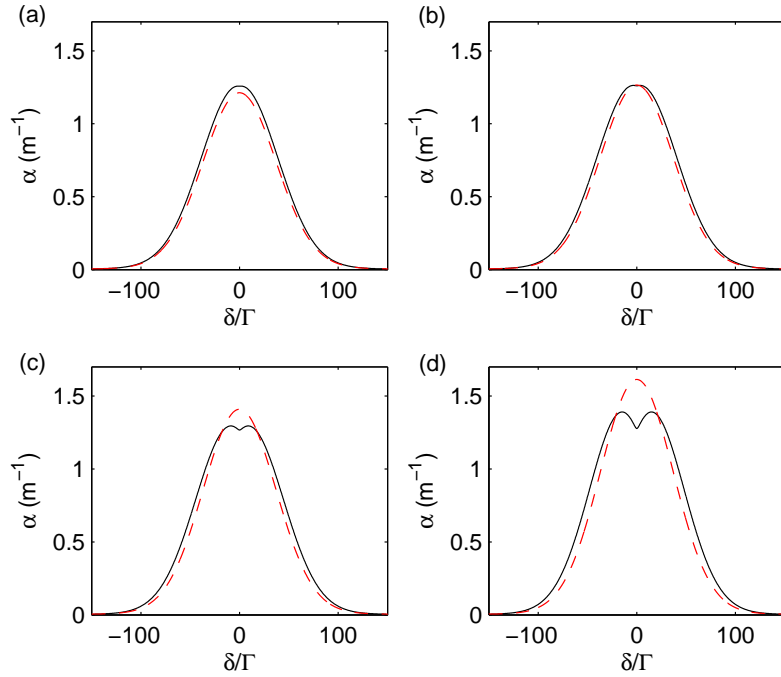


Figure 4.6. Absorption coefficients obtained from Eq. (4.10) (black solid curves) and using the steady-state approach (red dashed curves) for a) $L = 100$ mm, b) $L = 50$ mm, c) $L = 20$ mm, and d) $L = 10$ mm. $I/I_s = 0.1$, $R = 10$ mm.

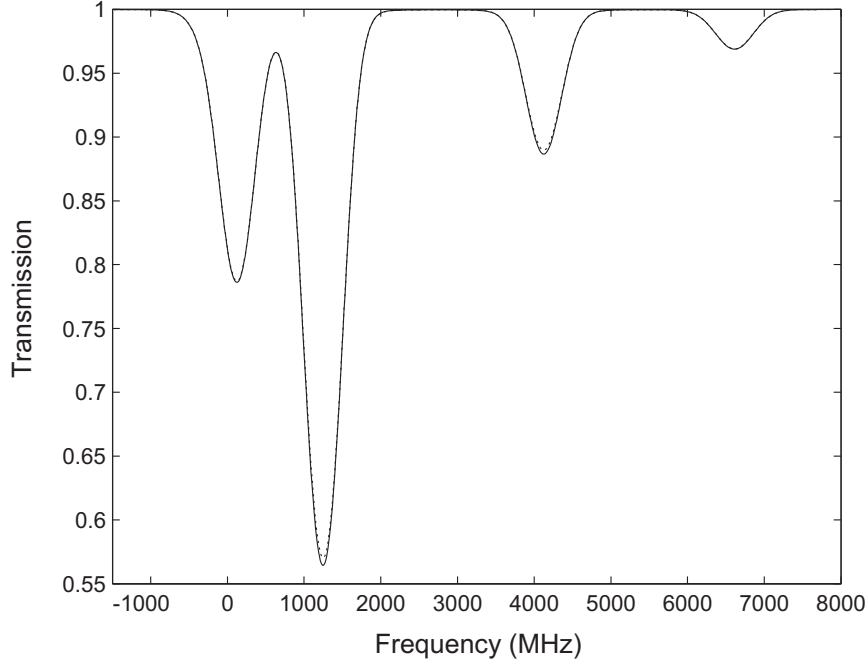


Figure 4.7. Rb D₂ absorption spectra for π or σ^+ polarization plotted using $M = 50$ (solid line) and $M = 1$ (dotted line). $T = 300$ K, $r = 15$ mm, $I/I_s = 10^{-1}$.

4.4 Rubidium D₂ spectra

D line spectra for the alkali-metal atoms can be obtained by summing over all transitions between the involved hyperfine levels. As an example, we consider the D₂ spectrum of natural rubidium.

4.4.1 Position-dependent absorption

Equation (2.26) cannot usually be solved analytically for an intensity-dependent absorption coefficient. It can be integrated numerically, or one can formally divide the absorbing medium of length L into M thin slices of thickness d , $L = Md$. If d is small enough, the absorption coefficient can be assumed constant over each slice and the intensity after the j th slice is given by

$$I_j = I_{j-1} e^{-\alpha(I_{j-1})d}, \quad j = 1, 2, \dots, M, \quad (4.13)$$

where I_0 is the incident and I_M is the transmitted intensity. Fig. 4.7 shows the rubidium D₂ spectrum for $M = 50$ and $M = 1$ using the steady-state approach (Section 4.2). One can see that the effect is small for an absorption length of 50 mm at room temperature, in agreement with recent theoretical results by Shin *et al.* [57]. As a large M makes the calculation of time-averaged spectra very time consuming, the spectra in Section 4.4.2 have been calculated using Eq. (2.27).

4.4.2 Transmission spectra

The dependence of the rubidium spectra on the parameters follow the behavior outlined for a single transition in Section 4.3.3, but the lineshape details are smeared out by the overlapping hyperfine transitions. Fig. 4.8 compares Rb D₂ spectra obtained by numerically integrating Eq. (4.10) to spectra obtained using the steady-state approach and by neglecting optical pumping but including saturation. In Fig. 4.8(a) the optical pumping is strong, but the lineshape details seen in Figs. 4.5(a)–4.5(b) are smeared out as each Doppler line consists of three overlapping transitions. In Fig. 4.8(b), $\Gamma_{\text{op}}(\delta = 0) \sim \tau_R^{-1}$ and the difference between the two approaches to treating optical pumping is largest. The two curves are still close compared to the spectrum neglecting optical pumping. Fig. 4.8(c) shows how the two results again approach each other as the optical pumping is reduced when the intensity and beam radius are decreased.

4.4.3 Doppler line shifts

The frequency shifts of the Doppler-spectrum minima as functions of different parameters can be obtained using the steady-state approach (Section 4.2). Fig. 4.9 shows the shifts as function of intensity and beam radius. Of particular interest is the different behavior of the A lines for π or σ^+ versus σ polarization.

4.5 Comparison to related research

The influence of optical pumping on the absolute absorption on the rubidium D lines has recently been experimentally studied by Siddons *et al.* [59]. They used a linearly polarized laser beam without nulling or controlling the laboratory magnetic field. In this case, the polarization experienced by the atoms depends on the local magnetic field, consisting of the field of the Earth and the fluctuating fields caused by electronic equipment. Fig. 4.10 shows rubidium D₂ spectra obtained using the time-dependent approach for parameters corresponding to Fig. 6 in [59] and for the following cases: π or σ^+ polarization, σ polarization, and randomly distributed quantization axis (equal amounts of π , σ^+ and σ^-)¹. The more polarization components that are involved, the fewer uncoupled magnetic sublevels there will be in the ground state and the less prominent the optical pumping will be. The experimentally obtained spectrum in Fig. 6 of [59] agrees well with our results for the following parameters: a polarization which consists of about 80 % σ and 20 % π , and a vapor pressure about 10 % higher than that from [51] and about 20 % lower than that from [53]. This seems reasonable given the uncertainties of the vapor pressure formulae, see Section 3.2.

¹In this case, the only difference between σ and random polarization occurs for the $|F = 1\rangle \rightarrow |F' = 0\rangle$ transition of the 87A line, where the ground sublevel $m_F = 0$ is uncoupled for σ , but coupled for random polarization.

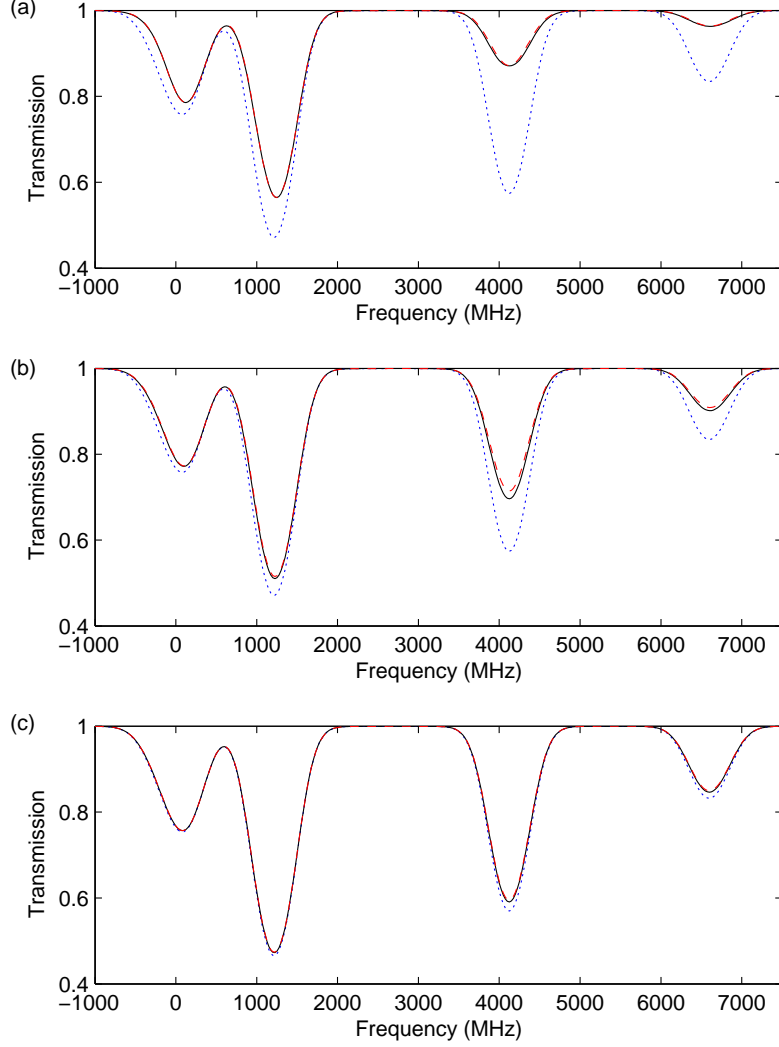


Figure 4.8. Rubidium D₂ spectra for π or σ^+ polarization obtained from (4.10) (black solid curves), using the steady-state approach (red dashed curves), and neglecting optical pumping, but including saturation (blue dotted curves). (a) $I/I_s = 0.1$, $R = 10$ mm, (b) $I/I_s = 0.1$, $R = 1$ mm, (c) $I/I_s = 0.01$, $R = 1$ mm. $L = 50$ mm, $T = 300$ K.

As pointed out in Publication I, Zeeman pumping can make the approach of averaging over the m_F sublevels fail for σ^+ polarization. Some recent results [56, 57] indeed indicate that this is the case. Shin *et al.* show that for σ^+ excitation of the cycling transition $|F = I + 1/2\rangle \rightarrow |F' = F + 1\rangle$, there is Zeeman pumping to the $m_F = F$ sublevel, which causes the absorption to increase with intensity before saturation sets in. On the other hand, Vanier has studied the effect of optical pumping on the rubidium D₁ spectrum in the presence of a buffer gas and observed good agreement between the three-level model and the experimental spectra for both σ and σ^+ polarization [60]. This is apparently due to the lack of cycling transitions in the D₁ line, but there might be an additional depolarizing effect by the buffer gas [31].

The method of averaging over the distribution of interaction times, Eq. (4.6),

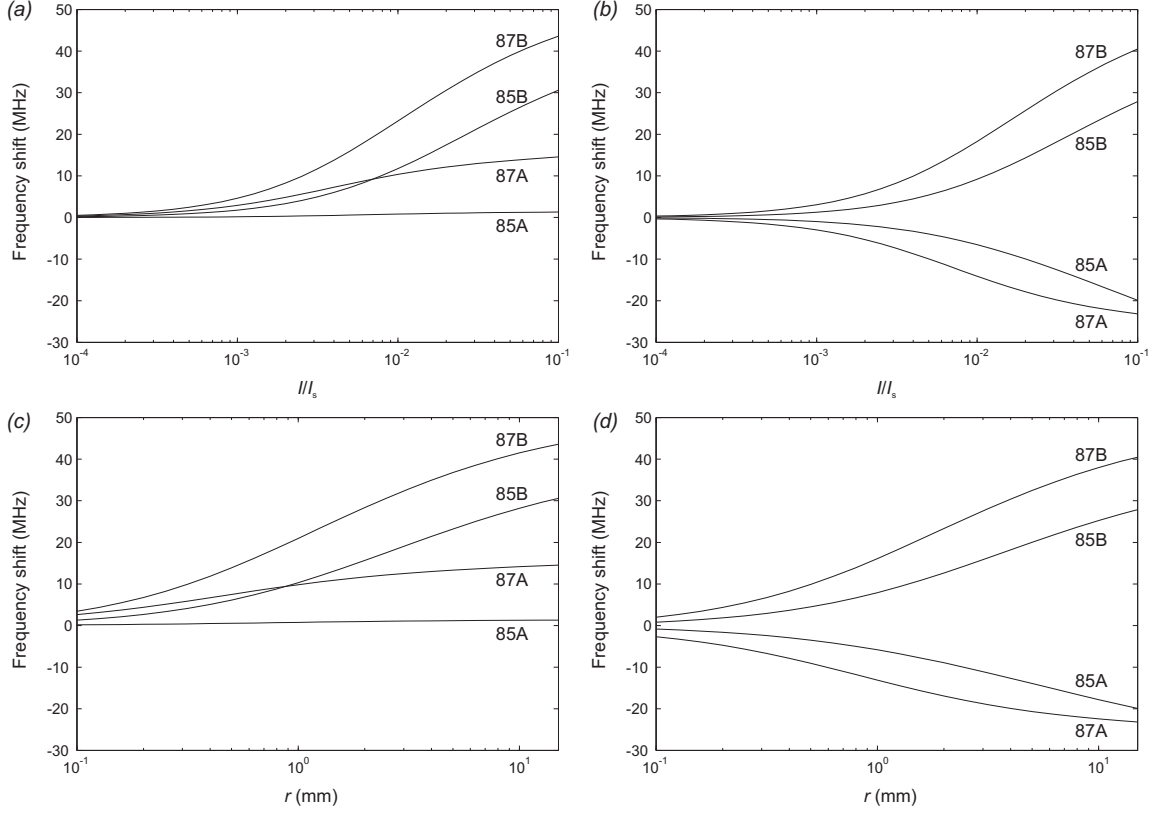


Figure 4.9. Frequency shifts of the peak minima of the Rb D₂ line as function of incident intensity and beam radius at $T = 300$ K. (a) π or σ^+ polarization and (b) σ polarization for $r = 15$ mm. (c) π or σ^+ polarization and (d) σ polarization for $I/I_s = 10^{-1}$. $M = 50$.

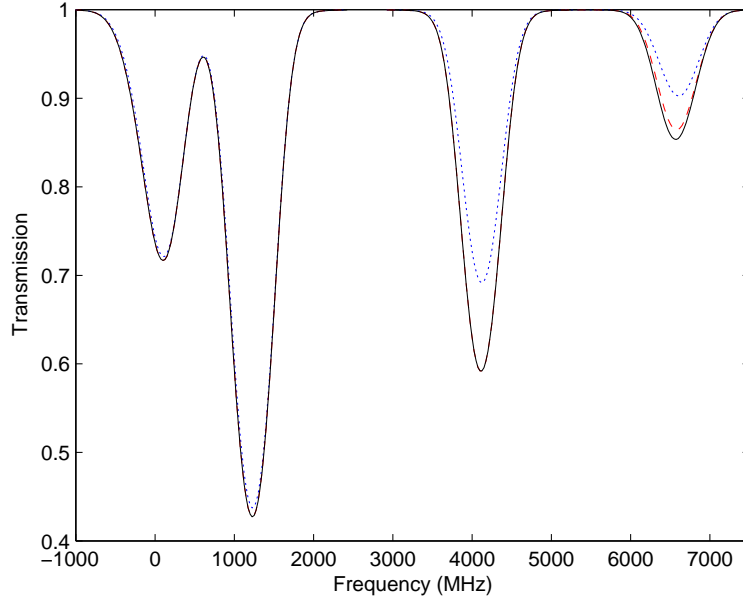


Figure 4.10. Rubidium D₂ spectra for π or σ^+ polarization (blue dotted curve), σ polarization (red dashed curve), and random quantization axis (black solid curve). $I/I_s = 10^{-1}$, $L = 75$ mm, $R = 2$ mm, $T = 298.55$ K.

can be used also when the full system including all excited-state hyperfine levels and magnetic sublevels is considered, although it would require considerable computational effort. This would take into account both Zeeman pumping and optical pumping that occurs via several close-lying excited levels simultaneously. The latter has been reported to cause asymmetry of the absorption profiles [58], as discussed in Publication I.

Coherent population trapping

The phenomenon of *coherent population trapping* (CPT) was first observed by Alzetta *et al.* in 1976 [35]. In this work the fluorescence of sodium atoms pumped by a multimode laser in an inhomogeneous magnetic field was studied. In combination with an excited level the two hyperfine ground levels of sodium form a three-level system in the so-called Λ configuration. A strong decrease in the fluorescence was observed at the positions in the sodium cell where laser modes were resonant with both of the Zeeman-shifted transitions of the Λ system. This gave rise to terms like *dark resonance* and *nonabsorption resonance*. Soon it was theoretically shown that the dark resonances occur because the atoms are pumped into a nonabsorbing superposition of the ground states [61, 62]. In 1979 Orriols reported on the exact steady-state solutions for the density matrix together with a numerical analysis [63]. The actual term coherent population trapping arose in the early 1980s [64].

In addition to frequency standards discussed here, CPT has several other applications. Velocity-selective coherent population trapping (VSCPT) is used in laser cooling [65] and CPT is utilized for lasing without inversion (LWI) [66, 67], electromagnetically induced transparency (EIT) [68], slowing down light [69], and in magnetometer applications [70–72]. An extensive review on CPT has been published by Arimondo [64] and a review on precision spectroscopy using CPT by Wynands and Nagel [73, 74].

5.1 Superposition states

The three-level Λ system used to describe CPT is similar to the one used to treat optical pumping, but there is now one laser field coupling each of the ground levels to the excited state, see Fig. 5.1(a),

$$\mathbf{E}_j(\mathbf{R}, t) = \frac{1}{2} \mathbf{u}_j \mathcal{E}_j e^{i(\omega_{Lj}t - k_j z + \phi_j)} + \text{c.c.}, \quad j = 1, 2. \quad (5.1)$$

In the electric dipole approximation and the RWA, the interaction Hamiltonian is then given by

$$V = -\frac{\hbar\Omega_1}{2} e^{-i(\omega_{L1}t - k_1 z + \phi_1)} |3\rangle\langle 1| - \frac{\hbar\Omega_2}{2} e^{-i(\omega_{L2}t - k_2 z + \phi_2)} |3\rangle\langle 2| + \text{H.c.}, \quad (5.2)$$

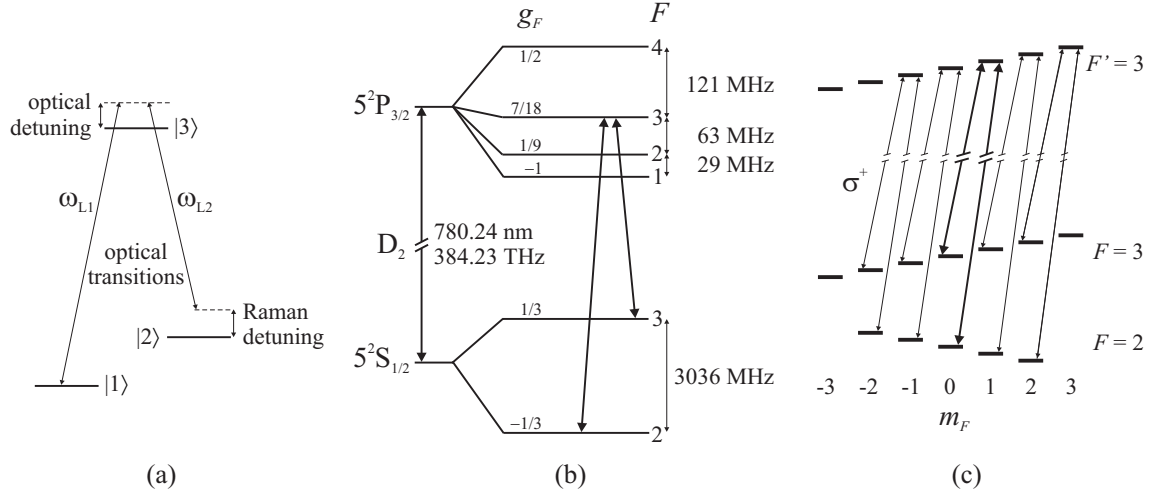


Figure 5.1. (a) Three-level Λ system. (b) ^{85}Rb Λ system used in the experiments. (c) Five open Λ systems are formed using σ^+ light and a homogeneous longitudinal magnetic field.

where H.c. stands for Hermitian conjugate and the Rabi frequencies are $\Omega_j = \mu_{j3} \cdot \mathbf{u}_j \mathcal{E}_j / \hbar$, again assumed to be real.

Let us define the following two orthogonal linear superpositions of the ground states, the coupled and the noncoupled states, which evolve in time as they are not energy eigenstates,

$$|C\rangle(t) = \frac{1}{\Omega} e^{i\omega_1 t} \left(\Omega_1 |1\rangle + e^{i[\omega_{21}t + \varphi(z)]} \Omega_2 |2\rangle \right), \quad (5.3a)$$

$$|NC\rangle(t) = \frac{1}{\Omega} e^{i\omega_1 t} \left(\Omega_2 |1\rangle - e^{i[\omega_{21}t + \varphi(z)]} \Omega_1 |2\rangle \right), \quad (5.3b)$$

where

$$\Omega = \sqrt{\Omega_1^2 + \Omega_2^2}. \quad (5.4)$$

The transition dipole matrix elements between the coupled and noncoupled states and the excited state are

$$\langle 3|V|C\rangle = -\frac{\hbar}{2\Omega} e^{-i(\delta_1 t - k_1 z + \phi_1)} \left(\Omega_1^2 + \Omega_2^2 e^{i[\delta_R t - \Delta k z + \Delta\phi + \varphi(z)]} \right), \quad (5.5a)$$

$$\langle 3|V|NC\rangle = -\frac{\hbar\Omega_1\Omega_2}{2\Omega} e^{-i(\delta_1 t - k_1 z + \phi_1)} \left(1 - e^{i[\delta_R t - \Delta k z + \Delta\phi + \varphi(z)]} \right), \quad (5.5b)$$

where the detunings from the optical resonances are $\delta_j = \omega_{Lj} - \omega_{3j}$ and the Raman detuning is $\delta_R = \delta_1 - \delta_2$. In addition, $\Delta k = k_1 - k_2$ and $\Delta\phi = \phi_1 - \phi_2$. We see that at two-photon resonance ($\delta_R = 0$) and for the phase condition $\varphi(z) = \Delta k z - \Delta\phi$, the matrix element for the noncoupled state is equal to zero. As both the coupled and noncoupled states are populated by spontaneous emission from the excited state, this causes a buildup of population in the noncoupled state.

5.2 CPT frequency standards

Since the nonabsorbing state in CPT is a superposition of two ground-state sub-levels, it is radiatively stable and the CPT resonance can be very narrow. The possibility of using this resonance as a frequency standard was soon realized. The first attempt to realize an all-optical—i.e., without a microwave cavity—frequency standard based on the hyperfine splitting of sodium was presented in 1982 by Thomas *et al.* [75]. In this experiment, two laser beams, each containing both modes of the Λ system, were incident on a sodium atomic beam at two separated interaction regions like in the Ramsey configuration, but without microwave cavities. In 1993 Cyr *et al.* proposed a simple all-optical microwave frequency standard with only one interaction region, based on CPT using a diode laser frequency modulated at a subharmonic of the ^{87}Rb hyperfine splitting [76]. A few years later serious efforts in this field were started by Vanier, Godone, and Levi [77] and Wynands *et al.* [73, 78–80].

Vanier *et al.* has worked with both a CPT maser [81] and a passive, optical CPT frequency standard [82]. Both of these approaches have been further developed and commercialized by Kernco Inc. [83, 84]. In collaboration with Wynands *et al.*, the Hollberg group from NIST (National Institute of Standards and Technology, CO, USA) started working on CPT frequency standards [85, 86]. The Hollberg group has concentrated on developing a micro-fabricated chip-scale CPT clock, where a vertical-cavity surface-emitting laser (VCSEL), the optics, the alkali cell, and the detector are integrated in a package of volume 1 cm^3 [87–89].

CPT based frequency standards have potential to be utilized in applications where an intermediate step between the Cs atomic clock and crystal oscillators is needed, such as in global navigation and telecommunications. A general review on CPT based atomic clocks has been published by Vanier [60] and a review on microfabricated atomic clocks by Knappe [90].

5.3 Buffer gas

The linewidth of the CPT resonance essentially depends on how long the atoms can interact coherently with the laser fields. For a cell with pure rubidium vapor at room temperature, the interaction time is limited by collisions with the cell walls, or by the radius of the laser beam if this is smaller than the cell radius. For typical cell sizes, the rate of collisions γ is of the order of 10^4 s^{-1} . One way to increase the interaction time is to use a coating, e.g., paraffine [91], on the inner cell walls. This makes the collisions soft and the relaxation rate can be decreased by as much as a factor of 1000 [32].

Another technique to increase the interaction time is to use an inert buffer gas, e.g., a noble gas or nitrogen. The alkali-metal atoms have to diffuse through the buffer gas which reduces the rate of wall collisions. The buffer gas also reduces any residual Doppler broadening, as the mean free path between collisions with

buffer-gas atoms is shorter than the CPT wavelength (Dicke narrowing [92]¹) [94].

However, the buffer gas collisions also shift and broaden the lines as the interaction shifts the energy levels of the atom. The optical D₂ transitions experience a red-shift of the order of a few MHz/mbar for Rb in the noble gases. The broadening is of the order of 10 MHz/mbar. This can be described as the collisions causing phase shifts in the radiation emitted or absorbed by the alkali-metal atoms. The net phase shift causes the pressure shift, whereas the dispersion of the shifts gives rise to the broadening.

When an alkali-metal atom collides with a buffer gas atom, the interaction Hamiltonian can be expressed as [32]

$$V_{AB} = U(r) + \delta A(r) \mathbf{S} \cdot \mathbf{I} + \gamma(r) \mathbf{S} \cdot \mathbf{N} + \delta(r) \mathbf{I} \cdot \mathbf{N}, \quad (5.6)$$

where it has been assumed that the buffer gas atom has no nuclear spin². The different terms will be explained in the following.

$U(r)$ represents the electrostatic and exchange interactions and can be approximated by a *Lennard-Jones* or *6–12 potential*

$$U(r) = \frac{C_{12}}{r^{12}} - \frac{C_6}{r^6}, \quad (5.7)$$

where the second, negative, term represents the attractive dipole-dipole or *van der Waals* interaction and the first, positive, term represents the repulsive interaction that appears when the atoms are close enough for the electronic clouds to overlap. This potential causes the scattering phenomenon and can also give rise to formation of van der Waals molecules. These molecules are formed by three-body collisions, i.e., a rubidium atom collides with two noble gas atoms and forms a molecule with one of them. The relaxation rate due to molecule formation is small for the lighter noble gases but for krypton and xenon it can be dominating [32].

$\delta A(r) \mathbf{S} \cdot \mathbf{I}$ is a shift in the hyperfine interaction $A \mathbf{S} \cdot \mathbf{I}$, where A is the hyperfine constant, due to a distortion of the orbital of the alkali S electron in the collision. First, the van der Waals forces pull the electron away from the nucleus, which decreases the hyperfine interaction. Then, at smaller distances, the exchange interaction increases the electronic density at the nucleus and the hyperfine interaction increases [32]. The net effect is a positive or negative pressure shift, depending on the particular atoms involved. As highly polarizable, the heavy noble gases Kr and Xe generally give rise to large van der Waals forces and thus a negative pressure shift, $\delta A < 0$, whereas the lighter ones He and Ne are not very polarizable and cause a positive shift, $\delta A > 0$ [31]. This effect does not cause transitions between the hyperfine states, but the dispersion of the shifts causes broadening.

¹Dicke narrowing occurs when the motion of the atoms is restricted to a region of space smaller than the wavelength of the radiation. The collisions between the optically active atoms and the buffer gas atoms must be elastic and the lifetime of the upper level has to be much longer than the mean time between collisions. Thus the effect occurs mainly in the infrared and microwave range, where both the wavelength and the lifetime are long [93].

²This is true for all noble-gas atoms, except for the following isotopes (natural abundance in parenthesis): ³He (0.00014 %), ²¹Ne (0.27 %), ⁸³Kr (11.5 %), ¹²⁹Xe (26.4 %), ¹³¹Xe (21.2 %) [95].

$\gamma(r)\mathbf{S} \cdot \mathbf{N}$ is the coupling between the alkali-metal atom spin \mathbf{S} and the angular momentum of the colliding atom pair,

$$\mathbf{N} = \frac{1}{\hbar} \mathbf{r} \times \mathbf{p}, \quad (5.8)$$

where \mathbf{r} and \mathbf{p} are the relative position and momentum of the two atoms. This term is believed to be the main cause of relaxation [32].

$\gamma(r)\mathbf{I} \cdot \mathbf{N}$ is the coupling between the alkali-metal atom nuclear spin \mathbf{I} and the angular momentum of the colliding pair. The ratio of this interaction to the $\gamma(r)\mathbf{S} \cdot \mathbf{N}$ interaction is of the order of the ratio between the electronic and nuclear mass, so for practical purposes it can be neglected.

As the buffer gas reduces broadening due to wall collisions, but causes an additional pressure broadening, there is a certain buffer gas pressure that gives a minimum linewidth.

The pressure and temperature dependence of the pressure shift is complicated, but the shift of the hyperfine splitting can in a limited temperature interval around a reference temperature T_0 be approximated by [32]

$$\delta\nu_{\text{hfs}} = p_0 \left[\beta_0 + \delta_0(T - T_0) + \gamma_0(T - T_0)^2 \right]. \quad (5.9)$$

Here p_0 is the buffer gas pressure at the reference temperature T_0 and β_0 , δ_0 and γ_0 are coefficients that can be measured. For a multi-component buffer gas, the contributions of the gases are simply added [91].

At higher alkali-metal atom densities (above room temperature for Rb), reabsorption of fluorescent light can destroy the ground-state coherence. In this case one can use nitrogen to quench the fluorescence [31]. In a quenching collision, the excitation energy of the alkali-metal atom is absorbed by the rotational and vibrational degrees of freedom of the diatomic nitrogen molecule.

5.4 Electron spin exchange

When two alkali-metal atoms come close to each other due to their thermal motion, they can exchange their electrons or spins [32]: as the electron clouds overlap it cannot be distinguished which electron belongs to which atom. This causes relaxation of both the ground-state populations and the ground-state coherence at the rates

$$\gamma_1^{\text{se}} = N v_{\text{r,ave}} \sigma_{\text{se}} \quad (5.10)$$

and

$$\gamma_2^{\text{se}} = \frac{6I + 1}{8I + 4} \gamma_1^{\text{se}}, \quad (5.11)$$

respectively [32]. Here N is the density of the alkali-metal atoms, $v_{\text{r,ave}}$ is the average relative velocity of the two atoms, and σ_{se} is the spin-exchange cross section.

The spin-exchange broadening sets a fundamental lower limit on the obtainable linewidth in alkali-metal vapor based frequency standards. Spin exchange

collisions also cause a frequency shift which is proportional to the alkali density and the population difference between the two clock levels. This is important in atomic clocks which rely on a population imbalance between the two levels, but negligible for CPT clocks as no population imbalance is created in this case [96].

5.5 Density matrix for CPT in a cell with buffer gas

For the interaction Hamiltonian in Eq. 5.2, the rapid time dependence of the density matrix equations can be eliminated using the following transformations:

$$\tilde{\rho}_{j3} = \rho_{j3} e^{-i(\omega_{Lj}t - k_j z + \phi_j)}, \quad j = 1, 2, \quad (5.12a)$$

$$\tilde{\rho}_{12} = \rho_{12} e^{-i[(\omega_{L1} - \omega_{L2})t - (k_1 - k_2)z + \phi_1 - \phi_2]}. \quad (5.12b)$$

For the case of a buffer gas, the density matrix equations become

$$\frac{d\rho_{33}}{dt} = -\Omega_1 \tilde{\rho}_{13}^i - \Omega_2 \tilde{\rho}_{23}^i - \Gamma \rho_{33}, \quad (5.13a)$$

$$\frac{d\rho_{11}}{dt} = \Omega_1 \tilde{\rho}_{13}^i + \frac{\Gamma}{2} \rho_{33} + \frac{\gamma_1}{2} (\rho_{22} - \rho_{11}), \quad (5.13b)$$

$$\frac{d\rho_{22}}{dt} = \Omega_2 \tilde{\rho}_{23}^i + \frac{\Gamma}{2} \rho_{33} + \frac{\gamma_1}{2} (\rho_{11} - \rho_{22}), \quad (5.13c)$$

$$\frac{d\tilde{\rho}_{13}}{dt} = -\left[\frac{\Gamma^*}{2} + i\delta_1\right] \tilde{\rho}_{13} + i\frac{\Omega_1}{2} (\rho_{33} - \rho_{11}) - i\frac{\Omega_2}{2} \tilde{\rho}_{12}, \quad (5.13d)$$

$$\frac{d\tilde{\rho}_{23}}{dt} = -\left[\frac{\Gamma^*}{2} + i\delta_2\right] \tilde{\rho}_{23} + i\frac{\Omega_2}{2} (\rho_{33} - \rho_{22}) - i\frac{\Omega_1}{2} \tilde{\rho}_{12}^*, \quad (5.13e)$$

$$\frac{d\tilde{\rho}_{12}}{dt} = -[\gamma_2 + i\delta_R] \tilde{\rho}_{12} + i\frac{\Omega_1}{2} \tilde{\rho}_{23}^* - i\frac{\Omega_2}{2} \tilde{\rho}_{13}. \quad (5.13f)$$

The excited state decays at the rate Γ , whereas the dephasing rate of the optical coherences includes contributions from radiative dampening and collisions with buffer gas atoms [97]: Γ^* is the collisionally broadened linewidth. The decay rates for the ground-state populations and coherences are γ_1 and γ_2 , respectively. For simplicity, it has been assumed that the spontaneous emission branching ratios and the equilibrium populations of the two ground states are equal.

For a typical frequency standard application, we can make the following assumptions in order to simplify the equations [91]:

- The laser field is weak, $\Omega_{1,2} \ll \Gamma, \Gamma^*$.
- The excited-state population is small compared to the ground-state populations, $\rho_{33} \ll \rho_{11,22}$, which implies $\rho_{11} + \rho_{22} \approx 1$.
- The Raman detunings considered are small compared to the optical linewidth, $\delta_R \ll \Gamma^*$.
- Adiabatic approximation: the optical coherences are assumed to evolve rapidly and we can use the steady-state expressions obtained by setting Eqs. (5.13d–5.13e) equal to zero.

By using these assumptions and defining the ground-state population difference $w_{21} = \rho_{22} - \rho_{11}$ and the average optical detuning $\delta_0 = (\delta_1 + \delta_2)/2$, Eqs. (5.13) are reduced to

$$\frac{d\rho_{33}}{dt} = -\Gamma\rho_{33} + \frac{1}{1 + (2\delta_0/\Gamma^*)^2} \left[\frac{\Omega_1^2 + \Omega_2^2}{2\Gamma^*} + \frac{\Omega_2^2 - \Omega_1^2}{2\Gamma^*} w_{21} + \frac{2\Omega_1\Omega_2}{\Gamma^*} \tilde{\rho}_{12}^r \right], \quad (5.14a)$$

$$\begin{aligned} \frac{dw_{21}}{dt} = & - \left[\gamma_1 + \frac{1}{2\Gamma^*} \frac{\Omega_1^2 + \Omega_2^2}{1 + (2\delta_0/\Gamma^*)^2} \right] w_{21} \\ & + \frac{1}{1 + (2\delta_0/\Gamma^*)^2} \left[\frac{\Omega_1^2 - \Omega_2^2}{2\Gamma^*} + \frac{\delta_0\Omega_1\Omega_2}{(\Gamma^*/2)^2} \tilde{\rho}_{12}^i \right], \end{aligned} \quad (5.14b)$$

$$\begin{aligned} \frac{d\tilde{\rho}_{12}}{dt} = & - \left[\gamma_2 + \frac{1}{2\Gamma^*} \frac{\Omega_1^2 + \Omega_2^2}{1 + (2\delta_0/\Gamma^*)^2} + i \left(\delta_R + \frac{\Omega_1^2 - \Omega_2^2}{1 + (2\delta_0/\Gamma^*)^2} \frac{\delta_0}{\Gamma^{*2}} \right) \right] \tilde{\rho}_{12} \\ & - \frac{1}{2\Gamma^*} \frac{\Omega_1\Omega_2}{1 + (2\delta_0/\Gamma^*)^2} - i \frac{\Omega_1\Omega_2}{1 + (2\delta_0/\Gamma^*)^2} \frac{\delta_0}{\Gamma^{*2}} w_{21}. \end{aligned} \quad (5.14c)$$

For the special case when $\delta_0 = 0$ and $\Omega_1 = \Omega_2 = \Omega$, Eqs. (5.14) simplify to

$$\frac{d\rho_{33}}{dt} = -\Gamma\rho_{33} + \frac{\Omega^2}{\Gamma^*} (1 + 2\tilde{\rho}_{12}^r), \quad (5.15a)$$

$$\frac{dw_{21}}{dt} = - \left(\gamma_1 + \frac{\Omega^2}{\Gamma^*} \right) w_{21}, \quad (5.15b)$$

$$\frac{d\tilde{\rho}_{12}}{dt} = - \left(\gamma_2 + \frac{\Omega^2}{\Gamma^*} + i\delta_R \right) \tilde{\rho}_{12} - \frac{\Omega^2}{2\Gamma^*}. \quad (5.15c)$$

We can define the pumping rate $\Gamma_p = \Omega^2/2\Gamma^*$, which creates a ground-state coherence without affecting the ground-state populations [91]. The steady-state solution of Eqs. (5.15) is

$$\rho_{33} = 2\frac{\Gamma_p}{\Gamma} \left[1 - 2\Gamma_p \frac{\gamma_2 + 2\Gamma_p}{\delta_R^2 + (\gamma_2 + 2\Gamma_p)^2} \right], \quad (5.16a)$$

$$w_{21} = 0, \quad (5.16b)$$

$$\tilde{\rho}_{12} = -\frac{\Gamma_p}{\gamma_2 + 2\Gamma_p + i\delta_R}, \quad (5.16c)$$

and the imaginary part of the optical coherences becomes

$$\tilde{\rho}_{j3}^i = -\frac{\Gamma_p}{\Omega} \left[1 - 2\Gamma_p \frac{\gamma_2 + 2\Gamma_p}{\delta_R^2 + (\gamma_2 + 2\Gamma_p)^2} \right], \quad j = 1, 2. \quad (5.17)$$

Eqs. (5.16–5.17) show that the full width at half maximum of the CPT resonance is $\Delta\omega_{\text{FWHM}} = 2(\gamma_2 + 2\Gamma_p)$. One can also see that the relaxation rate γ_2 determines the contrast of the CPT resonance: the absorption vanishes completely for $\gamma_2 = 0$ only.

One can also obtain the time-dependent solution of Eqs. (5.15). For the initial conditions $\rho_{33}(0) = w_{21}(0) = \tilde{\rho}_{12}(0) = 0$, we easily obtain $w_{21}(t) = 0$ and

$$\tilde{\rho}_{12}(t) = -\Gamma_p \frac{1 - e^{-(\gamma_2 + 2\Gamma_p + i\delta_R)t}}{\gamma_2 + 2\Gamma_p + i\delta_R}, \quad (5.18)$$

whereas $\rho_{33}(t)$ is more complicated. Note that for $\delta_R = 0$, the time constant of the coherence is directly related to the CPT linewidth.

In the general case ($\delta_0 \neq 0$ and $\Omega_1 \neq \Omega_2$), the algebraic solution of Eqs. (5.14) is complex. One important feature is the light shift term in Eq. (5.14c), which shifts the CPT resonance by

$$\Delta\omega_{\text{LS}} = -\frac{\Omega_1^2 - \Omega_2^2}{1 + (2\delta_0/\Gamma^*)^2} \frac{\delta_0}{\Gamma^{*2}}. \quad (5.19)$$

However, the theory leading to Eqs. (5.14) assumed that each field interacts with only one transition. Thus there will be a light shift due to the influence of each field on the other, nonresonant, transition even when the Rabi frequencies are equal. Assuming $\Omega_1 = \Omega_2 = \Omega$ and $\omega_{21} \gg \delta_R, \delta_0, \Gamma^*$, this shift is approximately $\Delta\omega'_{\text{LS}} = \Omega^2/2\omega_{21}$.

5.6 CPT frequency standard using ^{85}Rb

For the work of Publications III–IV, the D_2 line of ^{85}Rb , Fig. 5.1(b), was chosen, as laser diodes operating at 780 nm were readily available and because the modulation bandwidth of edge-emitting diode lasers covers the ground-state hyperfine splitting of 3.036 GHz. In frequency standards a Λ system involving the $m_F = 0$ ground levels, which experience no linear Zeeman shift, is preferred. The different Zeeman Λ systems are separated using a homogeneous longitudinal magnetic field and σ^+ light, see Fig. 5.1(c). The $|F' = 3\rangle$ excited state was chosen because the transition probabilities for transitions from the two ground states only differ by a factor of ~ 1.6 , whereas for the $|F' = 2\rangle$ excited state they differ by a factor of ~ 12 .

5.6.1 Experimental setup

The laser source was a 780-nm commercial edge-emitting diode laser equipped with an integrated microlens. The optical feedback from the closely mounted microlens ensures single-mode operation even under heavy current modulation and improves both the beam geometry and the frequency tunability.

Edge-emitting diode lasers have intrinsically low intensity noise, which is beneficial as the intensity noise at the detection frequency essentially determines the signal-to-noise ratio. Since the two CPT laser modes are generated from the same laser by frequency modulation, their frequency noise is nearly perfectly correlated and has a negligible effect on the decay rate of the ground-state coherence [64].

However, frequency noise can be converted to amplitude noise [98] and thus decrease the signal-to-noise ratio. In this case the frequency noise is determined by the properties of the laser diode, as the optical feedback from the microlens is too weak to narrow the linewidth. Fortunately the high output power of the laser diode (~ 20 mW) and the properties of its cavity yield a relatively small fundamental linewidth of approximately 2 MHz. The power of the first-order red sideband used as ω_{L2} was 30 % of the carrier power.

The laser frequency was locked to the cross-over resonance between the transitions $|F = 2\rangle \rightarrow |F' = 1\rangle$ and $|F = 2\rangle \rightarrow |F' = 2\rangle$ of the D₂ line using a laser frequency stabilization scheme similar to the one described in Ref. [99]. This resonance was used as it gives the strongest signal and partially compensates the -130 MHz pressure shift [100] caused by the buffer gas.

The experimental setup is schematically shown in Fig. 5.2. The clock part of the optical setup consists of a Rb cell, polarization and beam-expansion optics and a large-area, high-quantum yield (90 %) photodiode. The Rb cell is placed inside a long solenoid, which generates a homogeneous $6\text{-}\mu\text{T}$ field that lifts the Zeeman degeneracy. This is in turn enclosed by a magnetic shield. The laser beam is expanded to give a nearly uniform intensity over the cell cross section.

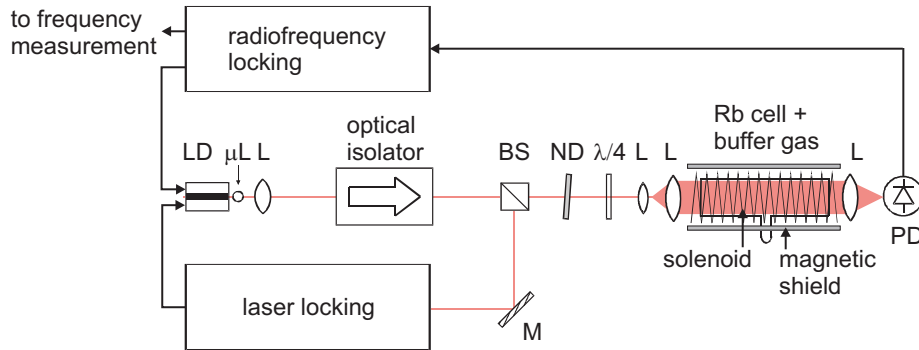


Figure 5.2. CPT clock setup: LD = laser diode, μL = microlens, L = lens, BS = beam splitter, ND = neutral density filter, $\lambda/4$ = quarter-wave plate, PD = photodetector, and M = mirror.

5.6.2 Neon-argon buffer gas

The first-order temperature dependence of the pressure shift, Eq. (5.9), can be reduced using a mixture of two buffer gases having temperature coefficients with opposite signs. Of the noble gases, He and Ne have positive temperature coefficients, whereas Ar, Kr and Xe have negative.³ He is not a practical choice because it easily diffuses through the cell walls and the heavy noble gases Kr and Xe cause additional broadening due to the formation of van der Waals molecules,

³Ref. [101] gives the values for ^{87}Rb , but it has been shown that the relative shift is the same for the two isotopes ^{85}Rb and ^{87}Rb [102].

see Sec. 5.3. For a Ne-Ar mixture the optimum pressure ratio $p_{\text{Ar}}/p_{\text{Ne}} \approx 0.87$ is obtained [101].

In a cylindrical Rb cell with a Ne-Ar two-component buffer gas the ground-state coherence decay rate is given by [32]

$$\gamma_2 = \left[\left(\frac{2.405}{r} \right)^2 + \left(\frac{\pi}{l} \right)^2 \right] p_0 \frac{D_{\text{Ne}} D_{\text{Ar}}}{D_{\text{Ne}} p_{\text{Ar}} + D_{\text{Ar}} p_{\text{Ne}}} + \frac{N_0}{p_0} (\bar{v}_{\text{Rb-Ne}} \sigma_2^{\text{Ne}} p_{\text{Ne}} + \bar{v}_{\text{Rb-Ar}} \sigma_2^{\text{Ar}} p_{\text{Ar}}) + \frac{6I+1}{8I+4} N_{\text{Rb}} \bar{v}_{\text{Rb-Rb}} \sigma_{\text{se}}, \quad (5.20)$$

where the three terms originate from wall collisions, pressure broadening, and spin-exchange collisions, respectively. A description of the symbols, their numerical values and references are given in Table 1 of Publication III.

Minimizing Eq. (5.20) using the pressure ratio $p_{\text{Ar}}/p_{\text{Ne}} \approx 0.87$ gives the optimal partial pressures $p_{\text{Ar}} \approx 16$ mbar and $p_{\text{Ne}} \approx 19$ mbar. These parameters give a calculated CPT linewidth of $\delta\nu = \gamma_2/\pi \approx 17$ Hz. The uncertainty is, however, large due to the uncertainties of the experimentally obtained decoherence cross sections and diffusion constants.

5.6.3 CPT resonances

The CPT resonances are very sensitive to saturation, as the coherence saturation intensity is much smaller than the saturation intensity for the optical transitions [64]. Brandt *et al.* [78] have measured the CPT linewidth in cesium as a function of intensity with a minimum linewidth of 42 Hz. Their results indicate a coherence saturation intensity of the order of $10 \mu\text{W}/\text{cm}^2$. Earlier a coherence saturation intensity of $70 \mu\text{W}/\text{cm}^2$ has been reported for ^{87}Rb [64]. In this work, saturation broadening was avoided by using very low light intensities, $\lesssim 1 \mu\text{W}/\text{cm}^2$, which was possible due to the good noise properties of the laser source and the expanded beam.

Frequency-modulation (FM) spectroscopy was used for frequency stabilization. Typical experimental parameters were: $1.3 \mu\text{W}/\text{cm}^2$ intensity, 325 Hz modulation frequency (between the 6th and the 7th harmonic of the line frequency in order to minimize interference), and a modulation index of 0.4. With these values it was possible to obtain a reasonable signal-to-noise ratio in detection and a sufficient feedback loop bandwidth. The lock-in amplifier output is shown in Fig. 5.3(a) as a function of the Raman detuning.

In order to measure as narrow CPT resonances as possible, a very low intensity of $0.3 \mu\text{W}/\text{cm}^2$ was used. Using wavelength modulation spectroscopy the resonances can be obtained directly through numerical integration of the lock-in amplifier output signal, see Fig. 5.3(b). Lorentzian lineshapes were fitted to estimate the FWHM of the resonances. The linewidth measured using a 19 Hz peak-to-peak modulation amplitude is 23 Hz, corresponding to a Q-value of 1.3×10^8 , comparable to Q-values in cesium atomic clocks [103]. The poor signal-to-noise ratio of the measurement with 10 Hz peak-to-peak modulation amplitude makes

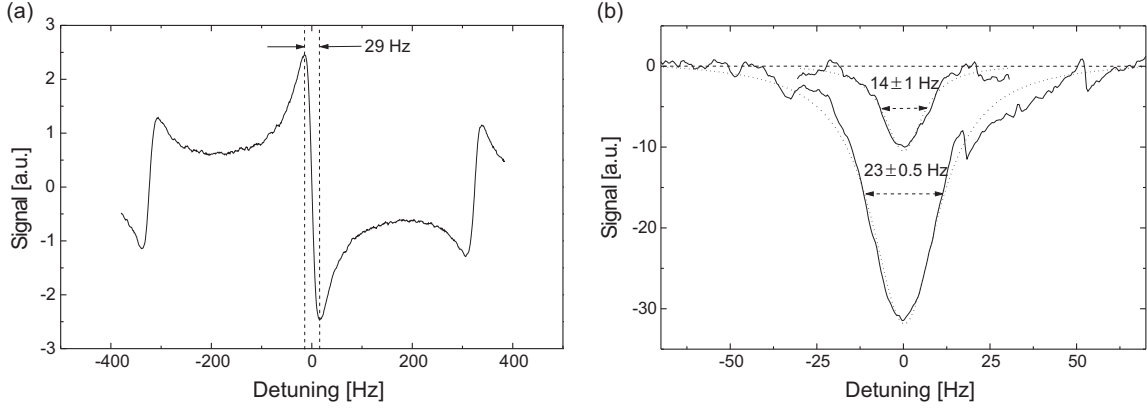


Figure 5.3. (a) FM spectroscopy signal of the CPT resonance. (b) CPT resonances of 23-Hz and 14-Hz widths measured using a 5-Hz lock-in frequency and peak-to-peak modulation amplitudes of 19 Hz and 10 Hz, respectively. The error estimates ± 0.5 Hz and ± 1 Hz refer to the uncertainty in fitting, the overall uncertainty being larger especially for the narrower line.

it difficult to determine the zero-level and thus to evaluate the linewidth. However, the linewidth is clearly below 20 Hz (Q-value 1.5×10^8), apparently the smallest optically-induced hyperfine CPT linewidth measured and in good agreement with the calculated linewidth of 17 Hz. The results of other authors include 42 Hz wide CPT resonances in cesium with neon buffer gas using a pair of phase-locked lasers [78] and 128 Hz wide CPT resonances measured in cesium with neon buffer gas using a single VCSEL, modulated to produce sidebands [80].

5.6.4 Frequency shifts

Light shift

The light shift of the CPT resonance was mentioned in Sec. 5.5. As the laser modes are obtained through frequency-modulation, the effect of all the sidebands have to be accounted for [104, 105]. The situation is further complicated by the fact that there are four hyperfine excited-state sublevels, two of which ($F' = 2$ and $F' = 3$) are coupled to both ground levels, thus contributing to the CPT. The $F' = 1$ ($F' = 4$) excited level is coupled only to the lower (upper) ground level. Because of the 400-MHz pressure broadening [100], all the excited levels are overlapping.

In Publication IV, the light shift was experimentally studied as a function of total intensity, laser mode intensity ratio, and optical detuning. With a 50-MHz detuning from the pressure-shifted $|F = 2\rangle \rightarrow |F' = 3\rangle$ resonance a linear intensity dependence of $0.3 \text{ Hz}(\mu\text{W}/\text{cm}^2)^{-1}$ was obtained. The dependence of the CPT frequency on the laser-mode intensity ratio is shown in Fig. 5.4(a) and the dependence on the detuning is shown in Fig. 5.4(b).

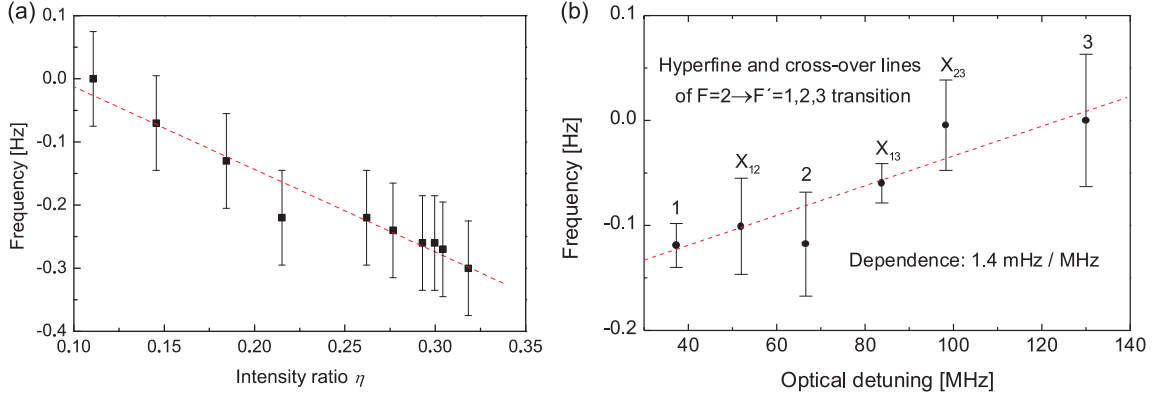


Figure 5.4. (a) Frequency shift of the CPT resonance as a function of the laser-mode intensity ratio. A linear fit gives a shift of $-1.3 \text{ Hz} \times \eta$. The total intensity was $2 \mu\text{W}/\text{cm}^2$ and the detuning was 50 MHz. (b) Frequency shift of the CPT resonance as a function of the laser detuning from the -130-MHz pressure-shifted $|F = 2\rangle \rightarrow |F' = 3\rangle$ transition. The intensity was $1.3 \mu\text{W}/\text{cm}^2$. A linear fit yields a $1.4 \text{ mHz}/\text{MHz}$ dependence on the laser detuning. These shifts are generally not linear and the linear fits are valid only in the small ranges studied here.

Pressure and temperature shifts

The pressure shift, described by the coefficient β_0 in Eq. (5.9), is by far the largest deviation from the unperturbed hfs frequency. The measured shift is 2.6 kHz , in reasonable agreement with the 2.3-kHz shift that can be calculated using the values from [102]. Even though the cells used in this experiment are produced in the same batch, the observed frequency difference is 40 Hz , which is within the limits of the $\pm 1\%$ pressure tolerance given by the manufacturer. The pressure shift makes this type of an atomic clock a secondary frequency standard, as it is necessary to characterize the frequency of each cell individually.

The Rb cell is thermally insulated but no active temperature stabilization is used in order to avoid stray magnetic fields from e.g. Peltier-element currents. Since the buffer gas mixture is optimized to minimize the temperature dependence, the residual temperature dependence is caused mainly by the uncertainties of the measured temperature shifts [101] and is expected to be small.

Magnetic field shift

The Zeeman-shifted energies of the alkali-atom ground-state sublevels can be calculated exactly using the Breit-Rabi formula [32]

$$E(F, m_F) = -\frac{E_{\text{hfs}}}{2(2I + 1)} - g_I \mu_B B_z m_F \pm \frac{1}{2} E_{\text{hfs}} \sqrt{1 + \frac{4m_F}{2I + 1} x + x^2} \quad (5.21)$$

for $F = I \pm 1/2$. Here

$$x = (g_J + g_I) \mu_B B_z / E_{\text{hfs}}, \quad (5.22)$$

where g_I is the nuclear g -factor, and E_{hfs} is the unperturbed hyperfine splitting energy. When $m_F = 0$, Eq. (5.21) is simplified and the 0-0 frequency for ^{85}Rb ($I = 5/2$) becomes

$$E_{0-0}(B_z) = E(3,0) - E(2,0) = E_{\text{hfs}} \sqrt{1 + x^2}. \quad (5.23)$$

This shift is plotted in Fig. 5.5(a) using the unperturbed hfs frequency $\nu_{\text{hfs}} = 3.035732440$ GHz and the experimentally obtained $g_I = 0.293640 \times 10^{-3}$ and $g_J = 2.002331$ [32]. The measured shift agrees very well with the calculated, except for an offset caused by the magnetic field of the Earth (the Rb cell was incidentally aligned in the north-south direction, allowing the field of the Earth to partially couple in through the optical windows). As the nonlinear Zeeman shift has a relatively strong effect on the CPT resonance frequency, all unnecessary magnetic fields in the cell should be carefully minimized.

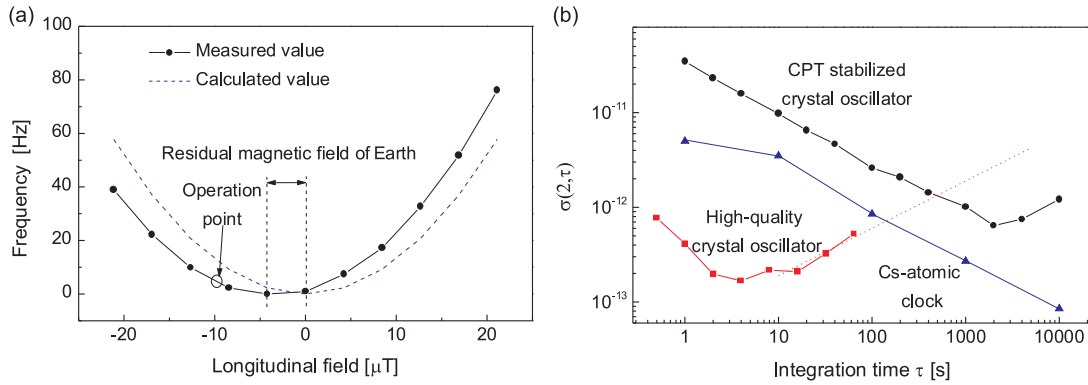


Figure 5.5. (a) Nonlinear Zeeman shift. (b) Relative frequency stability (square root of Allan-variance) of an RF signal generator locked to the 0-0 resonance (●). The stability of a high-quality crystal oscillator (■) [106] and a commercial Cs atomic clock (▲) are shown for reference.

5.6.5 Frequency stability

As no better frequency reference was available at the time, another setup, essentially identical except that the laser was stabilized using Zeeman locking [107], was constructed in order to measure the frequency stability by comparing the two setups. The relative frequency stability of an RF signal generator locked to the CPT resonance is shown in Fig. 5.5(b) as the square root of the Allan variance. The relative frequency stability of a free-running crystal oscillator and a commercial cesium atomic clock are given for reference. The relationship describing the relative frequency stability of the frequency synthesizer locked to the 0-0 CPT resonance is $3.5 \times 10^{-11} \tau^{-1/2}$ ($1 \text{ s} < t < 2000 \text{ s}$), and the best stability of 6.4×10^{-13} is reached at an integration time of $t = 2000 \text{ s}$.

The short-term stability was limited by the measurement technique used. Factors that are likely to limit the long-term stability include temperature fluctuations, despite the temperature-compensated buffer gas, and external magnetic fields.

6

Laser cooling

6.1 Light forces

The forces exerted on atoms by light can be derived using the semiclassical formalism of Chapter 2. Using the Heisenberg equation of motion for the time-independent Hamiltonian $H_{\text{tot}} = \mathbf{p}^2/2m + H_A + V(\mathbf{r})$ on the position and momentum operators gives

$$\frac{d\mathbf{r}}{dt} = \frac{i}{\hbar}[H_{\text{tot}}, \mathbf{r}] = \frac{\mathbf{p}}{m}, \quad (6.1a)$$

$$\frac{d\mathbf{p}}{dt} = \frac{i}{\hbar}[H_{\text{tot}}, \mathbf{p}] = -\nabla V(\mathbf{r}), \quad (6.1b)$$

respectively. From Eqs. (6.1) follows

$$m \frac{d^2\mathbf{r}}{dt^2} = \frac{d\mathbf{p}}{dt} = -\nabla V(\mathbf{r}) = \mathbf{F}(\mathbf{r}), \quad (6.2)$$

where \mathbf{F} is the force operator. Taking the averages (expectation values) in some time-independent Heisenberg state, one obtains

$$m \frac{d^2\langle\mathbf{r}\rangle}{dt^2} = \frac{d\langle\mathbf{p}\rangle}{dt} = -\langle\nabla V(\mathbf{r})\rangle = \langle\mathbf{F}(\mathbf{r})\rangle, \quad (6.3)$$

which holds in both the Heisenberg and the Schrödinger picture. The Ehrenfest theorem [108] states that if the position probability distribution is small compared to the length scale over which the force varies, we can replace the expectation value of the force operator by its value evaluated at the average position,

$$\langle\mathbf{F}(\mathbf{r})\rangle \approx \mathbf{F}(\langle\mathbf{r}\rangle). \quad (6.4)$$

When this is valid, the quantum-mechanical expectation values $\langle\mathbf{r}\rangle$ and $\langle\mathbf{p}\rangle$ obey the classical equation of motion. This is essentially the same assumption as the electric dipole interaction, Eq. (2.6), and also allows us to interchange the gradient with the expectation value, yielding the force

$$\mathbf{F}(\langle\mathbf{r}\rangle) \approx -\nabla\langle V(\mathbf{r})\rangle. \quad (6.5)$$

With $V(\mathbf{r})$ as in Eq. (2.10), but with position-dependent Rabi frequency $\Omega(\mathbf{r})$, and applying the RWA the expectation value becomes

$$\langle V(\mathbf{r}) \rangle = \text{Tr} [\rho V(\mathbf{r})] = -\frac{\hbar\Omega}{2}(\rho_{eg}e^{i(\omega t - kz)} + \rho_{ge}e^{-i(\omega t - kz)}). \quad (6.6)$$

The force is then given by

$$\begin{aligned} \mathbf{F} &= \hbar\tilde{\rho}_{ge}^r \nabla\Omega - \hbar\mathbf{k}\tilde{\rho}_{ge}^i \Omega \\ &= -\frac{2\hbar\delta}{\delta^2 + (\Gamma/2)^2 + 2(\Omega/2)^2} \nabla \left(\frac{\Omega}{2} \right)^2 + \hbar\mathbf{k}\Gamma \frac{(\Omega/2)^2}{\delta^2 + (\Gamma/2)^2 + 2(\Omega/2)^2}, \end{aligned} \quad (6.7)$$

where Eq. (2.15c) and the identity $(\Omega/2)\nabla\Omega = \nabla(\Omega/2)^2$ have been used.

The first term in Eq. (6.7) is the *dipole force* (also known as the *reactive*, *dispersive*, or *gradient force*). It is caused by the light shift of the atomic levels and is proportional to the gradient of the intensity ($I \propto \Omega^2$). Its sign is determined by the detuning; red detuning corresponds to an attractive force, blue detuning to a repulsive. For a plane wave the dipole force is zero, whereas a beam with a Gaussian intensity profile creates a force in the two transversal dimensions. A simple three-dimensional dipole trap can be created by a tightly focused red-detuned laser beam.

The second term in Eq. (6.7) is the *spontaneous force* (also known as the *dissipative*, *absorptive*, *scattering*, or *light pressure force*). It is due to the absorption of photons from the laser beam followed by spontaneous emission. The spontaneous emission is isotropic and there is thus a net momentum transfer in the direction of the wave vector. Note that the spontaneous force can be written as $\mathbf{F}_{\text{sp}} = \hbar\mathbf{k}\Gamma\rho_{ee}$, i.e., the photon momentum times the scattering rate $\Gamma_{\text{sc}} = \Gamma\rho_{ee}$.

Although the spontaneous force always points in the direction of the wave vector, its strength depends on the detuning, which for a moving atom depends on the velocity. This can be used to slow down atoms. For a red-detuned laser beam, atoms traveling opposite to the beam are shifted closer to resonance and absorb more photons, whereas those traveling in the direction of the beam are shifted away from resonance.

6.2 Magneto-optical trap

6.2.1 One-dimensional model

Consider an atom with the ground state $J_g = 0$ and excited state $J_e = 1$. In a linearly inhomogeneous magnetic field, $B(z) = bz$, the excited-state sublevels $m_e = -1, 0$, and $+1$ (excited by σ^- , π , and σ^+ polarization, respectively) experience a position-dependent Zeeman splitting as shown in Fig. 6.1. Incident on the atom are two red-detuned ($\delta < 0$) laser beams: a σ^+ polarized beam traveling in the positive z direction and a σ^- polarized beam traveling in the negative z direction.

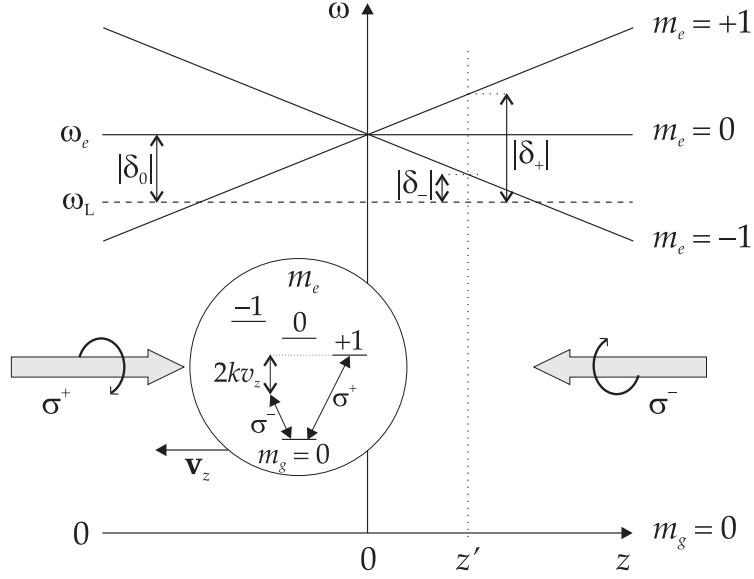


Figure 6.1. One-dimensional MOT. Due to the Zeeman shift, an atom at $z = z'$ is closer to resonance with the σ^- beam ($|\delta_-| < |\delta_+|$) and experiences a force towards the center. The circular inset illustrates how an atom traveling to the left is Doppler-shifted into resonance with the σ^+ beam and experiences a decelerating force.

As mentioned in Section 6.1, due to the Doppler shift an atom traveling in the negative direction will scatter more photons from the beam propagating in the positive direction, and vice versa. In addition, for an atom to the left of the origin, the position-dependent Zeeman shift tunes the σ^+ transition closer to resonance. The total force on the atom is $F = F_+ + F_-$, where the spontaneous forces exerted by the two beams are

$$F_{\pm} = \pm \hbar k \Gamma \frac{(\Omega/2)^2}{\delta_{\pm}^2 + (\Gamma/2)^2 + 2(\Omega/2)^2}, \quad (6.8)$$

where the detunings of the two beams are

$$\delta_{\pm} = \delta_0 \mp kv_z \mp g_e \mu_B bz / \hbar, \quad (6.9)$$

where g_e is the excited-state Landé factor. When the Doppler and Zeeman shifts are much smaller than the detuning, the total force can be expanded to be linear in v_z and z

$$F = -\beta v_z - \kappa z, \quad (6.10)$$

where the damping coefficient is given by

$$\beta = \frac{-\hbar k^2 \Gamma \delta_0 \Omega^2}{[\delta_0^2 + (\Gamma/2)^2 + 2(\Omega/2)^2]^2} \quad (6.11)$$

and the spring constant by

$$\kappa = \frac{g_e \mu_B b}{\hbar k} \beta. \quad (6.12)$$

The first term in Eq. 6.10, the Doppler cooling term, is a viscous damping force. This gave rise to the term optical molasses [39]. The theoretical limit for Doppler cooling, the Doppler temperature or Doppler limit $T_D = \hbar\Gamma/2k_B$, can be obtained by equating the cooling rate to the heating rate associated with the atomic recoil at absorption and emission and is typically of the order of $100 \mu\text{K}$ [47].

6.2.2 Three-dimensional MOT

A three-dimensional MOT can be realized using a quadrupole magnetic field, created by a pair of coils in the anti-Helmholtz configuration, and three pairs of counter-propagating beams, see Fig. 6.2. Although there is no simple theoretical model for the 3-D MOT, it is a robust trap: not very sensitive to small intensity imbalances between the counter-propagating beam or impure polarizations.

For magneto-optical trapping of alkali-metal atoms, the strong and cycling D_2 transition from the upper hfs ground level $|F_g = I + 1/2\rangle$ to the highest hfs level of the $P_{3/2}$ excited state $|F_e = F_g + 1\rangle$ is used. Although this transition is closed, there is a finite probability to excite atoms to the lower hfs excited levels, mainly $|F'_e = F_g\rangle$, that leads to a loss of atoms through optical pumping to the lower hfs ground level $|F'_g = I - 1/2\rangle$. To solve this problem, another laser, the *repumper*, is tuned to the $|F'_g\rangle \rightarrow |F'_e\rangle$ or $|F'_g\rangle \rightarrow |F'_g + 1\rangle$ transition to optically pump the atoms back.

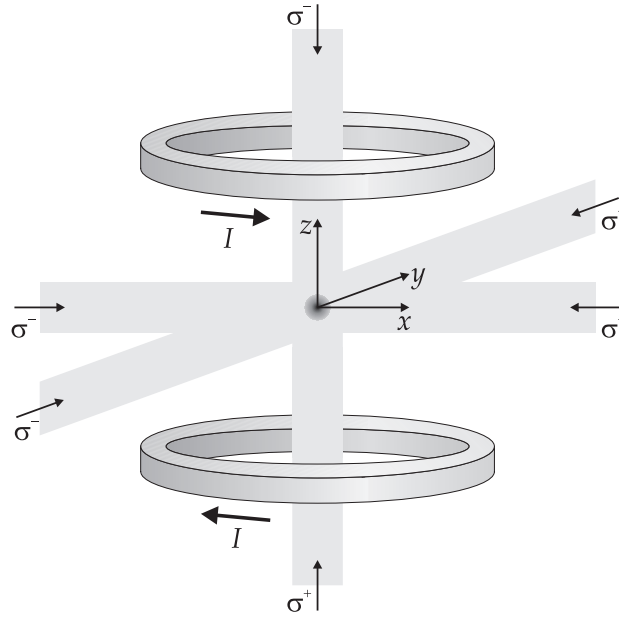


Figure 6.2. Three-dimensional MOT.

6.2.3 Polarization gradient cooling

A few years after the demonstration of optical molasses, temperatures much lower than the Doppler limit were measured [109]. This is due to polarization gradient

cooling (PGC) [110], a cooling effect that relies on optical pumping between the Zeeman sublevels of atoms as they move in the polarization gradient.

In the $\text{lin} \perp \text{lin}$ PGC configuration, where the two counterpropagating beams have perpendicular linear polarizations, the resulting polarization changes from linear at 45° , to σ^+ , to linear at -45° , to σ^- over half a wavelength. This causes the different Zeeman levels to experience different spatially-dependent light shifts. In addition, the polarizations are such that a moving atom is likely to always be optically pumped into the (locally) lowest Zeeman level. Hence it always “has to move uphill” and loses kinetic energy, a process referred to as Sisyphys cooling.

Another type of PGC is the $\sigma^+ \text{-} \sigma^-$ configuration. In this case, the resulting polarization is always linear, but rotates spatially like a cork screw with a period of one wavelength. A moving atom is unable to follow this polarization adiabatically. Using a $|J_g = 1\rangle \rightarrow |J_e = 2\rangle$ model, it has been shown that atoms traveling towards the σ^+ beam will have a larger population in the $m_g = +1$ state than in the $m_g = -1$ state, and vice versa for atoms traveling towards the σ^- beam [110]. This results in a damping force.

Polarization gradient cooling (also referred to simply as molasses cooling) is usually applied as a separate stage after the atoms have been trapped in the MOT, by turning off the magnetic field and increasing the detuning of the cooling laser, see for example Ref. [111].

6.2.4 MOT loading

The first MOT [40] was loaded from an atomic beam decelerated by a Zeeman slower [38], which is a fairly massive apparatus. The discovery that atoms could be trapped in a MOT directly from a low-pressure vapor in a small glass cell [112] was a great simplification and lead to a massive increase in the number of research groups working with laser cooling. In both cases, the source of atoms was a piece of alkali metal, either inside the oven that generated the atomic beam or in a separate part of the vacuum system, temperature-regulated in order to control the vapor pressure.

Hot background atoms limit the lifetime of the MOT. This problem has been solved by using a shutter to block the atomic beam after the MOT is loaded, or by transferring a vapor-loaded MOT into a lower-pressure part of the vacuum system through a differentially pumped line.

Today alkali-metal dispensers (AMDs) are the most commonly used source of atoms. An AMD is a small metal container containing an alkali-metal chromate and a reducing agent. When a dispenser in vacuum is heated above a threshold temperature of several hundred $^\circ\text{C}$ by running a current of several amperes through it, the reduction reaction starts and alkali-metal vapor is emitted through a slit in the container. Dispensers were first used in a simple and inexpensive vapor-cell MOT setup intended for student laboratories [113]. They were located relatively far from the trapping region and operated continuously to provide a sufficient background pressure.

Alkali-metal dispensers can also be used in pulsed mode [114]. In this case the dispensers are usually located a few centimeters from the MOT and the thermal atoms emitted from the dispenser are prevented from impacting the MOT center by a thin wire in front of the dispenser slit or, in the case of atom chips, see Section 6.4, by mounting the dispensers “behind” the edge of the chip. A large number of atoms (of the order of 10^8) can be loaded into the MOT using a current pulse of the order of 10 s and after five to ten more seconds the background pressure can be low enough to facilitate magnetic trapping [115–117]. However, this requires a good base pressure, large vacuum pumps, and careful design of the vacuum system, otherwise repetitive MOT loading will lead to an increased background pressure due to alkali-metal atoms that adsorb to the cell walls and are pumped away very slowly.

Another method to quickly modulate the alkali metal pressure for MOT loading is light-induced atom desorption (LIAD) [118]. In this method, there is a low alkali metal pressure in the vacuum chamber and a pulse of light is used to desorb atoms from its inner walls. Reported methods include desorption from stainless steel [118] and glass [119] using white light from a halogen bulb. Later ultraviolet light has been used [111]. In Ref. [111] it was also reported that desorption from quartz glass is not efficient enough, which was solved by adding a helix of Pyrex into the cell. Improved LIAD performance has also been reported using a pyrex cell coated with polydimethylsiloxane, a polymer with a very low adsorption coefficient [120].

6.3 Magnetic traps

In an inhomogeneous magnetic field \mathbf{B} , an atom with a magnetic moment μ experiences the force

$$\mathbf{F} = \nabla(\mu \cdot \mathbf{B}). \quad (6.13)$$

If the magnetic field is sufficiently strong, the magnetic moment will follow the changes in the field adiabatically, and the force simplifies to $\mathbf{F} = \mu \nabla B$. Local magnetic-field maxima are forbidden [121], but atoms in so-called low-field-seeking states, i.e., states with positive Zeeman shift, can be trapped in local minima. Magnetic traps are relatively shallow and are typically loaded with atoms from a MOT or optical molasses.

The quadrupole trap, consisting of two identical coils with opposite currents, like the quadrupole field in the MOT, is the simplest magnetic trap. The drawback with this trap type is that the magnetic field is zero at the center, which at lower temperatures leads to trap loss through Majorana spin-flip transitions.¹ The most commonly used trap type with non-zero magnetic field everywhere is the Ioffe or Ioffe-Pritchard trap. The basic design consists of four rectilinear currents that create a two-dimensional quadrupole field. Two circular end coils with the currents

¹Processes where an atom passes through a region of weak magnetic field where adiabatic following is not fulfilled and ends up in another magnetic sublevel when it re-enters a region of stronger field.

running in the same direction provide the axial confinement and the non-zero field in the center [47].

Magnetic traps can be realized also using permanent magnets. Of special interest is here traps based on magnetic thin films, where the trapping potential is obtained by adding an external magnetic field to the stray field from the domain pattern of the film. For a film with out-of-plane magnetization (preferred direction of magnetization normal to the surface), the stray field can be calculated using the equivalent current density [122]: a boundary where the magnetization reverses its direction corresponds to a current sheet with a total current $I = 2Mh$, where M is the magnetization and h is the thickness of the film. As an example, a quadrupole field can be created above the film surface by writing a circular domain of reversed magnetization into the film, corresponding to a circular current (“coil”), and superimposing an external field normal to the surface.

6.4 Atom chips

Microscopic magnetic traps based on planar current geometries were first suggested by Weinstein and Libbrecht in 1995 [123]. Miniaturization makes it possible to achieve large magnetic field gradients using relatively modest currents. The first experimental results were obtained using free-standing wire traps loaded from ordinary magneto-optical traps [124, 125]. The use of a so-called mirror MOT made it possible to collect the atoms in the near vicinity of an *atom chip*, a microfabricated wire structure on a planar substrate [126, 127]. This development eventually led to Bose-Einstein condensation in surface microtraps [116, 119].

Several problems associated with atom chips based on current-carrying wires have been reported. Fragmentation of the atomic clouds in the traps has been observed [128, 129]. This is due to deviations of the current path inside the wires that cause a varying longitudinal magnetic field component parallel to the wires [130]. These deviations have later been shown to be caused by local properties of the wire, such as inhomogeneous conductivity or top surface roughness, and not only the roughness of the wire edges [131]. Another problem is technical radio-frequency noise in the wires [128, 129]. Noise at the Larmor frequency of the atoms cause spin-flip transitions to untrapped Zeeman sublevels and noise at harmonics of the trap frequencies cause heating. A more fundamental problem is the trap loss at small distances that is caused by thermal current fluctuations (Johnson noise) in the conducting solid [132–135]. Also the issue of ohmic power dissipation must be addressed.

Atom chips based on permanent magnets offer several advantages. Ohmic heating and technical noise are lacking completely. Several different technologies have been investigated. Floppy discs have been used to create atom mirrors [136–138] and audio- and videotape has been used for atom mirrors [139], and to produce BEC in microtraps [140]. However, the tape has to be patterned outside the vacuum chamber and because of the in-plane magnetization, arbitrary two-dimensional patterns cannot be created. Other approaches include

an atom mirror created using an etched hard disc [141] and atoms traps, used for Bose-Einstein condensation, based on a hard disc with a periodic magnetization perpendicular to the plane [142].

Also permanent magnetic films have been used. One method is to have the film cover only part of the chip. This can be achieved by applying the film selectively [143] or by removing parts of the film by cutting or lithographic patterning [144, 145]. Both methods have been successfully used for Bose-Einstein condensation. Another possibility is to use magneto-optically patterned films. In this case the film is first magnetized in one direction perpendicular to the surface. By selectively heating spots above the Curie temperature while applying a weak external field in the opposite direction, the magnetization of the heated spot will flip. An early experiment with an atom mirror consisting of a periodically magnetized magneto-optical (M-O) TbFeCo film was successful, but the regions of un-flipped polarization contained striped domain patterns due to heat conduction [146]. Micrometer-scale M-O patterning of multilayer Co/Pt films designed for atom trapping has also been reported [147], but apparently not used for actual trapping.

A clear advantage of wire traps over permanent magnet traps is of course that the currents, and thus the fields, can be varied in time. With M-O films, an additional degree of freedom can be achieved if the film can be rewritten and erased inside the vacuum chamber, preferably during the experiment.

Regarding trap loss due to thermal currents, previously used M-O films have been metallic or have relied on a metal top layer to collect atoms in a mirror MOT, so the main advantage has been that the metallic layers have been thin compared to those used on wire chips. On the other hand, if we can use a dielectric magnetic film, the trap would be free of not only technical, but also thermal noise, as the dielectric does not affect the atoms significantly until the attractive Casimir-Polder potential [148, 149] limits the trap depth [135].

Atom chips loaded from a mirror MOT require a reflective metal top layer that, albeit thin, will cause some thermal noise. A transparent dielectric M-O film that could be loaded from a standard MOT, on the other hand, would be completely free from conducting layers.

Unfortunately, fragmentation of the atom cloud has been reported also for permanent magnet atom traps based on video tape [150], a hard disc platter [142], and the edge of a TbGdFeCo film [151]. For video tape, the corrugation of the potential is due to small, deep holes in the surface of the tape, probably formed during manufacture, and appears at a distance of 50 μm from the surface [150]. Also for the hard disc platter, the imperfections were attributed to manufacture and fragmentation occurred for distances below 40 μm [142]. For the TbGdFeCo film, the corrugation was due to long range inhomogeneity in the film magnetization and not the irregularity of the film edge [151]. The inhomogeneity was mainly caused during the vacuum bake-out and could be reduced by a factor of 10 by remagnetization, although the corrugation still remained larger than for microwires [131].

For M-O films, no results concerning corrugation of the potential has been

reported. The problem of deterioration of the magnetization during bakeout can be solved by magnetizing the film inside the chamber, but corrugation due to the finite size of the magnetic domains is to be expected.

6.5 Microscopic magneto-optical traps

The purpose of the microscopic MOTs reported in Publication [V](#) was to demonstrate the potential of transparent dielectric permanent-magnet films for atom chip applications.

6.5.1 Ferrite-garnet films

Magnetic garnets are ferrimagnetic insulators that are transparent over a broad spectral range [\[152\]](#). In Publication [V](#), a thin film of the bismuth-substituted ferrite garnet $(\text{BiYTmGd})_3(\text{FeGa})_5\text{O}_{12}$ is used. It is fabricated on a $500\text{ }\mu\text{m}$ $\text{Gd}_3\text{Ga}_5\text{O}_{12}$ (gadolinium-gallium-garnet, GGG) substrate using liquid phase epitaxy (LPE). The GGG substrate is transparent and paramagnetic. The ferrite garnet (FG) film is ferrimagnetic with the preferred direction of magnetization normal to the surface (out-of-plane magnetization). The minimum domain size is less than one micrometer [\[122\]](#).

The $1.8\text{-}\mu\text{m}$ thick FG film has a saturation magnetization of approximately 20 mT and a coercivity larger than 10 mT. A boundary where the magnetization \mathbf{M} reverses its direction can be modeled as carrying the equivalent current $I = 2Mh \approx 60\text{ mA}$, where h is the film thickness. The film can be patterned using a magnetic recording head or magneto-optically. Also all-optical switching of the local magnetization has been demonstrated [\[152\]](#).

The FG is transparent at near-infrared and infrared wavelengths (absorption $\sim 10\%$ at 780 nm) and exhibits large Faraday rotation of visible light, which makes it possible to image the domains using polarization spectroscopy. Details about the FG films can be found in [\[122\]](#).

6.5.2 Experimental setup

The vacuum system is shown in Fig. [6.3](#). It consists of a custom-made six-way cross with the glass cell, where the actual experiments take place, attached to the bottom and a large viewport on top. The other ports are occupied by the ion pump, the titanium sublimation pump (TSP), the ionization gauge for measuring the pressure, and the all-metal valve, which closes off the turbomolecular pump, backed by a membrane pump, and the nitrogen valve used to vent the chamber before it is opened.

After the initial pump-down, the vacuum chamber is covered with heating tapes and insulated with aluminum foil. The voltages of the heating tapes are slowly ramped up until the temperature of the glass cell is just below $200\text{ }^\circ\text{C}$ and the other parts around $210\text{ }^\circ\text{C}$. Then the chamber is baked for a few days

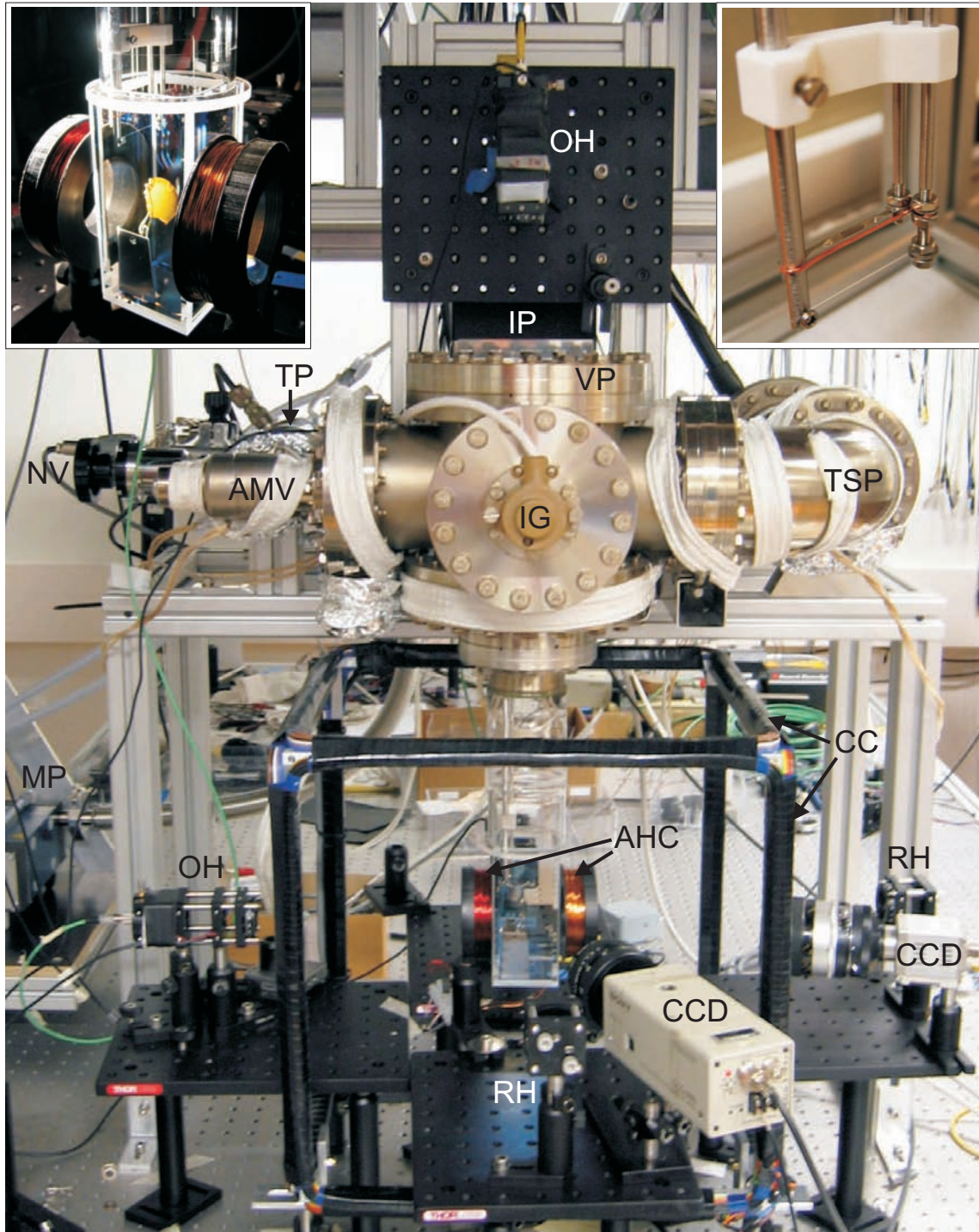


Figure 6.3. Vacuum system: VP—viewport, IP—ion pump, TSP—titanium sublimation pump, IG—ionization gauge, AMV—all-metal valve, TP—turbomolecular pump, MP—membrane pump, and NV—nitrogen valve. Coils: AHC—anti-Helmholtz coils and CC—compensation coils. Optics: OH—optics head, RH—retro-reflection head, and CCD—CCD camera. The inset on the left shows the FG film inside the cell, the one on the right the dispenser assembly.

with the turbopump running. During the bakeout all filaments (dispenser, ionization gauge, and TSP) are degassed thoroughly. Then the ion pump is started, the all-metal valve is closed and the temperature of the chamber is slowly ramped down. Once room temperature is reached, the pressure has dropped to about 5×10^{-10} mbar and after using the TSP it drops below the minimum pressure 1×10^{-11} mbar of the ionization gauge. Fig. 6.4 illustrates the vast range of atomic densities encountered in atom cooling and trapping.

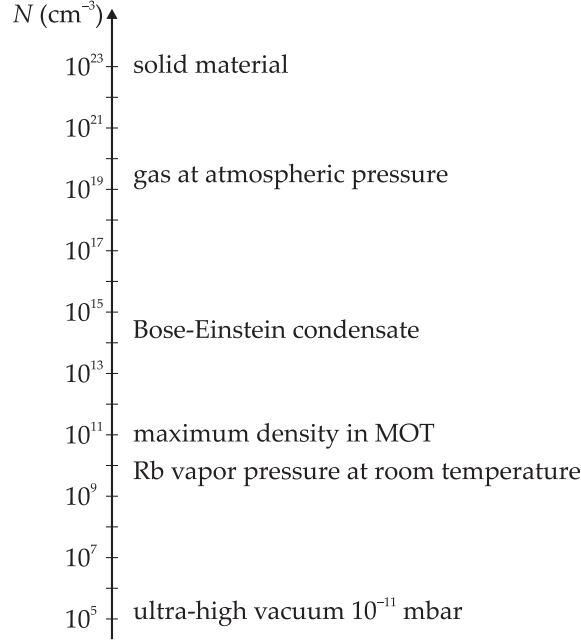


Figure 6.4. Atomic densities in atom cooling and trapping.

The lasers are located on another optical table. The cooling light is produced by three single-mode diode lasers injection-locked to a transmission-grating external-cavity diode laser [153], locked one natural linewidth below the $|F = 3\rangle \rightarrow |F = 4\rangle$ transition of ^{85}Rb . The three beams are coupled into polarization-maintaining single-mode optical fibers and delivered to three compact optics heads, containing beam expansion optics, quarter-wave plates and photo diodes to monitor the beam intensities, see Fig. 6.3. The three beams are retro-reflected by similar heads. The repumping light is created by a separate laser locked to the $|F = 2\rangle \rightarrow |F = 2\rangle$ transition and coupled into one of the optical fibers. The anti-Helmholtz coils for the MOT are mounted close to the glass cell, and the larger compensation coils, used to null the background field, are square-shaped in a cubical configuration in order to enable optical and physical access to the cell. Two CCD cameras are used to image the trapped atoms parallel and perpendicular to the surface of the FG film.

A scanning mirror is used to magneto-optically pattern the FG film inside the chamber and a polarization-microscopy (PM) setup is used to image the magnetic domain patterns using the CCD camera that is aligned perpendicular to the film. The scanning mirror and PM setup are not shown in Fig. 6.3.

The MOTs were loaded from rubidium vapor produced by a Rb dispenser above and slightly behind (on the substrate side) the FG film, see the insets in Fig. 6.3. During the experiments, it was heated continuously with a relatively low current.

6.5.3 Results

Atoms were trapped in a number of different micro-MOTs as well as in arrays of micro-MOTs. Because of the small spatial extent of the quadrupole field created by the magnetized pattern, the capture volume of the micro-MOTs is small and only around 7×10^4 atoms could be trapped. By adding a weaker but more extended quadrupole field using the anti-Helmholtz coils, the capture volume was increased and the number of trapped atoms exceeded 10^6 .

When the auxiliary quadrupole field was not used, atoms could be trapped in micro-MOTs 3 mm apart, as far as the size of the MOT beams allowed. More closely adjacent multiple micro-MOTs could be loaded with the auxiliary quadrupole field centered at the MOT array. Using purely optical patterning [152], patterns of reversed magnetization could be added to increase the number of micro-MOTs in the array.

The magneto-optical trapping is quite insensitive to the exact geometry (circular, square-shaped etc.) of the magnetized pattern. We were also able to trap atoms in a ring-shaped trap above a toroidal pattern, Fig. 6.5(a–c). By modulating the x and y components of the external field created by the compensation coils, the trap could instead be translated around the toroid, Fig. 6.5(d–g).

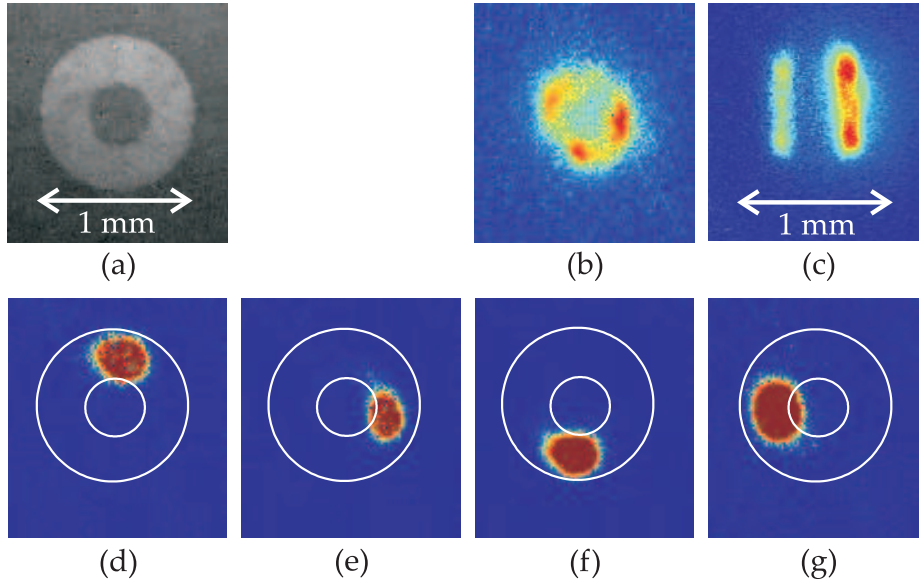


Figure 6.5. (a) Toroidal magnetization pattern. (b) Front view of the trapped atoms. (c) Side view of the trapped atoms. The left-hand image is the reflection from the chip surface and can be used to determine the distance of the atoms from the surface. (d–g) A MOT is translated around the toroid.

7

Conclusions

In this thesis, different aspects and applications of alkali atoms, in particular rubidium, in atomic and optical physics have been studied.

In Publication [I](#), the significant influence of optical pumping on the Doppler-broadened D-line spectra of alkali-metal vapors is shown. The atomic system with numerous sublevels is reduced to an effective three-level system, and an analytical expression for the absorption of the atoms is derived by taking into account the finite interaction time and collisions with the vapor-cell walls in the form of ground-state relaxation. The result gives physical insight on the significance of optical pumping compared to saturation, and constitutes a computationally efficient way to compare theoretical spectra to experimental results.

Publication [II](#) deals with the same topic as Publication [I](#), but considers the dynamics of the optical pumping process. A distribution for the interaction times of all atoms momentarily interacting with the laser field is derived from the three-dimensional geometry and the atomic velocity distribution. The time-dependence of the atoms entering the laser beam is solved numerically and an analytical series approximation is obtained. The time-dependent absorption is then averaged over the interaction-time and velocity distributions to obtain absorption spectra. The coupling between the Doppler shift and the interaction times through the longitudinal velocity of the atoms gives rise to velocity-dependent homogeneous lines and dips in the Doppler-broadened spectra. The interaction-time-averaged approach can be directly applied to the complete system including excited-state hyperfine sublevels and Zeeman sublevels with more numerical effort only.

In Publications [III–IV](#), an all-optical atomic clock is realized using coherent population trapping in rubidium. A buffer-gas mixture was optimized for narrow CPT resonances with reduced temperature dependence, and the theoretical predictions were later verified by an experiment where ultranarrow CPT resonances below 20 Hz were measured, apparently the narrowest optically induced hyperfine CPT resonance ever measured. The narrow linewidth was made possible by the good noise properties of the diode laser and by using a very low light intensity. The Q value of this resonance, 1.5×10^8 , is comparable to Q values in cesium clocks and the stability of the CPT clock is sufficient for many high-precision applications.

Publication [V](#) demonstrates trapping of Rb atoms in microscopic magneto-optical traps a few hundred micrometers from the surface of an optically trans-

parent permanent-magnet atom chip. The required magnetic fields are created by magnetic patterns magneto-optically written into the ferrite-garnet film. The transparent chip allows the use of a conventional MOT geometry, as one of the beams pass through the chip. The magnetic patterns can be erased and re-written *in situ* even during the experiments. Magnetic traps with a trap depth up to 1 mK could be realized using this type of atom chip.

References

- [1] H. Davy, "The Bakerian Lecture: On Some New Phenomena of Chemical Changes Produced by Electricity, Particularly the Decomposition of the Fixed Alkalies, and the Exhibition of the New Substances Which Constitute Their Bases; And on the General Nature of Alkaline Bodies", *Phil. Trans. R. Soc. Lond.* **98**, 1 (1808).
- [2] W. T. Brande, *A Manual of Chemistry* (George Long, New York, 1821).
- [3] "An Account of the New Alkali lately discovered in Sweden", *The Quarterly Journal of Science and the Arts* **5**, 337 (1818).
- [4] J. Fraunhofer, "Bestimmung des Brechungs- und Farbenzerstreuungs-Vermögens verschiedener Glasarten", *Denkschriften der kgl. Akademie der Wissenschaften zu München* **5**, 193 (1817).
- [5] G. Kirchhoff and R. Bunsen, "Chemische Analyse durch Spectralbeobachtungen", *Annalen der Physik und Chemie* **186**, 161 (1860).
- [6] G. Kirchhoff and R. Bunsen, "Chemische Analyse durch Spectralbeobachtungen – Zweite Abhandlung", *Annalen der Physik und Chemie* **189**, 337 (1861).
- [7] N. Bohr, "On the Constitution of Atoms and Molecules, Part I", *Phil. Mag.* **26**, 1 (1913).
- [8] N. Bohr, "On the Constitution of Atoms and Molecules, Part II – Systems containing only a Single Nucleus", *Phil. Mag.* **26**, 476 (1913).
- [9] L. Dunoyer, "Sur la réalisation d'un rayonnement matériel d'origine purement thermique. Cinétique expérimentale", *Le Radium* **8**, 142 (1911).
- [10] W. Gerlach and O. Stern, "Der experimentelle Nachweis des magnetischen Moments des Silberatoms", *Z. Physik* **8**, 110 (1922).
- [11] W. Gerlach and O. Stern, "Der experimentelle Nachweis der Richtungsquantelung im Magnetfeld", *Z. Physik* **9**, 349 (1922).
- [12] W. Gerlach and O. Stern, "Das magnetische Moment des Silberatoms", *Z. Physik* **9**, 353 (1922).
- [13] W. Gerlach and O. Stern, "Über die Richtungsquantelung im Magnetfeld", *Ann. Phys.* **379**, 673 (1924).
- [14] W. Gerlach, "Über die Richtungsquantelung im Magnetfeld II. Experimentelle Untersuchungen über das Verhalten normaler Atome unter magnetischer Kraftwirkung", *Ann. Phys.* **381**, 163 (1925).
- [15] R. Frisch, "Experimenteller Nachweis des Einsteinschen Strahlungsrückstoßes.", *Z. Phys.* **86**, 42 (1933).
- [16] P. Lebedev, "Untersuchungen über die Druckkräfte des Lichtes", *Ann. Phys.* **311**, 433 (1901).
- [17] E. F. Nichols and G. F. Hull, "A Preliminary Communication on the Pressure of Heat and Light Radiation", *Phys. Rev.* **13**, 307 (1901).
- [18] E. F. Nichols and G. F. Hull, "The Pressure Due to Radiation (Second Paper)", *Phys. Rev.* **17**, 26 (1903).
- [19] I. I. Rabi, J. R. Zacharias, S. Millman, , and P. Kusch, "A New Method of Measuring Nuclear Magnetic Moment", *Phys. Rev.* **53**, 318 (1938).
- [20] I. I. Rabi, S. Millman, , P. Kusch, and J. R. Zacharias, "The Molecular Beam Resonance Method for Measuring Nuclear Magnetic Moments. The Magnetic Moments of ${}^3\text{Li}^6$, ${}^3\text{Li}^7$ and ${}^9\text{F}^{19}$ ", *Phys. Rev.* **55**, 526 (1939).
- [21] P. Kusch, S. Millman, and I. I. Rabi, "The Radiofrequency Spectra of Atoms. Hyperfine Structure and Zeeman Effect in the Ground State of Li^6 , Li^7 , K^{39} and K^{41} ", *Phys. Rev.* **57**, 765 (1940).
- [22] S. Millman and P. Kusch, "On the Radiofrequency Spectra of Sodium, Rubidium and Caesium", *Phys. Rev.* **58**, 438 (1940).
- [23] F. Bloch, "Nuclear Induction", *Phys. Rev.* **70**, 460 (1946).
- [24] N. F. Ramsey, "History of Atomic Clocks", *J. Res. NBS* **88**, 301 (1983).
- [25] N. F. Ramsey, "A New Molecular Beam Resonance Method", *Phys. Rev.* **76**, 996 (1949).

- [26] N. F. Ramsey, "A Molecular Beam Resonance Method with Separated Oscillating Fields", *Phys. Rev.* **78**, 695 (1950).
- [27] L. Essen and J. V. L. Parry, "An Atomic Standard of Frequency and Time Interval: A Caesium Resonator", *Nature* **176**, 280 (1955).
- [28] A. Kastler, "Quelques suggestions concernant la production optique et la détection optique d'une inégalité de population des niveaux de quantification spatiale des atomes. Application à l'expérience de Stern et Gerlach et à la résonance magnétique", *J. Phys. Radium* **11**, 255 (1950).
- [29] J. Brossel, A. Kastler, and J. Winter, "Création optique d'une inégalité de population entre les sous-niveaux Zeeman de l'état fondamental des atomes", *J. Phys. Radium* **13**, 668 (1952).
- [30] W. B. Hawkins and R. H. Dicke, "The Polarization of Sodium Atoms", *Phys. Rev.* **91**, 1008 (1953).
- [31] W. Happer, "Optical Pumping", *Rev. Mod. Phys.* **44**, 169 (1972).
- [32] J. Vanier and C. Audoin, *The Quantum Physics of Atomic Frequency Standards* (Adam Hilger, Bristol, 1989).
- [33] A. L. Schawlow and C. H. Townes, "Infrared and Optical Masers", *Phys. Rev.* **112**, 1940 (1958).
- [34] T. H. Maiman, "Stimulated Optical Radiation in Ruby", *Nature* **187**, 493 (1960).
- [35] G. Alzetta, A. Gozzini, L. Moi, and G. Orriols, "An Experimental Method for the Observation of R.F. Transitions and Laser Beat Resonances in Oriented Na Vapour", *Nuovo Cimento* **36 B**, 5 (1976).
- [36] T. W. Hänsch and A. L. Schawlow, "Cooling of gases by laser radiation", *Opt. Commun.* **13**, 68 (1975).
- [37] D. J. Wineland and H. Dehmelt, "Proposed $10^{14} \Delta\nu < \nu$ Laser Fluorescence Spectroscopy on Ti^+ Mono-Ion Oscillator III", *Bull. Am. Phys. Soc.* **20**, 637 (1975).
- [38] W. D. Phillips and H. Metcalf, "Laser Deceleration of an Atomic Beam", *Phys. Rev. Lett.* **48**, 596 (1982).
- [39] S. Chu, L. Hollberg, J. E. Bjorkholm, A. Cable, and A. Ashkin, "Three-Dimensional Viscous Confinement and Cooling of Atoms by Resonance Radiation Pressure", *Phys. Rev. Lett.* **55**, 48 (1985).
- [40] E. L. Raab, M. Prentiss, A. Cable, S. Chu, and D. E. Pritchard, "Trapping of Neutral Sodium Atoms with Radiation Pressure", *Phys. Rev. Lett.* **59**, 2631 (1987).
- [41] M. H. Anderson, J. R. Ensher, M. R. Matthews, C. E. Wieman, and E. A. Cornell, "Observation of Bose-Einstein Condensation in a Dilute Atomic Vapor", *Science* **269**, 198 (1995).
- [42] U. Fano, "Description of States in Quantum Mechanics by Density Matrix and Operator Techniques", *Rev. Mod. Phys.* **29**, 74 (1957).
- [43] K. Blum, *Density Matrix Theory and Applications*, 2nd ed. (Plenum Press, New York, 1996).
- [44] S. Stenholm, *Foundations of Laser Spectroscopy* (Wiley, New York, 1984).
- [45] L. E. Ballentine, *Quantum Mechanics: A Modern Development* (World Scientific, Singapore, 1998).
- [46] P. Meystre and M. Sargent III, *Elements of Quantum Optics*, 3rd ed. (Springer, Berlin, 1999).
- [47] H. J. Metcalf and P. van der Straten, *Laser Cooling and Trapping* (Springer, New York, 1999).
- [48] A. R. Edmonds, *Drehimpulse in der Quantenmechanik* (Bibliographisches Institut, Mannheim, 1964).
- [49] D. R. Lide, editor, *CRC Handbook of Chemistry and Physics*, 89th ed. (CRC Press, Boca Raton, 2008).
- [50] E. Arimondo, M. Inguscio, and P. Violino, "Experimental determinations of the hyperfine structure in the alkali atoms", *Rev. Mod. Phys.* **49**, 31 (1977).
- [51] N. A. Nesmeyanov, *Vapor Pressure of the Chemical Elements* (Elsevier, New York, 1963).
- [52] A. V. Nowak and B. J. Krohn, "Spectral Characterization of a Tunable Alexandrite Laser by Rubidium Absorption at 780 nm", *IEEE J. Quantum Electron.* **QE-21**, 1607 (1985).
- [53] C. B. Alcock, V. P. Itkin, and M. K. Horrigan, "Vapour pressure equations for the metallic elements: 298–2500 K", *Canadian Metallurgical Quarterly* **23**, 309 (1984).
- [54] J. M. Luque, M. D. Calzada, and M. Saez, "A new procedure for Obtaining the Voigt function

- dependent upon the complex error function", *J. Quant. Spectrosc. Radiat. Transfer* **94**, 151 (2005).
- [55] M. L. Harris, C. S. Adams, S. L. Cornish, I. C. McLeod, E. Tarleton, and I. G. Hughes, "Polarization spectroscopy in rubidium and cesium", *Phys. Rev. A* **73**, 062509 (2006).
 - [56] S. R. Shin and H.-R. Noh, "Calculation and Measurement of Absolute Transmission in Rubidium", *J. Phys. Soc. Jpn.* **78**, 084302 (2009).
 - [57] S. R. Shin, H.-R. Noh, and H.-S. Noh, "Calculation of the Absorption Coefficient for a Doppler-Broadened Multilevel Atom", *J. Korean Phys. Soc.* **56**, 195 (2010).
 - [58] L. P. Maguire, R. M. W. van Bijnen, E. Mese, and R. E. Scholten, "Theoretical calculation of saturated absorption spectra for multi-level atoms", *J. Phys. B: At. Mol. Opt. Phys.* **39**, 2709 (2006).
 - [59] P. Siddons, C. S. Adams, C. Ge, and I. G. Hughes, "Absolute absorption on rubidium D lines: comparison between theory and experiment", *J. Phys. B: At. Mol. Opt. Phys.* **41**, 155004 (2008).
 - [60] J. Vanier, "Atomic clocks based on coherent population trapping: a review", *Appl. Phys. B* **81**, 421 (2005).
 - [61] E. Arimondo and G. Orriols, "Nonabsorbing Atomic Coherences by Coherent Two-Photon Transitions in a Three-Level Optical Pumping", *Lett. Nuovo Cimento* **17**, 333 (1976).
 - [62] H. R. Gray, R. M. Whitley, and C. R. Stroud, Jr., "Coherent trapping of atomic populations", *Optics Lett.* **3**, 218 (1978).
 - [63] G. Orriols, "Nonabsorption Resonances by Nonlinear Coherent Effects in a Three-Level System", *Nuovo Cimento* **53 B**, 1 (1979).
 - [64] E. Arimondo, "Coherent Population Trapping in Laser Spectroscopy", *Prog. Opt.* **35**, 257 (1996).
 - [65] A. Aspect, E. Arimondo, R. Kaiser, N. Vansteenkiste, and C. Cohen-Tannoudji, "Laser Cooling below the One-Photon Recoil Energy by Velocity-Selective Coherent Population Trapping", *Phys. Rev. Lett.* **61**, 826 (1988).
 - [66] S. E. Harris, "Lasers without Inversion: Interference of Lifetime-Broadened Resonances", *Phys. Rev. Lett.* **62**, 1033 (1989).
 - [67] E. S. Fry, X. Li, D. Nikonov, G. G. Padmabandu, M. O. Scully, A. V. Smith, F. K. Tittel, C. Wang, S. R. Wilkinson, and S.-Y. Zhu, "Atomic Coherence Effects within the Sodium D_1 Line: Lasing without Inversion via Population Trapping", *Phys. Rev. Lett.* **70**, 3235 (1993).
 - [68] K.-J. Boller, A. Imamoglu, and S. E. Harris, "Observation of Electromagnetically Induced Transparency", *Phys. Rev. Lett.* **66**, 2593 (1991).
 - [69] A. B. Matsko, O. Kocharovskaya, Y. Rostovtsev, G. R. Welch, A. S. Zibrov, and M. O. Scully, "Slow, ultraslow, stored, and frozen light", *Adv. At. Mol. Opt. Phys.* **46**, 191 (2001).
 - [70] M. O. Scully and M. Fleischhauer, "High-Sensitivity Magnetometer Based on Index-Enhanced Media", *Phys. Rev. Lett.* **69**, 1360 (1992).
 - [71] P. D. D. Schwindt, S. Knappe, V. Shah, L. Hollberg, J. Kitching, L.-A. Liew, and J. Moreland, "Chip-scale atomic magnetometer", *Appl. Phys. Lett.* **85**, 6409 (2004).
 - [72] V. Shah, S. Knappe, P. D. D. Schwindt, and J. Kitching, "Subpicotesla atomic magnetometry with a microfabricated vapour cell", *Nature Photonics* **1**, 649 (2007).
 - [73] R. Wynands and A. Nagel, "Precision spectroscopy with coherent dark states", *Appl. Phys. B* **68**, 1 (1999).
 - [74] R. Wynands and A. Nagel, "Erratum: Precision spectroscopy with coherent dark states", *Appl. Phys. B* **70**, 315 (2000).
 - [75] J. E. Thomas, P. R. Hemmer, S. Ezekiel, C. C. Leiby, Jr., R. H. Picard, and C. R. Willis, "Observation of Ramsey Fringes Using a Stimulated, Resonance Raman Transition in a Sodium Atomic Beam", *Phys. Rev. Lett.* **48**, 867 (1982).
 - [76] N. Cyr, M. Têtu, and M. Breton, "All-Optical Microwave Frequency Standard: A Proposal", *IEEE Trans. Instrum. Meas.* **42**, 640 (1993).
 - [77] J. Vanier, A. Godone, and F. Levi, "Coherent population trapping in cesium: Dark lines and coherent microwave emission", *Phys. Rev. A* **58**, 2345 (1998).
 - [78] S. Brandt, A. Nagel, R. Wynands, and D. Meschede, "Buffer-gas-induced linewidth reduc-

- tion of coherent dark resonances to below 50 Hz", *Phys. Rev. A* **56**, R1063 (1997).
- [79] R. Wynands, A. Nagel, S. Brandt, D. Meschede, and A. Weis, "Selection rules and line strengths of Zeeman-split dark resonances", *Phys. Rev. A* **58**, 196 (1998).
 - [80] C. Affolderbach, A. Nagel, S. Knappe, C. Jung, D. Wiedenmann, and R. Wynands, "Non-linear spectroscopy with a vertical-cavity surface-emitting laser (VCSEL)", *Appl. Phys. B* **70**, 407 (2000).
 - [81] A. Godone, F. Levi, and J. Vanier, "Coherent Microwave Emission Without Population Inversion: A New Atomic Frequency Standard", *IEEE Trans. Instrum. Meas.* **48**, 504 (1999).
 - [82] J. Vanier, M. W. Levine, D. Janssen, and M. J. Delaney, "The Coherent Population Trapping Passive Frequency Standard", *IEEE Trans. Instrum. Meas.* **52**, 258 (2003).
 - [83] J. Vanier, M. W. Levine, S. Kendig, D. Janssen, C. Everson, and M. J. Delaney, "Practical Realization of a Passive Coherent Population Trapping Frequency Standard", *IEEE Trans. Instrum. Meas.* **54**, 2531 (2005).
 - [84] Kernco Inc. <http://www.kernco.com>, October 2010.
 - [85] J. Kitching, S. Knappe, N. Vukićević, L. Hollberg, R. Wynands, and W. Weidmann, "A Microwave Frequency Reference Based on VCSEL-Driven Dark Line Resonances in Cs Vapor", *IEEE Trans. Instrum. Meas.* **49**, 1313 (2000).
 - [86] S. Knappe, R. Wynands, J. Kitching, H. G. Robinson, and L. Hollberg, "Characterization of coherent population-trapping resonances as atomic frequency standards", *J. Opt. Soc. Am. B* **18**, 1545 (2001).
 - [87] S. Knappe, V. Shah, P. D. D. Schwindt, L. Hollberg, J. Kitching, L.-A. Liew, and J. Moreland, "A microfabricated atomic clock", *Appl. Phys. Lett.* **85**, 1460 (2004).
 - [88] S. Knappe, P. D. D. Schwindt, V. Shah, L. Hollberg, J. Kitching, L. Liew, and J. Moreland, "A chip-scale atomic clock based on ^{87}Rb with improved frequency stability", *Opt. Express* **13**, 1249 (2005).
 - [89] V. Gerginov, S. Knappe, V. Shah, P. D. D. Schwindt, L. Hollberg, and J. Kitching, "Long-term frequency instability of atomic frequency references based on coherent population trapping and microfabricated vapor cells", *J. Opt. Soc. Am. B* **23**, 593 (2006).
 - [90] S. Knappe. "MEMS Atomic Clocks". In Y. Gianchandani, O. Tabata, and H. Zappe, editors, *Comprehensive Microsystems*, pp. 571–612. Elsevier, 2007.
 - [91] A. Godone, F. Levi, and S. Micalizio, *Coherent Population Trapping Maser* (C.L.U.T., Torino, 2002).
 - [92] R. H. Dicke, "The Effect of Collisions upon the Doppler Width of Spectral Lines", *Phys. Rev.* **89**, 472 (1953).
 - [93] W. Demtröder, *Laser Spectroscopy*, 2nd ed. (Springer, Berlin, 1996).
 - [94] M. Erhard, S. Nußmann, and H. Helm, "Power broadening and Doppler effects of coherent dark resonances in Rb", *Phys. Rev. A* **62**, 061802(R) (2000).
 - [95] WebElements: the periodic table on the web. <http://www.webelements.com>, October 2010.
 - [96] S. Micalizio, A. Godone, F. Levi, and J. Vanier, "Spin-exchange frequency shift in alkali-metal-vapor cell frequency standards", *Phys. Rev. A* **73**, 033414 (2006).
 - [97] C. Affolderbach, S. Knappe, R. Wynands, A. V. Taichenachev, and V. I. Yudin, "Electromagnetically induced transparency and absorption in a standing wave", *Phys. Rev. A* **65**, 043810 (2002).
 - [98] J. Kitching, H. G. Robinson, L. Hollberg, S. Knappe, and R. Wynands, "Optical-pumping noise in laser-pumped, all-optical microwave frequency references", *J. Opt. Soc. Am. B* **18**, 1676 (2001).
 - [99] H. Talvitie, M. Merimaa, and E. Ikonen, "Frequency stabilization of a diode laser to Doppler-free spectrum of molecular iodine at 633 nm", *Optics Comm.* **152**, 182 (1998).
 - [100] Ch. Ottinger, R. Scheps, G. W. York, and A. Gallagher, "Broadening of the Rb resonance lines by the noble gases", *Phys. Rev. A* **11**, 1815 (1975).
 - [101] P. L. Bender, E. C. Beaty, and A. R. Chi, "Optical Detection of Narrow Rb^{87} Hyperfine Absorption Lines", *Phys. Rev. Lett.* **1**, 311 (1958).
 - [102] J. Vanier, J.-F. Simard, and J.-S. Boulanger, "Relaxation and frequency shifts in the ground state of Rb^{85} ", *Phys. Rev. A* **9**, 1031 (1974).

- [103] D. B. Sullivan, J. C. Bergquist, J. J. Bollinger, R. E. Drullinger, W. M. Itano, S. R. Jefferts, W. D. Lee, D. Meekhof, T. E. Parker, F. L. Walls, and J. D. Wineland, "Primary Atomic Frequency Standards at NIST", *J. Res. Natl. Inst. Stand. Technol.* **106**, 47 (2001).
- [104] F. Levi, A. Godone, and J. Vanier, "The Light Shift Effect in the Coherent Population Trapping Cesium Maser", *IEEE Trans. Ultrason., Ferroelect., Freq. Contr.* **47**, 466 (2000).
- [105] C. Affolderbach, C. Andreeva, S. Cartaleva, T. Karaulanov, G. Mileti, and D. Slavov, "Light-shift suppression in laser optically pumped vapour-cell atomic frequency standards", *Appl. Phys. B* **80**, 841 (2005).
- [106] M. B. Bloch, J. C. Ho, C. S. Stone, A. Syed, and F. L. Walls. "Stability of high-quality quartz crystal oscillators: an update". In *Proceedings of the 43rd Annual Symposium on Frequency Control*, pp. 80–84. Institute of Electrical and Electronics Engineers, 1989.
- [107] K. L. Corwin, Z.-T. Lu, C. F. Hand, R. J. Epstein, and C. E. Wieman, "Frequency-stabilized diode laser with the Zeeman shift in an atomic vapor", *Appl. Opt.* **37**, 3295 (1998).
- [108] P. Ehrenfest, "Bemerkung über die angenäherte Gültigkeit der klassischen Mechanik innerhalb der Quantenmechanik", *Z. Physik* **45**, 455 (1927).
- [109] P. D. Lett, R. N. Watts, C. I. Westbrook, W. D. Phillips, P. L. Gould, and H. J. Metcalf, "Observation of Atoms Laser Cooled below the Doppler Limit", *Phys. Rev. Lett.* **61**, 169 (1988).
- [110] J. Dalibard and C. Cohen-Tannoudji, "Laser cooling below the Doppler limit by polarization gradients: simple theoretical models", *J. Opt. Soc. Am. B* **6**, 2023 (1989).
- [111] S. Du, M. B. Squires, Y. Imai, L. Czaia, R. A. Saravanan, V. Bright, J. Reichel, T. W. Hänsch, and D. Z. Anderson, "Atom-chip Bose-Einstein condensation in a portable vacuum cell", *Phys. Rev. A* **70**, 053606 (2004).
- [112] C. Monroe, W. Swann, H. Robinson, and C. Wieman, "Very Cold Trapped Atoms in a Vapor Cell", *Phys. Rev. Lett.* **65**, 1571 (1990).
- [113] C. Wieman, G. Flowers, and S. Gilbert, "Inexpensive laser cooling and trapping experiment for undergraduate laboratories", *Am. J. Phys.* **63**, 317 (1995).
- [114] J. Fortagh, A. Grossmann, T. W. Hänsch, and C. Zimmermann, "Fast loading of a magneto-optical trap from a pulsed thermal source", *J. Appl. Phys.* **84**, 6499 (1998).
- [115] J. Fortagh, H. Ott, A. Grossmann, and C. Zimmermann, "Miniaturized magnetic guide for neutral atoms", *Appl. Phys. B* **70**, 701 (2000).
- [116] H. Ott, J. Fortagh, G. Schlotterbeck, A. Grossmann, and C. Zimmermann, "Bose-Einstein Condensation in a Surface Microtrap", *Phys. Rev. Lett.* **87**, 230401 (2001).
- [117] S. Wildermuth, P. Krüger, C. Becker, M. Brajdic, S. Haupt, A. Kasper, R. Folman, and J. Schmiedmayer, "Optimized magneto-optical trap for experiments with ultracold atoms near surfaces", *Phys. Rev. A* **69**, 030901(R) (2004).
- [118] B. P. Anderson and M. A. Kasevich, "Loading a vapor-cell magneto-optic trap using light-induced atom desorption", *Phys. Rev. A* **63**, 023404 (2001).
- [119] W. Hänsel, P. Hommelhoff, T. W. Hänsch, and J. Reichel, "Bose-Einstein condensation on a microelectronic chip", *Nature* **413**, 498 (2001).
- [120] S. N. Atutov, R. Calabrese, V. Guidi, B. Mai, A. G. Rudavets, E. Scansani, L. Tomassetti, V. Biancalana, A. Burchianti, C. Marinelli, E. Mariotti, L. Moi, and S. Veronesi, "Fast and efficient loading of a Rb magneto-optical trap using light-induced atomic desorption", *Phys. Rev. A* **67**, 053401 (2003).
- [121] W. H. Wing, "On Neutral Particle Trapping in Quasistatic Electromagnetic Fields", *Prog. Quant. Electr.* **8**, 181 (1984).
- [122] A. Jaakkola, A. Shevchenko, K. Lindfors, M. Hautakorpi, E. Il'yashenko, T. H. Johansen, and M. Kaivola, "Reconfigurable atom chip on a transparent ferrite-garnet film", *Eur. Phys. J. D* **35**, 81 (2005).
- [123] J. D. Weinstein and K. G. Libbrecht, "Microscopic magnetic traps for neutral atoms", *Phys. Rev. A* **52**, 4004 (1995).
- [124] J. Fortagh, A. Grossmann, C. Zimmermann, and T. W. Hänsch, "Miniaturized Wire Trap for Neutral Atoms", *Phys. Rev. Lett.* **81**, 5310 (1998).
- [125] J. Denschlag, D. Cassettari, and J. Schmiedmayer, "Guiding Neutral Atoms with a Wire", *Phys. Rev. Lett.* **82**, 2014 (1999).

- [126] J. Reichel, W. Hänsel, and T. W. Hänsch, “Atomic Micromanipulation with Magnetic Surface Traps”, *Phys. Rev. Lett.* **83**, 3398 (1999).
- [127] R. Folman, P. Krüger, D. Cassettari, B. Hessmo, T. Maier, and J. Schmiedmayer, “Controlling Cold Atoms using Nanofabricated Surfaces: Atom Chips”, *Phys. Rev. Lett.* **84**, 4749 (2000).
- [128] J. Fortágh, H. Ott, S. Kraft, A. Günther, and C. Zimmermann, “Surface effects in magnetic microtraps”, *Phys. Rev. A* **66**, 041604(R) (2002).
- [129] A. E. Leanhardt, Y. Shin, A. P. Chikkatur, D. Kielpinski, W. Ketterle, and D. E. Pritchard, “Bose-Einstein Condensates near a Microfabricated Surface”, *Phys. Rev. Lett.* **90**, 100404 (2003).
- [130] S. Kraft, A. Günther, H. Ott, D. Wharam, C. Zimmermann, and J. Fortágh, “Anomalous longitudinal magnetic field near the surface of copper conductors”, *J. Phys. B: At. Mol. Opt. Phys.* **35**, L469 (2002).
- [131] P. Krüger, L. M. Andersson, S. Wildermuth, S. Hofferberth, E. Haller, S. Aigner, S. Groth, I. Bar-Joseph, and J. Schmiedmayer, “Potential roughness near lithographically fabricated atom chips”, *Phys. Rev. A* **76**, 063621 (2007).
- [132] C. Henkel, S. Pötting, and M. Wilkens, “Loss and heating of particles in small and noisy traps”, *Appl. Phys. B* **69**, 379 (1999).
- [133] M. P. A. Jones, C. J. Vale, D. Sahagun, B. V. Hall, and E. A. Hinds, “Spin Coupling between Cold Atoms and the Thermal Fluctuations of a Metal Surface”, *Phys. Rev. Lett.* **91**, 080401 (2003).
- [134] D. M. Harber, J. M. McGuirk, J. M. Obrecht, and E. A. Cornell, “Thermally Induced Losses in Ultra-Cold Atoms Magnetically Trapped Near Room-Temperature Surfaces”, *J. Low Temp. Phys.* **133**, 229 (2003).
- [135] Y. Lin, I. Teper, C. Chin, and V. Vuletić, “Impact of the Casimir-Polder Potential and Johnson Noise on Bose-Einstein Condensate Stability Near Surfaces”, *Phys. Rev. Lett.* **92**, 050404 (2004).
- [136] I. G. Hughes, P. A. Barton, T. M. Roach, M. G. Boshier, and E. A. Hinds, “Atom optics with magnetic surfaces: I. Storage of cold atoms in a curved ‘floppy disk’”, *J. Phys. B: At. Mol. Opt. Phys.* **30**, 647 (1997).
- [137] I. G. Hughes, P. A. Barton, T. M. Roach, and E. A. Hinds, “Atom optics with magnetic surfaces: II. Microscopic analysis of the ‘floppy disk’ mirror”, *J. Phys. B: At. Mol. Opt. Phys.* **30**, 2119 (1997).
- [138] C. V. Saba, P. A. Barton, M. G. Boshier, I. G. Hughes, P. Rosenbusch, B. E. Sauer, and E. A. Hinds, “Reconstruction of a Cold Atom Cloud by Magnetic Focusing”, *Phys. Rev. Lett.* **82**, 468 (1999).
- [139] T. M. Roach, H. Abele, M. G. Boshier, H. L. Grossman, K. P. Zetie, and E. A. Hinds, “Realization of a Magnetic Mirror for Cold Atoms”, *Phys. Rev. Lett.* **75**, 629 (1995).
- [140] C. D. J. Sinclair, E. A. Curtis, I. Llorente Garcia, J. A. Retter, B. V. Hall, S. Eriksson, B. E. Sauer, and E. A. Hinds, “Bose-Einstein condensation on a permanent-magnet atom chip”, *Phys. Rev. A* **72**, 031603(R) (2005).
- [141] B. Lev, Y. Lassailly, C. Lee, A. Scherer, and H. Mabuchi, “Atom mirror etched from a hard drive”, *Appl. Phys. Lett.* **83**, 395 (2003).
- [142] M. Boyd, E. W. Streed, P. Medley, G. K. Campbell, J. Mun, W. Ketterle, and D. E. Pritchard, “Atom trapping with a thin magnetic film”, *Phys. Rev. A* **76**, 043624 (2007).
- [143] B. V. Hall, S. Whitlock, F. Scharnberg, P. Hannaford, and A. Sidorov, “A permanent magnetic film atom chip for Bose-Einstein condensation”, *J. Phys. B: At. Mol. Opt. Phys.* **39**, 27 (2006).
- [144] I. Barb, R. Gerritsma, Y. T. Xing, J. B. Goedkoop, and R. J. C. Spreeuw, “Creating Ioffe-Pritchard micro-traps from permanent magnetic film with in-plane magnetization”, *Eur. Phys. J. D* **35**, 75 (2005).
- [145] T. Fernholz, R. Gerritsma, S. Whitlock, I. Barb, and R. J. C. Spreeuw, “Fully permanent magnet atom chip for Bose-Einstein condensation”, *Phys. Rev. A* **77**, 033409 (2008).
- [146] D. C. Lau, R. J. McLean, A. I. Sidorov, D. S. Gough, J. Koperski, W. J. Rowlands, B. A. Sexton, G. I. Opat, and P. Hannaford, “Magnetic mirrors with micron-scale periodicities for slowly moving neutral atoms”, *J. Opt. B: Quantum Semiclass. Opt.* **1**, 371 (1999).

- [147] S. Eriksson, F. Ramirez-Martinez, E. A. Curtis, B. E. Sauer, P. W. Nutter, E. W. Hill, and E. A. Hinds, "Micron-sized atom traps made from magneto-optical thin films", *Appl. Phys. B* **79**, 811 (2004).
- [148] H. B. G. Casimir and D. Polder, "The Influence of Retardation on the London-van der Waals Forces", *Phys. Rev.* **73**, 360 (1948).
- [149] C. I. Sukenik, M. G. Boshier, D. Cho, V. Sandoghdar, and E. A. Hinds, "Measurement of the Casimir-Polder force", *Phys. Rev. Lett.* **70**, 560 (1993).
- [150] C. D. J. Sinclair, J. A. Retter, E. A. Curtis, B. V. Hall, I. Llorente Garcia, S. Eriksson, B. E. Sauer, and E. A. Hinds, "Cold atoms in videotape micro-traps", *Eur. Phys. J. D* **35**, 105 (2005).
- [151] S. Whitlock, B. V. Hall, T. Roach, R. Anderson, M. Volk, P. Hannaford, and A. I. Sidorov, "Effect of magnetization inhomogeneity on magnetic microtraps for atoms", *Phys. Rev. A* **75**, 043602 (2007).
- [152] A. Shevchenko, M. Korppi, K. Lindfors, M. Heiliö, M. Kaivola, E. Il'yashenko, and T. H. Johansen, "All-optical reversible switching of local magnetization", *Appl. Phys. Lett.* **91**, 041916 (2007).
- [153] M. Merimaa, H. Talvitie, P. Laakkonen, M. Kuittinen, I. Tittonen, and E. Ikonen, "Compact external-cavity diode laser with a novel transmission geometry", *Opt. Commun.* **174**, 175 (2000).

Abstracts of Publications I–V

- I Using a three-level model and semiclassical density matrix formalism, we show that optical pumping influences both line positions and amplitudes in Doppler-broadened alkali-atom D_1 and D_2 spectra for intensities much lower than the two-level atom saturation intensity. The influence on the D_2 spectrum is particularly interesting due to the presence of closed hyperfine transitions unaffected by optical pumping. This effect is of importance for example when lasers are frequency stabilized using linear absorption or when the alkali-atom vapour pressure is determined using absorption measurements.
- II We study the influence of optical pumping on Doppler-broadened alkali-metal-atom D line spectra by solving the time-dependent density matrix for an open two-level system. The time-dependent absorption is averaged over the distribution of interaction times obtained from the three-dimensional beam geometry and atomic velocity distribution and over the longitudinal velocity distribution. The optical pumping is significant at much lower intensities than saturation and depends strongly on the intensity, beam radius, vapor cell length, and spontaneous-decay branching ratio. The result is in agreement with our earlier steady-state solution for a wide range of parameters and predicts two interesting line-shape features.
- III An all-optical RF standard based on dark states of ^{85}Rb atoms has been developed. With this system we were able to measure ultra-narrow optically induced hyperfine dark resonances below 20 Hz (Q-value $> 1.5 \times 10^8$). The frequency of a signal generator was stabilized to the dark resonance giving a relative frequency stability (square root of Allan variance) of $3.5 \times 10^{-11} \tau^{-1/2}$ ($1 \text{ s} < t < 2000 \text{ s}$). The best stability reached at an integration time of $t = 2000 \text{ s}$ was 6.4×10^{-13} , which is sufficient for many high-precision applications. The frequency shifts caused by various experimental parameters were also studied.
- IV An all-optical microwave frequency standard based on coherent population trapping (CPT) in ^{85}Rb is developed. The CPT resonances are detected by an ordinary edge-emitting diode laser in a simple optical setup. A buffer-gas mixture is carefully optimized to yield a narrow linewidth and a reduced temperature dependence of the resonance frequency. With the developed system we are able to measure ultranarrow optically induced hyperfine CPT resonances at $< 20 \text{ Hz}$, which is in good agreement with the linewidth calculated from experimental parameters. The frequency of an RF-signal generator has been stabilized to the CPT resonance between the two $m_F = 0$ magnetic sublevels. The relative frequency stability (square root of Allan variance) follows a slope of $3.5 \times 10^{-11} \tau^{-1/2}$ ($1 \text{ s} < \tau < 2000 \text{ s}$). The best

stability of 6.4×10^{-13} is reached at an integration time of $\tau = 2000$ s. This stability is sufficient for many high-precision applications. Frequency-shift measurements were made to evaluate the frequency dependencies on the operation parameters.

- V We describe experiments on the trapping of atoms in microscopic magneto-optical traps on an optically transparent permanent-magnet atom chip. The chip is made of magnetically hard ferrite-garnet material deposited on a dielectric substrate. The confining magnetic fields are produced by miniature magnetized patterns recorded in the film by magneto-optical techniques. We trap Rb atoms on these structures by applying three crossed pairs of counterpropagating laser beams in the conventional magneto-optical trapping geometry. We demonstrate the flexibility of the concept in creation and *in situ* modification of the trapping geometries through several experiments.

Erratum

In Publication [II](#), the caption for Fig. 9 should read:

Rubidium D₂ spectra for π or σ^+ polarization obtained from Eq. (22) (black solid curves), from [16] (red dashed curves), and neglecting optical pumping, but including saturation (blue dotted curves). (a) $I/I_s = 0.1$, $R = 10$ mm, (b) $I/I_s = 0.1$, $R = 1$ mm, (c) $I/I_s = 0.01$, $R = 1$ mm. $L = 50$ mm, $T = 300$ K.



ISBN 978-952-60-3501-7
ISBN 978-952-60-3502-4 (PDF)
ISSN 1795-2239
ISSN 1795-4584 (PDF)